DISSERTATIONES
PHYSICAE
UNIVERSITATIS
TARTUENSIS
105

ANDRES TIKO

Measurement of single top quark properties with the CMS detector

DISSERTATIONES PHYSICAE UNIVERSITATIS TARTUENSIS
105

DISSERTATIONES PHYSICAE UNIVERSITATIS TARTUENSIS
105

ANDRES TIKO

Measurement of single top quark properties with the CMS detector

UNIVERSITY OF TARTU
Press

This study was carried out at the National Institute of Chemical Physics and Biophysics and at the University of Tartu.

The dissertation was admitted on 6th of September 2016 in partial fulfilment of the requirements for the degree of Doctor of Philosophy in physics, and was allowed for defence by the Council of the Institute of Physics, University of Tartu.

Supervisors: Prof. Andrea Giammanco
Centre for Cosmology,
Particle Physics and Phenomenology,
Université catholique de Louvain,
Louvain-la-Neuve, Belgium

Dr. Mario Kadastik,
National Institute of Chemical Physics and Biophysics,
Tallinn, Estonia

Prof. Martti Raidal
University of Tartu and
National Institute of Chemical Physics and Biophysics,
Estonia

Opponent: Dr. Oliver Maria Kind
Humboldt University
Berlin, Germany

The public defence will take place on 21st of October 2016 in the Institute of Physics, University of Tartu, W. Ostwaldi Str. 1.

This work has been partially supported by graduate school "Functional materials and technologies" receiving funding from the European Regional Development Fund under project in University of Tartu, Estonia

ISSN 1406-0647
ISBN 978-9949-77-230-8 (print)
ISBN 978-9949-77-231-5 (pdf)

Copyright: Andres Tiko, 2016

University of Tartu Press
www.tyk.ee

Contents

Introduction

The top quark is the heaviest known elementary particle. It was predicted by Kobayashi and Maskawa in 1973 along with the bottom quark [4] to explain the observed CP violations in kaon decay, and discovered at Tevatron in 1995 [5, 6].

Due to its properties, the top quark plays a special role in the standard model of particle physics (SM) and in many of its extensions, which makes it an especially interesting object of study. An accurate knowledge of the properties of the top quark can provide further knowledge about the SM and potential to observe the effects of previously undiscovered processes predicted by many theories.

Outline and Author's Contribution

All the analyses presented in this work are focused on single top quark t-channel production. Chapter 1 describes the top quark and its properties in the context of SM, and summarises its production properties in high-energy colliders. In section 1.3, the focus is on the production mode where top quarks are produced singly, and the advantages of measuring the properties of this production mode are highlighted. In section 1.4, a specific property of top quark, polarisation, is introduced.

All of the measurements under discussion here are performed with the Compact Muon Solenoid (CMS) detector at the Large Hadron Collider (LHC). Chapter 2 illustrates the experimental setup, detailing the process of accelerating and colliding particles at the LHC as well as the measurement and reconstruction of various particles at CMS.

Simulated collision events are beneficial in many aspects of the measurements and the simulation procedures are described in section 3.1. The top quark itself decays before it can be measured and section 3.2 explains how the top quark and its properties can be reconstructed from the particles measured with CMS. Multiple other physical processes produce similar

signatures in the detector as the top quark, these are specified in section 3.3. How we differentiate between single top quark and background events and what is done to obtain a relatively pure sample of top quark events is explained in section3.5.

One of the statistical methods used for the purpose of discriminating between signal and background events is Boosted Decision Trees (BDT), which is described in the chapter for statistical methods, chapter 4. In there, the procedure of unfolding is also discussed. Unfolding is used in the polarisation measurement to obtain a value directly comparable to theoretical predictions.

A number of systematic uncertainties have to be taken into account for the measurements included in this work. Their details are described in chapter 5.

Chapter 6 documents the measurements of single top quark cross section at at the centre-of-mass energies of 7 and 8 TeV. In both of these measurements I was involved with the estimation of the QCD multijet background. In the measurement at 7 TeV, I performed independent cross-checks of the procedure, which is documented in section 6.1.3. In the measurement at 8 TeV, I developed the estimation procedure further, including adding various new cross-checks to verify the stability of the procedure. The results are documented in section 6.2.3. The measurements of single top quark cross section at the centre-of-mass energies of 7 and 8 TeV, have been published in the papers [1] and [2], respectively.

Chapter 7 is dedicated to the measurement of single top quark polarisation, performed at the centre-of-mass energy of 8 TeV. I contributed to almost all aspects of the measurement. Notably, the following contributions can be highlighted:

- The multijet background estimation with a methodology further improved from the cross section measurements, documented in section 7.3, is my work. I developed and optimised a new BDT discriminator to distinguish multijet and signal events, performed a fit to estimate the multijet background contribution and made various check to confirm the validity of the results.
- I developed the BDT discriminator to improve the discrimination of signal from the $t\bar{t}$ and W+jets backgrounds, as documented in section 7.5, which, except for the subsection on working point selection, describes my work.

- I performed the fit to extract the signal and background yields, described in section 7.8. This includes the treatment of systematical uncertainties, each of which required a separate fit to be performed.
- I performed the processing of data measured by the CMS detector as well as simulated samples for the signal, background and various systematical uncertainty scenarios according to the descriptions in chapter 3.
- I performed the W+jets p_{T} reweighting, as described in section 7.4.1.

The work presented in this chapter has been published in [3], where I also contributed to the writing of the sections covering the contributions listed above.

In the interests of the completeness of the overview, some material from the aforementioned papers is reproduced in the thesis. In particular, figures 6.2 to 6.4 and table 6.1 replicate the ones in article [1]. Figures 6.9 to 6.18 and 8.1, and tables 6.3 to 6.6 originate in the article [2]. Figures 1.5, 7.10, 7.15, 7.16, 7.24, 7.26, 7.29, and tables 7.7 to 7.9 are reproduced from article [3]. Additionally, some passages of text are reproduced from each of these papers.

Claims of the Thesis

The primary result of this thesis is the first measurement of the top quark spin asymmetry in t-channel single top quark production, sensitive to the top quark polarisation, which was performed based on a sample of proton-proton collisions at a centre-of-mass energy of 8 TeV, corresponding to an integrated luminosity of 19.7 fb^{-1}. Polarisation is an important property of the single top quark and its value can be used to discriminate between SM and competing theories.

In addition, another important property of the single top quark is its production cross section. My goal was to contribute to its measurement at centre-of-mass energies of 7 and 8 TeV through the development of a technique for measuring from data an important background to single top production, the multijet background.

Measuring the single top quark cross section is an important check of the SM in its own right, but participating in the measurements was also very useful for me as a preparation for the more intricate polarisation measurement. Analogously, as I was not in a leading role in the

cross section measurements, the results of these are secondary results in terms of this thesis, while they also set the stage for the measurement of polarisation.

1 Theoretical Background

1.1 Standard Model of Particle Physics

The SM is the state-of-the-art theory of particle physics, describing all known elementary particles and the interactions between them. It is a quantum field theory with local gauge symmetries. SM describes three of the four known fundamental forces, the strong, electromagnetic, and weak interactions based on the gauge group $\mathrm{SU(3)_C} \times \mathrm{SU(2)_L} \times \mathrm{U(1)_Y}$, where $\mathrm{SU(3)_C}$ corresponds to the strong interaction and the group $\mathrm{SU(2)_L} \times \mathrm{U(1)_Y}$ to the electroweak (EW) interaction that unifies the weak interaction with electromagnetism.

The particles described by the SM can be divided into fermions and bosons. Fermions are the particles matter is composed of. They have spin 1/2 and they obey the Pauli exclusion principle. The fermions are the six quarks (up (u), down (d), charm (c), strange (s), top (t), bottom (b)) and the six leptons (electron (e), muon (μ) and tau (τ), and corresponding neutrinos (ν_e, ν_μ, ν_τ)). All fermions interact weakly, while all of them except neutrinos carry electrical charge and thus additionally interact electromagnetically. Both quarks and leptons are organised pairwise into three generations. The corresponding particles in the generations exhibit similar physical behaviour, but differ by mass. Regular matter is made of only first generation particles, as particles with higher masses decay quickly into ones with lower mass and can be observed only in high-energy environments. The quarks are the only fermions that carry colour charge (blue, red or green) and participate in the strong interaction. For each fermion, there is also an antiparticle with the opposite charges. It is not yet clear whether neutrinos are their own antiparticles.

Gauge bosons are the particles that mediate forces, and they all have spin 1. Consequently, they do not respect the Pauli exclusion principle like fermions do. The photon (γ) mediates the electromagnetic (EM) force, the Z_0, W^+ and W^- bosons mediate the weak force, and eight gluons (g)

mediate the strong force. As a contrast to other gauge bosons, gluons themselves carry a colour charge and thus take part in strong interaction. In addition, there is the Higgs boson with spin 0, which creates particle masses through the electroweak symmetry breaking (EWSB) mechanism. The SM particles are illustrated in figure 1.1 and the interactions between them are sketched in figure 1.2.

A thorough description of SM in available in [7], while in the following we will shortly discuss some aspects relevant to this work.

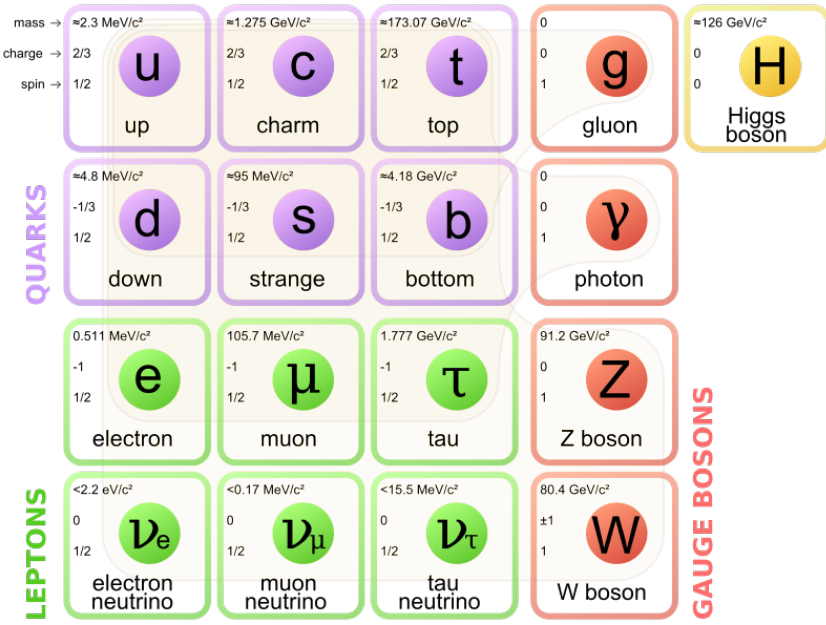

Figure 1.1: Standard model particles. Brown loops indicate which bosons (red) couple to which fermions (purple and green). Please note that the masses of some of the particles are not fully updated, see [7] for latest values. CC BY 3.0, author MissMJ, Wikimedia Commons

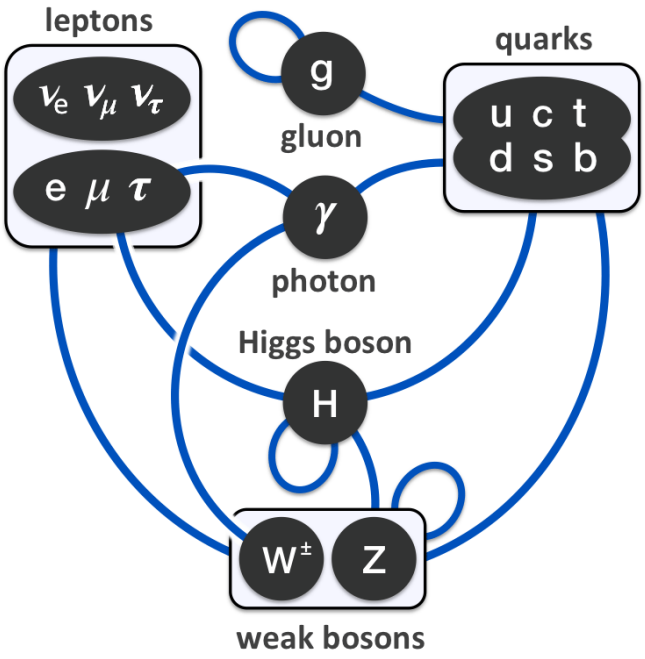

Figure 1.2: A diagram summarising interactions between elementary particles according to SM. Vertices (dark ovals) represent types of particles, and edges (blue arcs) represent interactions between them. Multiple generations of types of particle (leptons, quarks) share an oval. An arc that links to a box is equivalent to a set of arcs that link to every oval in the box. Author Eric Drexler, Wikimedia Commons

Quantum Chromodynamics

Quantum chromodynamics (QCD) is the theory of the strong interaction, a fundamental force, which acts between colour-charged particles – quarks and gluons. Through the interaction, the particles make up composite particles hadrons, e.g. protons, neutrons and pions. QCD is a non-Abelian gauge theory with the symmetry group SU(3).

The dynamics of quarks and gluons are described by the QCD Lagrangian, which can be written as:

$$\mathcal{L}_{\mathrm{QCD}} = \bar{\psi}_i \left(i(\gamma^\mu D_\mu)_{ij} - m\,\delta_{ij} \right) \psi_j - \frac{1}{4} G^a_{\mu\nu} G^{\mu\nu}_a , \tag{1.1}$$

where $G^a_{\mu\nu}$ represents the gauge invariant gluon field strength tensor,

$$G^a_{\mu\nu} = \partial_\mu \mathcal{A}^a_\nu - \partial_\nu \mathcal{A}^a_\mu + g f^{abc} \mathcal{A}^b_\mu \mathcal{A}^c_\nu , \tag{1.2}$$

$\psi_i(x)$ is the quark field and $\mathcal{A}^a_\mu(x)$ are the gluon fields, dynamical functions of spacetime in the fundamental and adjoint representation of SU(3), respectively. γ^μ are the Dirac matrices and the constants m and g determine the quark mass and coupling constants of the theory.

Colour is the conserved charge in QCD. Gluons are the force carrier of the strong interaction, similarly to photons in quantum electrodynamics (QED) for the EM force. However, the non-Abelian nature of QCD results in force mediators being colour-charged themselves.

This gives rise to confinement, which means that the force between quarks increases with distance and results in quarks being very strongly bound together to form composite particles (hadrons), which are colour-neutral. These are mainly particles containing either three quarks (baryons) or a quark and an antiquark (mesons). As a quark pair is separating from each other, the energy in the gluon field becomes enough to create another quark pair. The process repeats as long as there is enough energy left for creating new particles, resulting in showers of collimated particles in the general direction of the original quarks. The process is called hadronisation and the resulting showers of particles, called jets, are the measurable object in high-energy collisions.

An exception here is the top quark, which is the only quark that can be studied "naked". With a measured mass of $m_t = 173.34 \pm 0.76\,\mathrm{GeV}/c^2$ [8],

the top quark is by far the heaviest known fermion. Its production time $\approx 1/m_t$ is two orders of magnitude smaller than its lifetime $1/\Gamma_t, \Gamma_t \approx 2\,\text{GeV}$, which in turn is smaller than hadronisation time scale ($1/\Lambda_{QCD}$, $\Lambda_{QCD} \approx 0.2\,\text{GeV}$). This means that the top quark decays before forming hadrons and so can be studied using its decay products. Quark decay is not caused by the strong interaction, instead it takes place through the weak interaction.

Weak interaction

The electroweak interaction is based on the symmetry group $\mathrm{U}(1) \times \mathrm{SU}(2)_L$, with the subscript L indicating coupling only to left-handed fermions (and right-handed antifermions). To formulate the EW interaction as a gauge invariant theory, the covariant derivative is introduced as:

$$D_\mu := \partial_\mu - ig'\frac{1}{2}\,Y_W\,B_\mu - ig\frac{1}{2}\,\boldsymbol{\tau}\mathbf{W}_\mu \tag{1.3}$$

This makes the EW Lagrangian gauge invariant, but introduces four massless bosons, the $\mathrm{U}(1)$ gauge field B_μ and the three-component $\mathrm{SU}(2)$ gauge field W_μ. Y_W is the weak hypercharge, which generates of the $\mathrm{U}(1)$ group and $\boldsymbol{\tau}$ are the Pauli matrices (generators of the $\mathrm{SU}(2)$ group) whose eigenvalues give the weak isospin. The Lagrangian is given by:

$$\mathcal{L}_{\mathrm{EW}} = \sum_{\psi} i\bar{\psi}\gamma^\mu D_\mu \psi, \tag{1.4}$$

where ψ represents all the SM fermions. No mass terms can be added to the Lagrangian for neither fermions nor bosons, as this would break gauge symmetry. Still, experimentally the particles are not massless, and so another way of generating masses is needed.

Electroweak Symmetry Breaking

To solve this issue, the Higgs field is introduced as a complex scalar of the group $\mathrm{SU}(2)_L$:

$$\varphi = \frac{1}{\sqrt{2}}\begin{pmatrix} \varphi^+ \\ \varphi^0 \end{pmatrix}, \tag{1.5}$$

where indices + and 0 indicate the electric charge. Both components have weak isospin $Y_W = 1$.

The Higgs part of the Lagrangian is

$$\mathcal{L}_H = \left(D_\mu \phi\right)^\dagger \left(D_\mu \phi\right) - V(\phi), \tag{1.6}$$

where the Higgs potential is of the general form

$$V(\phi) = \mu^2 \phi^\dagger \phi + \lambda (\phi^\dagger \phi)^2 \tag{1.7}$$

In order to have a ground state, the potential should be bounded from below, i.e. $\lambda > 0$. If $\mu^2 \geq 0$, we end up with the minimum at $\phi = 0$. However, if $\mu^2 < 0$, the potential has an infinite set of degenerate states with a minimum energy of:

$$|\phi_0| = \sqrt{\frac{-\mu^2}{2\lambda}} \equiv \frac{v}{\sqrt{2}} \tag{1.8}$$

v is the vacuum expectation value of the Higgs field and is the only non-dimensionless parameter in the SM, with units of mass. In the unitarity gauge, ϕ^+ can be set to 0, so that ϕ^0 is real. This choice "spontaneously" breaks the symmetry of the Lagrangian and we end up with the potential

$$\varphi = \frac{1}{\sqrt{2}} \begin{pmatrix} 0 \\ v + h(x) \end{pmatrix}, \tag{1.9}$$

Substituting it into the Lagrangian, we are left with one massive scalar field $h(x)$, the Higgs field, while the three other components are "eaten up" by the gauge bosons, which obtain masses in the process, becoming the $W^\pm$ and Z bosons, while the photon remains massless, as the EM U(1) symmetry is not broken:

$$\begin{pmatrix} \gamma \\ Z^0 \end{pmatrix} = \begin{pmatrix} \cos\theta_W & \sin\theta_W \\ -\sin\theta_W & \cos\theta_W \end{pmatrix} \begin{pmatrix} B \\ W_3 \end{pmatrix} \tag{1.10}$$

and

$$W^\pm = \frac{1}{\sqrt{2}} (W_1 \mp i W_2) \tag{1.11}$$

θ_W is called the weak mixing angle, and it is a parameter of SM.

The masses of the gauge bosons are expressed as:

$$M_W = \frac{1}{2} v|g| \tag{1.12}$$

$$M_Z = \frac{1}{2} v\sqrt{g^2 + g'^2}, \tag{1.13}$$

or:

$$M_Z = \frac{M_W}{\cos\theta_W} \tag{1.14}$$

Interactions involving the $W^{\pm}$ act on only left-handed particles and right-handed antiparticles. The $W^{\pm}$ carry an electric charge and thus couple to the EM interaction, while the Z boson is electrically neutral, but interacts with both left- and right-handed particles and antiparticles.

For fermions, the mass terms can be introduced as Yukawa couplings between the fermion field ψ and the Higgs field ϕ, with unknown couplings G_ψ, which after symmetry breaking again gives rise to gauge-invariant mass terms, The Lagrange density for the Yukawa interaction of a fermion field ψ and the Higgs field ϕ is given by:

$$\mathcal{L}_{\text{Fermion}} = \overline{\psi}\gamma^\mu D_\mu \psi + G_\psi \overline{\psi}\phi\psi, \tag{1.15}$$

The Yukawa couplings are parameters of SM and in the framework of SM only derivable from measuring particle masses, which are proportional to the couplings:

$$M_\psi = G_\psi \frac{v}{\sqrt{2}} \tag{1.16}$$

Of particular interest here is again the top quark, which is the only known fermion with a mass at the EWSB scale v, indicating a Yukawa coupling to the Higgs boson of the order of unity [9].

The Higgs boson was discovered in 2012 [10, 11], completing the list of SM particles.

Quark mixing

Strong and electromagnetic interactions conserve quark flavour, which can only be transmuted by the weak interaction. That is, the conversion of a quark of one flavour (d, u, s, c, b, t) into a quark of another flavor

is allowed in SM only by the weak interaction. Also, it is observed that for quarks the mass eigenstates differ slightly from the weak interaction eigenstates. These flavour-changing weak interactions between quarks are described by the Cabibbo-Kobayashi-Maskawa (CKM) mixing matrix:

$$\begin{pmatrix} \mathrm{d}' \\ \mathrm{s}' \\ \mathrm{b}' \end{pmatrix} = \begin{pmatrix} V_{ud} & V_{us} & V_{ub} \\ V_{cd} & V_{cs} & V_{cb} \\ V_{td} & V_{ts} & V_{tb} \end{pmatrix} \cdot \begin{pmatrix} \mathrm{d} \\ \mathrm{s} \\ \mathrm{b} \end{pmatrix}, \tag{1.17}$$

where d′, c′ and b′ are the eigenstates of the weak interaction, while d, c and b are mass eigenstates.

The matrix can be parametrised in terms of three mixing angles and one complex phase, which violates CP-symmetry. The CKM matrix elements are fundamental parameters of the SM, so it is important to precisely determine their values, especially as many beyond the standard model (BSM) theories can modify the values of the parameters. The directly measured values of the CKM matrix elements are the following [7]:

$$\begin{pmatrix} |V_{ud}| & |V_{us}| & |V_{ub}| \\ |V_{cd}| & |V_{cs}| & |V_{cb}| \\ |V_{td}| & |V_{ts}| & |V_{tb}| \end{pmatrix} = \begin{pmatrix} 0.97425 \pm 0.00022 & 0.2253 \pm 0.0008 & (4.13 \pm 0.49) \cdot 10^{-3} \\ 0.225 \pm 0.008 & 0.986 \pm 0.016 & (41.1 \pm 1.3) \cdot 10^{-3} \\ (8.4 \pm 0.6) \cdot 10^{-3} & (40.0 \pm 2.7) \cdot 10^{-3} & 1.021 \pm 0.032 \end{pmatrix} \tag{1.18}$$

As can be seen from equation 1.18, the top quark couples almost exclusively to the bottom quark, decaying into the b quark and a W boson nearly 100% of the time. To date, the measurements are consistent with SM predictions, but more precision is required. It is possible to constrain the parameters further by a global fit taking into account model-dependent considerations, as described in [7], in particular, the requirement of unitarity for the matrix.

Open issues

The SM is a very successful theory, but at the same it has a number of important shortcomings. For example, SM only describes the composition

of ordinary matter, which makes up less than 5% of the universe. SM does not include a feasible dark matter candidate, and can not explain dark energy. SM also does not explain matter-antimatter asymmetry in the universe, as the CP-violation predicted from SM is too small for this.

Furthermore, it is believed that as electricity, magnetism and weak interaction have been unified, it should be possible to do so also for strong interaction and gravity, leading to a "theory of everything." Such a unification is not described by SM, but the described issues indicate that there must exist extensions of SM. Many such theories have been proposed, but so far there is no experimental evidence for any of them. Precise measurements of SM predictions are important in locating any discrepancies, which would provide hints of BSM physics.

1.2 Top Quark Measurement

Top quarks created in hadron collisions are produced dominantly in pairs through the processes $q\bar{q} \rightarrow t\bar{t}$ and $gg \rightarrow t\bar{t}$, at leading order in QCD [7]. The Feynman diagrams for these processes are shown in figure 1.3. At the Tevatron, which collided protons and antiprotons at 1.96 TeV, approximately 85% of the production cross section is from $q\bar{q}$ annihilation, with the rest from gluon-gluon fusion. In proton-proton collisions at the LHC, the situation is reversed, with $\approx 90\%$ of the production from gluon-gluon fusion at $\sqrt{s} = 14\,\text{TeV}$ ($\approx 80\%$ at 7 TeV) [7]. Top quarks can also be produced singly through electroweak (EW) production mechanisms. The production rates in single top production are smaller due to the weaker interaction, but still significant at high collision energies.

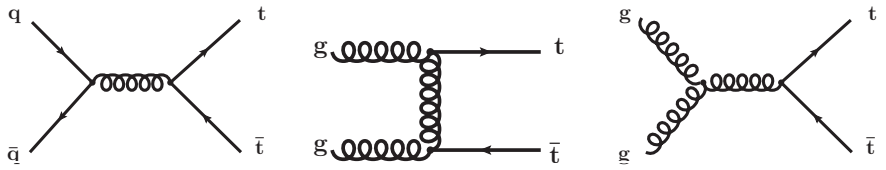

Figure 1.3: Leading order Feynman diagrams for $t\bar{t}$ production.

There are three main single top production modes, illustrated in figures 1.4 and 1.5, the *t*-channel, $qb \rightarrow q't$ mediated by a virtual *t*-channel

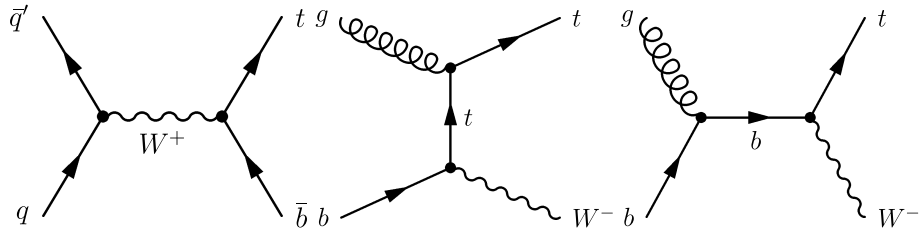

Figure 1.4: Leading order Feynman diagrams for single top quark production in the (left) *s*-channel and (centre and right) *t*W-associated processes. Similar diagrams are expected for top antiquark production.

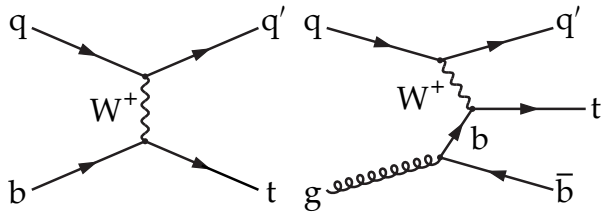

Figure 1.5: Feynman diagrams for single top quark production in the *t*-channel: (left) (2)→(2) and (right) (2)→(3) processes. Similar diagrams are expected for top antiquark production.

W-boson, the *s*-channel, $q\bar{q}' \rightarrow t\bar{b}$, mediated by a virtual *s*-channel W-boson, and the W-associated production (*t*W-channel) $qb \rightarrow W^-t$, as well as the respective processes for antiparticles.

Top quark was discovered in the pair production process at Tevatron in 1995 [5, 6], while single top production has only been first observed recently, in 2009 [12, 13]. Of the three single top channels, the *t*-channel is the most abundant at both Tevatron and LHC ($\approx$ 80% of the single top cross section at the LHC).

Due to the different colliding particles, the *t*- and *s*-channel cross sections are equal for top quarks and antiquarks at the Tevatron, but not at the LHC.

The W-associated production is negligible at the Tevatron, while the CMS and ATLAS (A Toroidal LHC Apparatus) experiments have mea-

sured it at the LHC [14, 15]. On the other hand, top quarks produced in the s-channel are relatively more copious at the Tevatron, which has made a measurement combining the data from their detectors [16]. At the LHC, the statistical significance is not enough to claim "re-discovery," but there is evidence of s-channel production at ATLAS [17].

1.3 Single Top Quark Properties

The study of the single top quark production provides a possibility to investigate the aspects of top quark physics related to the weak production mode, which cannot be studied in $t\bar{t}$ production, while various BSM physics models predict effects that show up in different single top production channels [18].

Precise measurements of the different single top production modes, such as differential cross sections in terms of different variables, charge asymmetry (difference in top quarks and antiquarks), and ratios of cross sections at different energies provide tests of SM predictions.

Additionally, the difference between production cross sections of single t and $\bar{t}$ results from a difference in parton distribution functions (PDF) of incident up and down quarks involved in the hard scattering, and can be probed by measuring the ratio of t and $\bar{t}$ production cross sections in the t-channel ($R_{t\text{-ch.}}$).

Another thing to look for are the so-called anomalous couplings of the top quark, which $R_{t\text{-ch.}}$ is also directly sensitive to [19]. Writing down the most general Lagrangian with up to dimension six operators for the Wtb coupling, we get [20]:

$$\mathcal{L}_{tWb}^{anom.} = -\frac{g}{\sqrt{2}}\bar{b}\gamma^{\mu}\left[(V_L P_L + V_R P_R) + \frac{i\sigma^{\mu\nu}q_{\nu}}{m_W}(g_L P_L + g_R P_R)\right] tW_{\mu}^{-} + h.c. \tag{1.19}$$

Here V_L (V_R) is left-handed (right-handed) vector coupling, and g_L (g_R) are tensor couplings. In SM $V_L = V_{tb} \approx 1$, while $V_R = g_L = g_R = 0$ at tree level, but possible deviations could be measured in single top processes.

Under the assumptions that $V_{tb} \gg V_{td}$, $V_{tb} \gg V_{ts}$ and that the Wtb coupling is purely left-handed, the cross sections of the single top processes are proportional to $|V_{tb}|^2$ [21]. The measurement of this value can be used to

test SM by detecting possible effects from additional quark-like particles coupling to the light quarks.

Assuming that $|V_{td}|$ and $|V_{ts}|$ are much smaller than $|V_{tb}|$, we can determine V_{tb} as:

$$|V_{tb}| = \sqrt{\sigma_{t\text{-ch.}}/\sigma_{t\text{-ch.}}^{\text{theo.}}}, \tag{1.20}$$

In the approximation $|V_{td}|, |V_{ts}| \ll |V_{tb}|$, we consider the top quark decay branching fraction into Wb, $\mathcal{B}$, to be almost equal to 1, thus obtaining [20, 22, 23]:

$$|V_L V_{tb}| = \sqrt{\sigma_{t\text{-ch.}}/\sigma_{t\text{-ch.}}^{\text{theo.}}}. \tag{1.21}$$

The choice of this approximation is motivated by the fact that several BSM scenarios predict a deviation of the measured value of V_L from 1, but only a mild modification of $\mathcal{B}$ [24]. This allows to interpret a possible deviation from SM single top quark production cross section in terms of new physics. In the SM case, $V_L = 1$, implying that the cross section measurement yields a direct constraint on $|V_{tb}|$.

Single top production also provides a way to look for flavour changing neutral current (FCNC) effects in the production and decay processes. In the SM, the neutral-current interactions do not change flavour, and while the limits for FCNC for lighter quarks are stringent, the constraints for FCNCs involving the top quark are less strongly constrained so far [7]. $R_{t\text{-ch.}}$ is also sensitive to FCNC contributions [25].

1.4 Single Top Quark Polarisation

One consequence of the large top quark mass is that the time scale for the top quark decay, $1/\Gamma_t$, set by its decay width $\Gamma_t \approx 2\,\text{GeV}$, is shorter than the hadronisation timescale $1/\Lambda_{QCD}$ and much shorter than the typical time m_t/Λ_{QCD}^2 required for QCD interactions to randomise its spin [26].

That is, a top quark decays with the same spin it is produced with. Furthermore, the EW V – A coupling at the Wtb vertex produces only left-handed top quarks in the SM. As the top quark decays before hadronising, the spin information is retained in its decay products. Although $\mathrm{t\bar{t}}$ production has a larger production cross section at the LHC, top quark pairs are dominantly not polarised, as they are produced primarily by the parity-conserving strong interaction through gluon-gluon fusion. [27]

To measure top quark polarisation, we can use the top quark spin asymmetry, defined as:

$$A_X \equiv \frac{1}{2} \cdot P_{\mathrm{t}}^{(\vec{s})} \cdot \alpha_X = \frac{N(\uparrow) - N(\downarrow)}{N(\uparrow) + N(\downarrow)} \tag{1.22}$$

$P_{\mathrm{t}}^{(\vec{s})}$ represents the top quark polarisation along an arbitrary polarisation axis $\vec{s}$ in production and the spin-analysing power α_X denotes the degree of the angular correlations of one of top quark's decay products, denoted X (W, ℓ, ν, or b), with the spin of the top quark. In the SM, α_X is exactly 1 for leptons at leading order (LO), but the value can be modified by anomalous top quark coupling models at the Wtb vertex in new physics theories [28, 20]. The variables $N(\uparrow)$ and $N(\downarrow)$ are defined for a top quark decay product X as the number of instances in which that X is aligned or anti-aligned, respectively, with the direction of $\vec{s}$ in the top quark rest frame.

The general form of the distribution of the angle θ_X^* between decay product X and the axis $\vec{s}$ in the top quark rest frame can be expressed as:

$$\frac{1}{\sigma}\frac{\mathrm{d}\sigma}{\mathrm{d}\cos\theta_X^*} = \frac{1}{2}(1 + P_{\mathrm{t}}^{(\vec{s})}\alpha_X \cos\theta_X^*) = \left(\frac{1}{2} + A_X \cos\theta_X^*\right). \tag{1.23}$$

It can be seen that at parton-level we expect a distribution with a slope which corresponds to the asymmetry.

The choice of basis for measuring polarisation basis has been studied in [9]. It turns out that the traditional helicity basis, the zero momentum frame, cannot be defined well enough to compute the top quark spin decomposition accurately. In addition, it has to be taken into account that the helicity of a massive particle is frame-dependent: in general, boosting to another frame will introduce a right-handed helicity component. Fortunately we can construct a spin basis in which well over 90% of the top quarks are produced in one of the two possible spin states: SM predicts that top quarks are strongly polarised along the direction of the momentum of the spectator quark (q′), which recoils against the top quark [9, 28] At the same time, new physics models can alter the coupling structure in a way leading to depolarisation in production [20, 29, 30]. Hence, a clear indication of an anomalous coupling structure would be

an excess of events where the q' momentum is anti-aligned with the top quark spin.

To take advantage of this fact, we study single top quark polarisation in the t-channel with polarisation axis defined as pointing along the direction of the untagged jet j' in the top quark rest frame, which is a good estimate of q' direction. This is called the "spectator basis".

Previously, the measurement of top quark polarisation in single top quark production has only been attempted by the CDF collaboration [31]. However, with only 3.2 fb^{-1} of $p\bar{p}$ collision data at a centre-of-mass energy of 1.96 TeV, the precision was not sufficient to exclude the hypothesis that single top quarks have the opposite polarisation to the one predicted by the SM, or are produced unpolarised.

2 LHC and the CMS Detector

2.1 Large Hadron Collider

The Large Hadron Collider (LHC) [32] is the world's largest and highest-energy particle accelerator. The LHC operates in a circular tunnel with a circumference of 27 km at CERN near Geneva, Switzerland.

LHC is a proton-proton collider with a maximum design energy of 14 TeV, also capable of colliding Pb ions. The analyses considered in this work are performed on data collected during the first run of LHC data taking at energies of 7 and 8 TeV.

The collider incorporates two parallel beam pipes, which contain beams that travel in opposite directions. The beams are directed to stay on a circular path by dipole magnets of 8.4 T with an operating temperature of 1.9 K. The dipole magnet cross-section can be seen on figure 2.1. Quadrupole magnets are used for focusing the beams for maximal chance of interaction in the four points where beams cross and collisions occur. The beams consist of up to 2808 bunches, with 10^{11} protons in each bunch, so that interactions between the two beams take place at 25 or 50 ns apart, depending on the setup of the collider.

The number of collisions N occurring per unit of time is given by:

$$\frac{dN}{dt} = \mathcal{L}\sigma, \tag{2.1}$$

where $\mathcal{L}$ is luminosity and σ is the interaction cross section.

A gaussian estimation of luminosity calculated using machine parameters is given as:

$$\mathcal{L} = \frac{{N_b}^2 n_b f_{rev} \gamma_{rev}}{4\pi\epsilon_n \beta^*} F, \tag{2.2}$$

where N_b is the number of particles per bunch, n_b the number of bunches per beam, f_{rev} the revolution frequency, γ_r the relativistic gamma fraction,

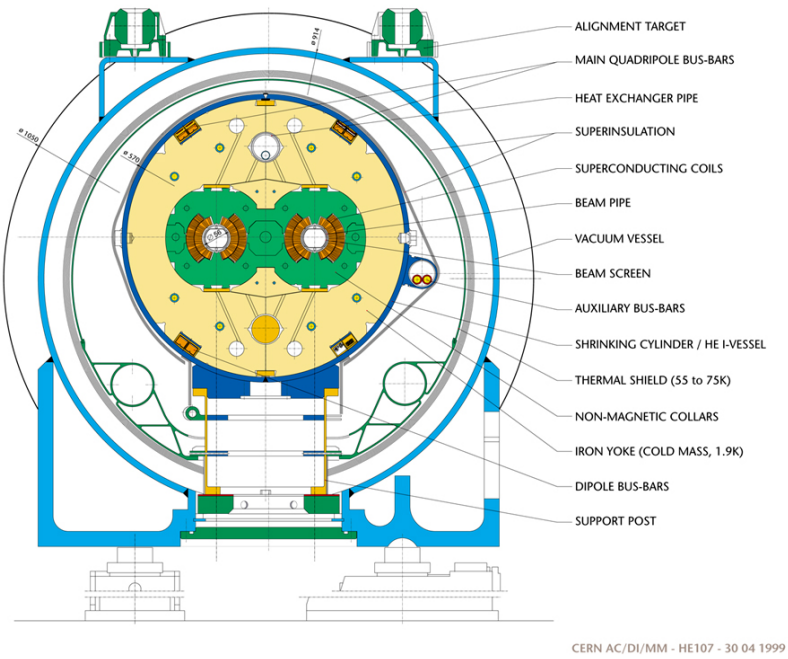

Figure 2.1: Cross-section of a LHC dipole magnet. © CERN

ϵ_n the normalised transverse beam emittance, β^* the amplitude function at the interaction point (IP) describing the cross-section of the beam and F the geometric luminosity reduction factor due to the crossing angle at the IP.

The peak design luminosity of the LHC is $\mathcal{L} = 10^{34}\,\mathrm{cm}^{-2}\,\mathrm{s}^{-1}$. The total number of collisions is obtained through integrated luminosity:

$$L = \int \mathcal{L} dt. \tag{2.3}$$

Before entering LHC, the particles pass through a series of smaller accelerators, each of which increase their energy further. The first is the linear particle accelerator LINAC 2, which generates 50 MeV protons. These are fed into the Proton Synchrotron Booster, where the protons are accelerated to an energy of 1.4 GeV. Then they are injected into the

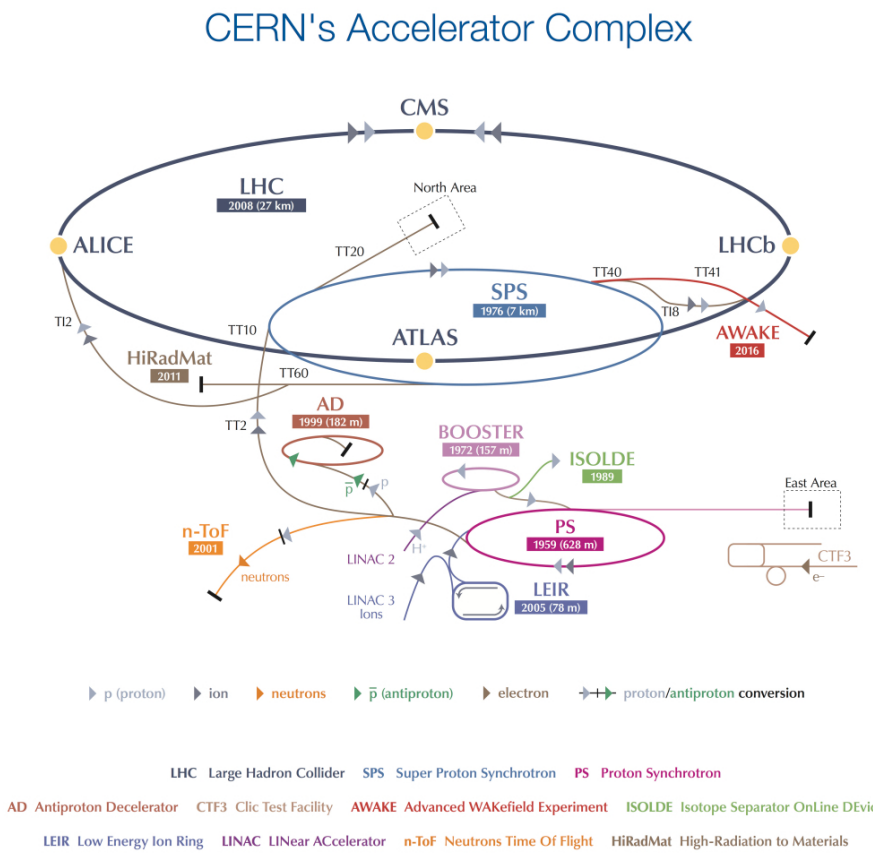

Figure 2.2: The LHC is the last ring (dark grey line) in a complex chain of particle accelerators. The smaller machines are used in a chain to help boost the particles to their final energies and provide beams to a whole set of smaller experiments, which also aim to uncover the mysteries of the Universe. © CERN

Proton Synchrotron (PS), where their energy is increased to 26 GeV, and after that into the Super Proton Synchrotron (SPS), where they achieve an energy of 450 GeV before being injected into LHC. In the LHC, the particles are accumulated to bunches, accelerated to their peak energy,

and then circulate the accelerator while producing collisions for several hours, until the luminosity drops considerably. The accelerators at CERN, including the LHC, are illustrated in figure 2.2.

Seven experiments are in operation at the LHC. The four main ones, each in one of the four beam crossing locations, are general purpose detectors ATLAS [33] and CMS [34], ALICE (A Large Ion Collider Experiment) [35] for studies of heavy ions, and LHCb (LHC-beauty) [36] for studying CP violation in the interactions of b-hadrons. There are also three smaller specialised experiments: TOTEM (Total Cross Section, Elastic Scattering and Diffraction Dissociation) [37], LHCf (LHC-forward) [38] and MoEDAL (Monopole and Exotics Detector At the LHC) [39].

2.2 Compact Muon Solenoid

The central feature of the CMS apparatus [34] is a superconducting solenoid of 6 m internal diameter. Within the superconducting solenoid volume are a silicon pixel and strip tracker, a lead tungstate crystal electromagnetic calorimeter (ECAL), and a brass and scintillator hadron calorimeter (HCAL), each composed of a barrel and two endcap sections. The CMS apparatus has an overall length of 22 m, a diameter of 15 m, and weighs 14 000 tonnes.

The coordinate system adopted by CMS has the origin centred at the nominal collision point inside the experiment, the y-axis pointing vertically upward, and the x-axis pointing radially inward toward the centre of the LHC. Thus, the z-axis points along the beam direction toward the Jura mountains from LHC Point 5. The azimuthal angle ϕ is measured from the x-axis in the x-y plane and the radial coordinate in this plane is denoted by r. The polar angle θ is measured from the z-axis. Pseudorapidity is defined as:

$$\eta = -\ln\tan(\theta/2). \tag{2.4}$$

The missing transverse momentum vector $\vec{p}_{\mathrm{T}}^{\,\mathrm{miss}}$ is defined as the projection of the negative vector sum of the momenta of all reconstructed particles in an event onto the plane perpendicular to the beams. Its magnitude is referred to as missing transverse energy, $\not{E}_{\mathrm{T}}$.

Forward calorimeters extend the pseudorapidity coverage provided by the barrel and endcap detectors. Muons are measured in gas-ionisation

detectors embedded in the steel flux-return yoke outside the solenoid. An illustration of the detector is shown on figure 2.3. The silicon tracker measures charged particles within the pseudorapidity range $|\eta| < 2.5$. It consists of 1440 silicon pixel and 15 148 silicon strip detector modules and is located in the 3.8 T field of the superconducting solenoid. For non-isolated particles of $1 < p_T < 10\,\text{GeV}/c$ and $|\eta| < 1.4$, the track resolutions are typically 1.5% in p_T and 25–90 (45–150) μm in the transverse (longitudinal) impact parameter [40]

The ECAL consists of 75 848 lead tungstate crystals which provide coverage in pseudorapidity $|\eta| < 1.479$ in a barrel region (EB) and $1.479 < |\eta| < 3.0$ in two endcap regions (EE). A preshower detector consisting of two planes of silicon sensors interleaved with a total of $3X_0$ of lead is located in front of the EE.

In the barrel section of the ECAL, an energy resolution of about 1% is achieved for unconverted or late-converting photons in the tens of GeV energy range. The remaining barrel photons have a resolution of about 1.3% up to a pseudorapidity of $|\eta| = 1$, rising to about 2.5% at $|\eta| = 1.4$. In the endcaps, the resolution of unconverted or late-converting photons is about 2.5%, while the remaining endcap photons have a resolution between 3 and 4% [41]. The HCAL, when combined with the ECAL, measures jets with a resolution $\Delta E/E \approx 100\%/\sqrt{E\,[\text{GeV}]} \oplus 5\%$.

In the region $|\eta| < 1.74$, the HCAL cells have widths of 0.087 in pseudorapidity and 0.087 in azimuth (ϕ). In the η-ϕ plane, and for $|\eta| < 1.48$, the HCAL cells map on to 5×5 ECAL crystals arrays to form calorimeter towers projecting radially outwards from close to the nominal interaction point. At larger values of $|\eta|$, the size of the towers increases and the matching ECAL arrays contain fewer crystals. Within each tower, the energy deposits in ECAL and HCAL cells are summed to define the calorimeter tower energies, subsequently used to provide the energies and directions of hadronic jets.

A more detailed description of the CMS detector can be found in [34].

2.2.1 Global Event Reconstruction

The global event reconstruction (also called particle-flow event reconstruction (PF) [42, 43]) consists in reconstructing and identifying each single particle with an optimised combination of all sub-detector information. In this process, the identification of the particle type (photon, electron, muon, charged hadron, neutral hadron) plays an important role in the determination of the particle direction and energy. An illustration of how CMS detects different kinds of particles is shown on figure 2.4.

2.2.2 Photons

Photons (e.g. coming from π^0 decays or from electron bremsstrahlung) are identified as ECAL energy clusters not linked to the extrapolation of any charged particle trajectory to the ECAL. The energy of photons is directly

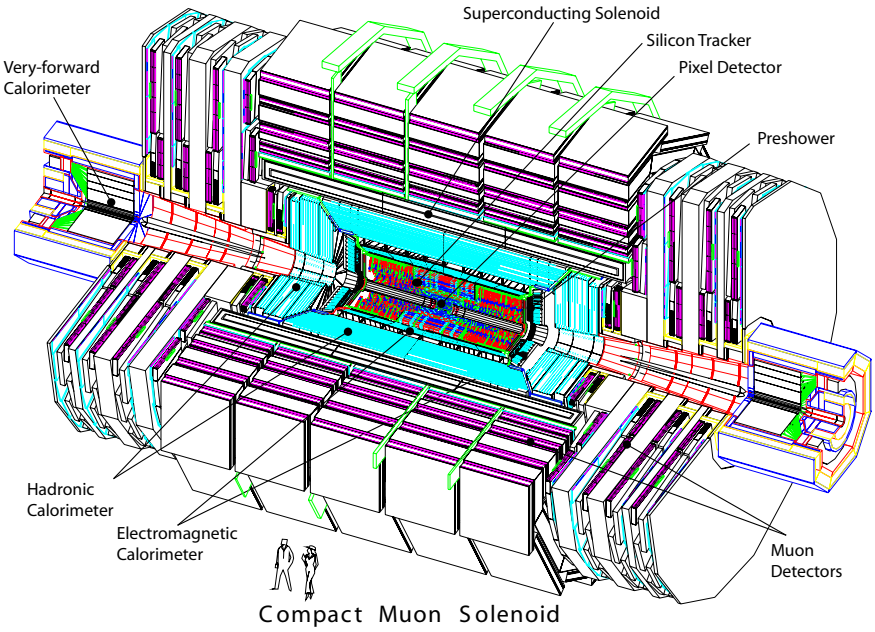

Figure 2.3: The CMS detector.

obtained from the ECAL measurement, corrected for zero-suppression effects.

2.2.3 Electrons

Electrons (e.g. coming from photon conversions in the tracker material or from b-hadron semileptonic decays) are identified as a primary charged particle track and potentially many ECAL energy clusters corresponding to this track extrapolation to the ECAL and to possible bremsstrahlung photons emitted along the way through the tracker material.

The electron momentum is estimated by combining the energy measurement in the ECAL with the momentum measurement in the tracker. The track fit is performed using a Gaussian Sum Filter (GSF), which allows the track to be reconstructed right out to the ECAL surface, despite kinks due to radiated bremsstrahlung. The momentum resolution for electrons with $p_T \approx 45\,\text{GeV}/c$ from $Z \to ee$ decays ranges from 1.7% for non-showering electrons in the barrel region to 4.5% for showering electrons in the endcaps [44].

2.2.4 Muons

Muons (e.g. from b-hadron semileptonic decays or from W boson decays) are identified as a track in the central tracker consistent with either a track or several hits in the muon system, associated with an energy deficit in the calorimeters. Muons are measured in the pseudorapidity range $|\eta| < 2.4$, with detection planes made using three technologies: drift tubes (DT), cathode strip chambers (CSC), and resistive plate chambers(RPC).

The muon reconstruction chain starts with the “local reconstruction”. First, hits in DTs, CSCs and RPCs are reconstructed from digitised electronic signals. Hits within each DT and CSC chamber are then matched to form “segments” (track stubs).

Stand-alone muons

In the offline reconstruction, the segments reconstructed in the muon chambers are used to generate "seeds" consisting of position and direction vectors and an estimate of the muon transverse momentum. These initial

estimates are used as seeds for the track fits in the muon system, which are performed using segments and hits from DTs, CSCs and RPCs and are based on the Kalman filter technique [45]. The result is a collection of reconstructed track objects reconstructed, which are referred to as “stand-alone muons”.

Global Muons

While each sub-detector is able to measure a part of a muon’s properties, the concept of a global muon is to combine information from multiple sub-detectors in order to obtain a more accurate description of the muon.

The muons’ track parameters are measured in two sub-detectors: the inner tracker, and the muon system. The momentum resolution of muon tracks up to $p_{\mathrm{T}} = 200\,\mathrm{GeV}/c$ reconstructed in the muon system alone is dominated by multiple scattering. At low momentum, the best momentum resolution for muons is obtained from the silicon tracker. However, at higher momentum, the characteristics of the muon system allow the improvement of the muon momentum resolution by combining the muon track from the silicon detector (tracker track), with the stand-alone muon into a global muon track.

For each "tracker track" - "standalone muon" pair, the track fit using all hits in both tracks is performed, again based on the Kalman filter technique, and the best-matching pair is selected. The resulting object is called a “global muon”.

Matching muons to tracks measured in the silicon tracker results in a relative transverse momentum resolution for muons with $20 < p_{\mathrm{T}} < 100\,\mathrm{GeV}/c$ of 1.3–2.0% in the barrel and better than 6% in the endcaps. The p_{T} resolution in the barrel is better than 10% for muons with p_{T} up to $1\,\mathrm{TeV}/c$ [46].

Tracker Muons

In some cases the hit and segment information in the muon system is minimal, and stand-alone muon reconstruction fails, for example for a large fraction of muons with p_{T} below 6-7 GeV/c. A complementary approach consists in considering all silicon tracker tracks and identifying them as muons by looking for compatible signatures in the calorimeters

and in the muon system. Muons identified with this method are called "Tracker Muons." However, while tracker muons are useful, are in general not used without further requirements because the association between muon chamber segments and tracker tracks is kept very loose by design.

2.2.5 Hadrons

Charged hadrons are identified as charged particle tracks identified neither as electrons nor as muons. The energy of charged hadrons is determined from a combination of the track momentum and the corresponding ECAL and HCAL energy, corrected for zero-suppression effects and for the response function of the calorimeters to hadronic showers. Neutral hadrons are identified as HCAL energy clusters not linked to any charged hadron trajectory, or as ECAL and HCAL energy excesses with respect to the expected charged hadron energy deposit, and their energy is obtained from the corresponding corrected ECAL and HCAL energy.

2.2.6 Jet Clustering

For each event, hadronic jets are clustered from the reconstructed particles with the infrared and collinear safe anti-k_{T} algorithm [47], operated with a size parameter $\Delta R = \sqrt{(\Delta\eta)^2 + (\Delta\phi)^2}$ of 0.5. The jet momentum is determined as the vectorial sum of all particle momenta in this jet, and is found in the simulation to be within 5% to 10% of the true momentum over the whole p_{T} spectrum and detector acceptance. Jet energy corrections are derived from the simulation, and are confirmed with in situ measurements with the energy balance of dijet and photon+jet events [48]. The jet energy resolution amounts typically to 15% at 10 GeV, 8% at 100 GeV, and 4% at 1 TeV, to be compared to about 40%, 12%, and 5% obtained when the calorimeters alone are used for jet clustering.

2.2.7 Triggering

In total, there are $\sim 10^8$ data channels checked in each bunch crossing. The first level (L1) of the CMS trigger system, composed of custom hardware processors, uses information from the calorimeters and muon detectors to select the most interesting events in a fixed time interval of less than 4 μs.

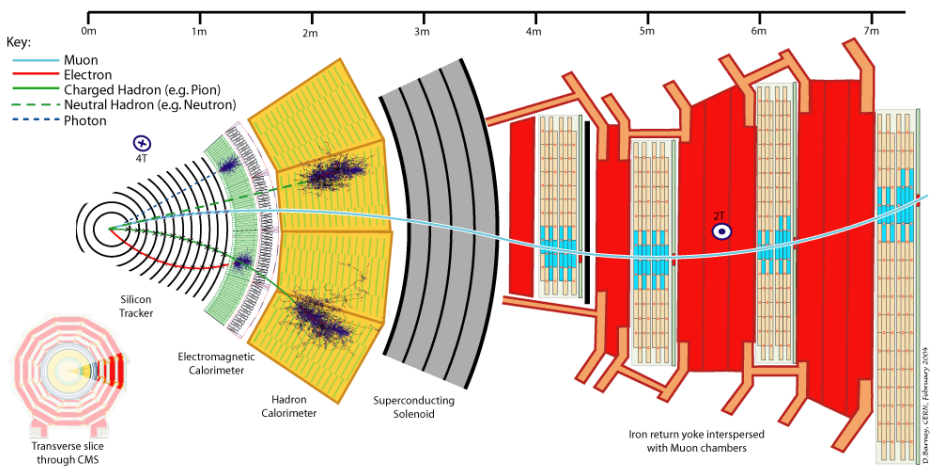

Figure 2.4: An illustration of how CMS detects different kinds of particles. The trajectory of an electron, shown with a red line, is measured with the tracker and its energy with the ECAL. A photon, shown with a blue dashed line, also has its energy measured with the ECAL, but it does not leave a track. A charged hadron, shown with a green line, registers in the tracker and its energy is measured with the HCAL. Neutral hadrons, shown with a dashed green line, are also measured with the HCAL while not leaving a track. Muons leave a track in the tracker, after which they pass outside the superconducting magnet and are measured in the muon chambers. Neutrinos pass through the detector undetected.

The high-level trigger (HLT) processor farm further decreases the event rate from around 100 kHz to less than 1 kHz, before data storage. This is referred to as the "online" selection, whereas further analysis based on the data saved in this way is called the "offline" selection.

3 Event Modelling and Reconstruction

3.1 Simulation and Detection of Events

3.1.1 Monte Carlo Event Simulation

Monte Carlo (MC) Event Generators are used to generate high-energy-physics (HEP) events, giving as output a set of randomly generated outgoing particles produced in the interactions between two incoming particles according to the probability of a given process. MC simulations play an essential role in modelling HEP processes, providing the opportunity to compare theoretical predictions to measurements. Simulations are invaluable also before any data is collected to study the feasibility of measurements, optimise event selection, calculate efficiencies etc.

A large number of event generators are in in use, including several general-purpose generators, such as PYTHIA [49, 50] and SHERPA [51, 52]. Such generators aim to compute the amplitudes of all the Feynman diagrams contributing to a given perturbative order in strong coupling constant α_S. Such (next-to)^k-leading-order (N^{k}LO) computations are technically challenging, and general solutions were until recently known only for the case of one extra order (NLO). General-purpose event generators aim to provide an accurate description of the whole collision process, including aspects like hard and soft interactions, parton distributions, initial and final state parton showers, multiple interactions, fragmentation and decay. Some generators are specific to some physical processes like TAUOLA [53] for tau decays.

Another class of MC generators are Matrix Element (ME) calculators, such as POWHEG [54], MADGRAPH [55], aMC@NLO [56], COMPHEP [57] etc. They produce events at the parton level, and other generators can be used to develop a fully hadronised event.

Single top quark production can be studied in the 5- or 4-flavour schemes [58]. In the 5-flavour scheme (5FS), the b quarks are considered as constituents of the proton. In the 4-flavour scheme (4FS), they are instead generated in the hard scattering from gluon splitting.

Vertex smearing is applied to the events after generation to model the physical spread of the collisions. An in-depth discussion of event generation, different generators and their properties can be found in [59].

3.1.2 Parton Distribution Functions

As explained in [59], the calculation of any production cross sections in hadron collisions depends on a knowledge of the distribution of the momentum fraction x of the quarks and gluons in the incoming hadrons. The parton distribution functions (PDFs) can not be perturbatively calculated, but are instead determined by global fits to data. These fits are performed by multiple groups, we use the ones provided in CT10 [60], MSTW [61] and NNPDF [62] PDF sets. We use the PDF sets in accordance with recommendations for LHC given in [63].

3.1.3 Detector Simulation

The MC event generators only output a set of particles after a collision, but the particles also interact with the detector. Thus, to be able to accurately compare simulated and measured events, we also need to simulate the detector itself.

Full-scale simulation of the CMS detector is based on the GEANT4 [64] toolkit. It relies on a fairly detailed description of the hierarchy of volumes and materials, and knowing which parts are "sensitive detector" (i.e., furnished with a readout) as opposed to "dead materials". Generated particles are taken as input, traced through the hierarchy of volumes and materials, and modelled in physics processes that accompany particle passage through matter. Results of particles' interactions with matter are recorded in the form of simulated hits, including also the interactions of secondary particles, which are created in interactions of primary particles with the detector.

In addition, "pileup" simulation deals with the effect of more that one interaction per beam crossing. This is due to high concentration of

particles in a bunch, causing more than one pair of protons to collide at a time, and/or the effect of the signal spill-over from the previous bunch crossing(s) into the current crossing (event), due to the fact that the time between collisions (bunch spacing) is often shorter than the duration of an electronic signal in some subdetectors. The effect of pileup interactions is evaluated by superimposing a sample of minimum-bias events (i.e. events mimicking a trigger selection as close to totally inclusive as possible, which registers all events with any activity in the detector) produced using PYTHIA 6 to the signal, with reweighting to reproduce the true pileup distribution measured from the data. The validation of the procedure is performed by comparing the number of observed primary vertices in data and to the number in simulation.

Finally, the response of the detector readout electronics is reproduced in accordance with the CMS detector structure, a process known as digitisation.

Since the simulation of an event with the full detector simulation is a time-consuming process, the Fast Simulation [65], which uses parametric approach to simulate and reconstruct events with the CMS detector, is in some cases used instead. This reduces the processing time overhead, while still achieving a comparably accurate simulation of the detector effects.

3.2 Top Quark Reconstruction

The t-channel signature is shown on figure 3.1. We are looking at leptonic decays of the W boson, which means we have one lepton in the final state along with considerable missing transverse energy from an energetic neutrino. There is a b-jet from the top decay and a light-flavour jet produced in the forward region. There is also a second b-jet which is usually outside our acceptance.

In the following, we discuss how the top quark and related objects needed for analyses are reconstructed, building upon the description of the detection principles in CMS as described in section 2.2. This section defines the basic analysis objects on which the event selection and the kinematic reconstruction are based. The reconstruction of all objects is done through the PF algorithm [42]. Due to the different conditions in the

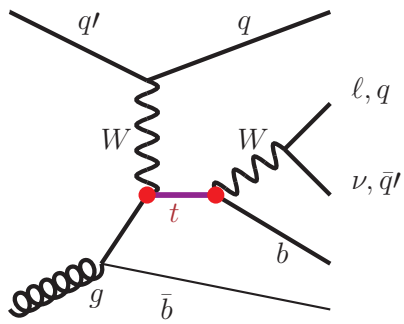

Figure 3.1: Single top t-channel production and decay.

runs at 7 and 8 TeV, some of the definitions change slightly between the two.

3.2.1 Primary Vertex

Primary vertex is the physical location of the initial interaction in a collision. In our analyses we require at least one reconstructed primary vertex, reconstructed from at least 4 tracks, with $|z_{PV}| < 24$ cm and $\rho_{PV} < 2$ cm, where $|z_{PV}|$ and ρ_{PV} are the vertex distances from the nominal interaction point along the z-axis and in the transverse plane, respectively.

Pileup

Pileup causes multiple primary vertices to appear in a collision. Usually, we are interested in only one of them, the one that caused the triggering of the event, which is usually the one with the largest sum of squared momenta associated to it. Those additional collisions make it harder to measure the process of interest. To mitigate these effects, charged particles associated to non-leading primary vertices are vetoed [66].

3.2.2 Relative Isolation

To distinguish isolated leptons from the leptons embedded in jets, we define for a lepton with momentum $p_{T,l}$ the "relative isolation" (I_{rel}):

$$I_{\text{rel}} = \frac{I^{\text{CH}} + max((I^{\gamma} + I^{\text{NH}}), 0)}{p_{T,l}} , \tag{3.1}$$

where I^{CH}, I^{γ}, and I^{NH} are the sum of the transverse energies deposited by stable charged hadrons, photons, and neutral hadrons in a cone of size $\Delta R = 0.4$ around the lepton direction. This definition of isolation is used in the analysis at 7 TeV.

At 8 TeV, we use slightly more complicated definitions. For muons, the relative isolation with the so-called $\Delta\beta$ corrections applies:

$$I_{\text{rel}}^{\beta-corr.} = \frac{I^{\text{CH}} + max((I^{\gamma} + I^{\text{NH}} - I^{\text{PU}}), 0)}{p_{T,l}} , \tag{3.2}$$

where $I^{\text{PU}} \equiv 0.5 \times \sum p_T^{PU}$ is the sum of transverse momenta of tracks associated to non-leading vertices, used to estimate the contribution of neutral particles from pileup events by applying a multiplicative factor 0.5 that takes into account the neutral-to-charged particles ratio expected from isospin invariance.

For electrons, we use relative isolation with rho corrections:

$$I_{\text{rel}}^{\rho-corr.} = \frac{I^{\text{CH}} + max((I^{\gamma} + I^{\text{NH}} - \rho \times A), 0)}{p_{T,l}} , \tag{3.3}$$

where ρ is the average energy of particles not used to build jets, and A is the area of the jet cone in the $\eta - \phi$ plane. The isolation cones for electrons in this case have $\Delta R = 0.3$, while muons still have $\Delta R = 0.4$.

3.2.3 Muons

Tight Muons

The muon decay channel is experimentally defined by the presence of a muon candidate passing "tight" selection criteria. We require the existence of muons, reconstructed with a transverse momentum $p_{\text{T}} > 20$ GeV/c

($p_{\mathrm{T}} > 26$ GeV/c) at at 7 TeV (8 TeV) within the single muon trigger acceptance range $|\eta| < 2.1$. The quality of the candidate has to meet the requirements of a global muon. Furthermore, the track fit is required to have $\chi^2/\mathrm{ndof} < 10$ and at least one valid hit in the muon chambers, more than 10 (5) valid hits in the silicon tracker, out of which at least one in the pixel detector, and at least two segments must match the global muon object in the muon chambers at 7 TeV (8 TeV).

The transverse impact parameter of the muons track with respect to the centre of the estimated beam spot position to suppress the small background due to cosmic-ray muons is required to be smaller than 0.02 cm at 7 TeV, while the absolute 2D impact parameter must be smaller than 0.2 cm at 8 TeV. The distance between the z coordinates of the leading primary vertex and of the muon track at the point of closest approach must be less than 1 (0.5) cm at 7 TeV (8 TeV). Tight muons are required to be isolated with $I_{\mathrm{rel}} < 0.15$ ($I_{\mathrm{rel}}^{\beta-corr.} < 0.12$) at 7 TeV (8 TeV).

Loose Muons

For the purpose of vetoing additional leptons we apply a looser muon selection by selecting PF muon candidates with $p_T > 10$ GeV/c within the full muon acceptance range ($|\eta| < 2.5$), flagged as global muons or tracker muons, with $I_{\mathrm{rel}}(I_{\mathrm{rel}}^{\beta-corr.}) < 0.20$ at 7 TeV (8 TeV).

3.2.4 Electrons

Tight Electrons

Reconstructed PF electrons that are also GSF electrons with a transverse energy $E_{\mathrm{T}} > 30\,\mathrm{GeV}/c$ within $|\eta| < 2.5$ are selected. The ECAL barrel-endcap transition region with $1.4442 < |\eta| < 1.5660$ is excluded from the selection because the reconstruction of an electron in this region is not optimal. Electrons also use a tight requirement on a simple cut based id variable described in [24]. Additionally, no missed inner layers must be present along the electron track to reject electron candidates that originate from a photon conversion to $\mathrm{e}^+\mathrm{e}^-$ pair. Furthermore, the electron candidate is required to pass electron identification criteria based on criteria of shower shape, track cluster matching etc. corresponding to 70% identi-

fication efficiency. The selection relating to impact parameter and primary vertex is the same as for tight muons. The imposed isolation requirement is $I_{\text{rel}} < 0.125$ ($I_{\text{rel}}^{\beta-corr.} < 0.1$) at 7 TeV (8 TeV).

Loose Electrons

The loose electron candidate selection requires an electron with $E_{\text{T}} > 20\,\text{GeV}/c$, $|\eta| < 2.5$, and has to pass the electron identification criteria. The isolation requirement is $I_{\text{rel}} < 0.15$ ($I_{\text{rel}}^{\rho-corr.} < 0.2$) at 7 TeV (8 TeV).

3.2.5 Jets

Jets are reconstructed using the anti-k_T algorithm [47] with a cone size of 0.5, using the PF objects as input for the clusterisation. The jet energy is scaled by a factor that describes the detector response depending on the E_{T} and the η of the jet, To take into account a known difference in jet resolution between data and MC, simulated jets are applied a Gaussian smearing according to η-dependent data-to-MC ratios and their uncertainties [48]

To reduce contamination from pileup events, charged particle candidates not associated to the main primary vertex are subtracted event by event. The energy of the jet is then corrected by the amount of energy deposited by neutral pileup hadrons in the jet area.

The analyses consider PF jets within $|\eta| < 4.5$ whose calibrated transverse energy is greater than 30 (40) GeV at 7 TeV (8 TeV). The jets must have more than one constituent and neutral hadronic energy fraction (including the energy in HF) smaller than 99%. If central ($|\eta| < 2.4$), they must also have charged EM and neutral EM energy fractions smaller than 99%, charged hadronic energy fraction larger than 0 and charged particle multiplicity greater than 1. The event is accepted for further analysis only if at least two such jets are reconstructed.

Once the jets have been selected according to the above criteria, they are further categorised using a b-tagging discriminator variable to distinguish jets originating from light partons from those coming from hadronisation of b-quarks.

Several b-tagging algorithms are available. Some exploit the long B-hadrons lifetime, others their semi-leptonic decay modes and others use kinematic variables related to the high B-meson mass and hard b-quark fragmentation function. Two examples are given below.

The "track counting" (TC) algorithm [67] calculates the signed 3D impact parameter significance (IP/σ_{IP}) of all the tracks associated to the jet that pass tight quality criteria, orders them by decreasing values of this observable, and outputs the value of IP/σ_{IP} for the third track as the jet discriminator. There are two variations of TC, the high efficiency (TCHE) and high purity (TCHP) versions.

The combined secondary vertex (CSV) algorithm [68] is a more sophisticated tagger that exploits all variables known to distinguish b- from non-b jets. The CSV algorithm aims to provide optimal b tagging performance by combining information about the secondary vertex, impact parameter significance, and jet kinematics. The most important property taken advantage of is the relatively large lifetime of b hadrons, which corresponds to a flight distance observable in the tracker ($c \cdot \tau \approx 450\,\mu$m). This leads to the b hadron decay products originating from secondary vertex displaced from the primary. The variables are combined using a likelihood ratio technique or a multivariate classifier to compute the b tag discriminator.

As output, the algorithms produce a b tag discriminator for each jet, on which a more or less tight selection can be performed, with b jets having larger values than non-b jets. In this way, different discriminator values will correspond to different efficiencies and purities for b jet selection. Loose ("L"), medium ("M"), and tight ("T") operating points are defined for all the algorithms with a misidentification probability for light-parton jets of 10%, 1%, and 0.1%, respectively.

Scale factors S_b, S_c and S_l (respectively for true b and c quarks and for light partons) are defined per-jet and depend on p_{T} and $|\eta|$. They are used to get weights per event, defined as $w \equiv P^{data}/P^{MC}$, where P is the probability that an event with a jet multiplicity N_{jets} passes the b-tagging requirements (there are N_{tags} tagged jets and $N_{jets} - N_{tags}$ non-tagged jets):

$$P^{data,MC} = \sum_{i=1}^{N_{jets}} \binom{N_{jets}}{N_{tags}} \prod_{j=1}^{N_{tags}} \epsilon_j^{data,MC}(f_j) \prod_{k=1}^{N_{jets}-N_{tags}} (1 - \epsilon_k^{data,MC}(f_k)) \quad (3.4)$$

where f_i is the flavour (b, c, or light) of $i-$th jet. The signal region considered in our analyses contains both b tagged and non-b-tagged jets, requiring therefore explicit knowledge of the all the efficiencies mentioned. The b-tagging efficiencies $\epsilon(b)$ for true b-quarks, $\epsilon(c)$ for true c-quarks and $\epsilon^{st}(l)$ for true light quarks and gluons are extracted using MC simulation. B tagging is discussed in detail in [69] for 7 TeV and in [70] for 8 TeV.

Light Jet Cleaning

For jets failing the b-tagging requirement, the root-mean-square radius of the particles with respect to the jet axis (RMS) is required to be smaller than 0.025 in the cross section measurement at 8 TeV to reject jets from pileup. This requirement is particularly useful in the forward region of the detector where other quality criteria making use of the tracking system cannot be applied. It is found to improve the agreement of simulation with data. The cleaning is only applied for untagged jets as the b-tagged jet is unlikely to come from pileup because of the presence of high-quality tracks originating from a secondary vertex;

An extra cut on $\Delta R(lepton, jet) > 0.3$ is applied to the jets in the 8 TeV analyses to ensure that the lepton does not come from the jet. This has a negligible effect on b-tagged jets, but improves modelling of untagged jets from multijet QCD events.

Jet and b-tag Counting

The signature of the t-channel single top production contains three partons in the final state, as can be seen in Fig. 3.1, one light quark recoiling against the virtual W boson, one b quark from the top quark decay, and a second b quark from the initial gluon splitting. The second b quark has a softer p_T and a harder η spectrum with respect to the one coming from top decay. As a result, jets stemming from its hadronisation are less likely to be selected due to the p_T cut on the jet, and if selected they are less likely

to be tagged, due to the intrinsic limit on the acceptance ($|\eta| < 2.5$) of the b-tagging algorithms.

Henceforth we will use the notation "$NJMT$" to refer to a sample of events, which have N reconstructed jets, M of which pass the b tagging threshold. For example, 2J1T corresponds to the sample of one b-tagged and one non-b-tagged jet, which is enriched in the t-channel signal. Due to the second b jet detection inefficiency the number of signal events with two reconstructed b jets is one order of magnitude smaller than the number of events with just one b jet. Other notable samples which are studied, primarily to estimate background contributions, are the 2J0T sample, enriched in W+jets, and the 3J1T and 3J2T samples, which are enriched with $\mathrm{t\bar{t}}$ events.

3.2.6 Missing Transverse Energy

Missing transverse momentum, $\vec{p}_{\mathrm{T}}^{\,\mathrm{miss}}$, is defined as the opposite of the vector sum of the PF particles in the event and its magnitude is the missing transverse energy, $\not{E}_{\mathrm{T}}$. A correction to take into account the jet calibration is applied by a propagation of the jet energy corrections to $\not{E}_{\mathrm{T}}$.

3.2.7 Transverse W Boson Mass

To suppress contributions from background processes where the lepton does not come from a leptonically decaying W boson (most notably multi-jet QCD), a selection based on the reconstructed transverse W-boson can be applied. This quantity is constructed from the lepton and neutrino momenta as:

$$m_{\mathrm{T}}(\mathrm{W}) = \sqrt{(p_{T,l} + p_{T,\nu})^2 - (p_{x,l} + p_{x,\nu})^2 - \left(p_{y,l} + p_{y,\nu}\right)^2}\,, \qquad (3.5)$$

where the transverse momentum components of the neutrino are approximated by the components of the missing transverse momentum vector, $\vec{p}_{\nu} = \vec{p}_{\mathrm{T}}^{\,\mathrm{miss}}$.

3.2.8 W-mass Constraint

The first step in the reconstruction of the top quark from its decay products is the reconstruction of the W boson. We assume that the x and y com-

ponents of the missing energy are entirely due to the escaping neutrino, and apply the W-mass constraint in order to extract the z component ($p_{z,\nu}$):

$$m_{\mathrm{W}}^2 = (E_\ell + \sqrt{\not{E}_{\mathrm{T}}{}^2 + p_{z,\nu}^2})^2 - (\vec{p}_{T,\ell} + \vec{p}_{\mathrm{T}}^{\,\mathrm{miss}})^2 - (p_{z,\ell} + p_{z,\nu})^2 \,. \tag{3.6}$$

This equation has in general two solutions:

$$p_{z,\nu} = \frac{\Lambda \cdot p_{z,\ell}}{p_{T,\ell}^2} \pm \sqrt{\frac{\Lambda^2 \cdot p_{z,\ell}^2}{p_{T,\ell}^4} - \frac{E_\ell^2 \cdot \not{E}_{\mathrm{T}}{}^2 - \Lambda^2}{p_{T,\ell}^2}} \,, \tag{3.7}$$

with

$$\Lambda = \frac{m_{\mathrm{W}}^2}{2} + \vec{p}_{T,\ell} \cdot \vec{p}_{\mathrm{T}}^{\,\mathrm{miss}} \,. \tag{3.8}$$

If the discriminant in Eq. (3.7) becomes negative, or equivalently $m_{\mathrm{T}}(\mathrm{W})$ is larger than m_{W}, the solutions have an imaginary component. This happens mostly because of the finite $\not{E}_{\mathrm{T}}$ resolution, while lepton momentum resolution and the intrinsic width of W give negligible contributions.

In the measurements considered here, the imaginary component is eliminated by modifying the neutrino transverse momentum components while keeping the measured $\not{E}_{\mathrm{T}}$ vector fixed, still respecting the m_{W} constraint from Eq. (3.6). This is obtained by imposing that the discriminator, and thus the square-root term in Eq. (3.7), are zero. This condition gives a quadratic relation between $p_{x,\nu}$ and $p_{y,\nu}$, with two possible solutions, among which the one with minimal distance between $p_{T,\nu}$ and $\not{E}_{\mathrm{T}}$ is chosen.

In the case of two real solutions for $p_{z,\nu}$, we choose the solution with the smallest absolute value.

3.2.9 Top Quark Reconstruction

The presence of a top quark is recognisable from a peak in the spectrum of the reconstructed invariant mass of the lepton, b jet and neutrino.

All top quark decay products are reconstructed in the detector, except for the neutrino, which escapes unobserved. The determination of neutrino momentum was discussed in section 3.2.8. We only select events with one charged lepton, and the b-tagged jet is taken as the decay product of the

top quark. In events where the number of b-tagged jets is different from one, we choose the one with largest value of the b-tagging discriminant. The reconstructed top quark mass, $m_{b\mu\nu}$, is an important variable in t-channel analyses.

The light quark jet from single top production (the spectator jet) is identified with the untagged jet in events with one such jet. In events where there number of untagged jets is different from one, we choose the one with the smallest value of the b-tagging discriminant or one in the most forward direction, depending on the analysis.

3.3 Background Processes

The main backgrounds to single top quark production in the t-channel are $t\bar{t}$, W+jets and QCD multijet production processes. Control samples rich in the corresponding events are defined for each of these contributions to check that the variables used in the measurements are reproduced correctly in the simulations.

3.3.1 $t\bar{t}$

A crucial background for single top are the $t\bar{t}$ events. The $t\bar{t}$ decays can be classified as hadronic, semileptonic, or dileptonic if 0, 1, or 2 of the top quarks decay leptonically (i.e. the W-boson from the top quark decay decays leptonically). If in a semileptonic decay two jets are not measured or in a dileptonic decay the second lepton is lost, we get an event that mimics the signal. The control regions for studying $t\bar{t}$ modelling are the ones with a large number of jets including b-tagged jets, namely 3J1T and 3J2T.

3.3.2 W+jets

A large background process contribution comes from the W boson production in association with additional jets (W+jets). A real W boson is produced from quark-antiquark annihilation and the jets arise from gluon radiation. If the W boson decays leptonically, there will be a charged lepton, a neutrino and quarks in the final state, faking the signal topology.

The background can be split to W+light (u,d,s,g) and W+heavy (c,b) flavour jets samples. A b tagging requirement can reduce the W+light flavour jets production significantly, but this background still has a large influence. The control regions for studying W+jets behaviour are the ones without any b-tagged jets, especially 2J0T.

In some cases, we will explicitly distinguish the processes with V+light partons, Wc, and VQ$\overline{\text{Q}}$, with V = W or Z and Q = b or c.

3.3.3 Multijet Events

A large background contribution originates from the QCD multijet production. In principle, the final state of these processes contains only jets, some of which can have the same kinematic properties as the ones from the signal process.

The jets may be misidentified as charged leptons, resulting in an instrumental background. Or, a charged lepton may be produced in a semi-leptonic b hadron decay in the jet.

Additionally, multijet processes can result in a real photon in the final state along with the jets. The photon can overlap with a charged hadron, mimicking the signal of an electron, or interact with the detector material, converting into an electron-positron pair. If one of these misidentified or only one of them is reconstructed, a mimicking of the signal can also occur.

3.3.4 Minor Backgrounds

Single Top *s*- and *tW*-channel

The *s*-channel production of single top quarks also gives rise to two jets in the final state as the *t*-channel, but both tend to be b tagged. The *tW*-channel contains an additional *W*-boson in the final state, giving rise to possible additional leptons or jets in the final state. The cross sections for both of these are smaller than for *t*-channel production and these backgrounds only have a minor effect.

Drell–Yan

The Drell–Yan (DY) background consists of events of Z boson production in association with additional jets (Z/γ^*+jets). If the Z decays leptonically, this leads to two leptons in the final state. The contribution of this background comes if one of the leptons is not reconstructed correctly or not in the acceptance of the detector, being reconstructed as missing energy.

Dibosons

A small background contribution comes from production of WW, WZ and ZZ, collectively called the diboson processes. The behaviour of the W and Z decays was already described above and is the same for diboson production. In the case of ZZ production, one Z decays leptonically Z can decay to jets. The diboson processes have a relatively small cross section.

3.4 Monte Carlo Samples

Single top quark *t*-channel events from MC simulation are generated with the (NLO) MC generator POWHEG interfaced to PYTHIA 6.4.24 for the parton showering simulation. The inherent b quarks are considered among the incoming particles as in figure 1.5 (left) i.e. the 5FS is used in the generation. Signal events have also been generated using the LO generator COMPHEP interfaced with PYTHIA 6 to study systematic uncertainties related to the MC generator. As an alternative NLO generator, used to assess the dependence of the analysis on the modelling of signal in the polarisation analysis, we use aMC@NLO 2.1.2 interfaced with PYTHIA 8.180, with the 4FS, i.e. b quarks in the initial state are only produced via gluon splitting as in the right plot of figure 1.5. In the polarisation analysis, COMPHEP is also used to generate special samples including a Wtb coupling with anomalous structure.

The POWHEG generator interfaced with PYTHIA 6 is also used to model the single top quark tW and *s*-channel events, which are considered as background. The $t\bar{t}$, W boson in association with jets (W+jets), and DY in association with jets (Z/γ^*+jets) processes are generated with MADGRAPH 5.1 interfaced with PYTHIA 6. TAUOLA is used to simulate τ lepton decays. Up to three (four) additional partons are generated at

matrix-element (ME) level in $t\bar{t}$ (W+jets and Z/γ^*+jets) events. A procedure based on the so-called "MLM prescription" [71, 72] is implemented during event generation to avoid double counting phase space regions generated simultaneously by the ME and by the parton shower (PS) simulations. An alternative sample of W+jets generated with SHERPA 1.4.0 at NLO [51, 52] is used to compare the modelling of this background in the polarisation analysis.

The remaining background samples are simulated using PYTHIA 6. These include diboson production, γ+jets, and multijet QCD enriched events with electrons or muons coming from the decays of b and c quarks, as well as muons from the decay of long-lived hadrons. The CTEQ6 [73] parton distribution functions are used for all simulated samples.

A top quark mass of 172.5 GeV/c^2 has been assumed in the simulations. Special signal and background samples are generated with different values of generator parameters (e.g. top quark mass, renormalisation and factorisation scales, etc.), and used to estimate the corresponding systematic uncertainties.

All single top quark processes are normalised to approximate NNLO predictions [74]. Top quark pair production is normalised to a complete NNLO prediction in QCD that includes soft gluon resummation to next-to-next-to-leading-log order, as calculated with the Top++2.0 program [75, 76]. The W+jets and Z/γ^*+jets production cross sections times branching fraction are calculated at NNLO with FEWZ [77]. The diboson cross sections are calculated at NLO with MCFM 5.8 [78].

The theoretical predictions for the cross sections of different processes are listed in table 3.1.

3.5 Single Top t-channel Event Selection

All the analyses in this work follow the same general idea when performing event selection. That is, we wish to end up with a high purity sample of t-channel single top quark events, which can be used to measure the quantity of interest. Reconstruction of particles and a preliminary selection was described in section 3.2. Here we describe how to obtain a t-channel sample with high purity. The analyses themselves are covered in the following chapters.

Table 3.1: Central values for cross sections of different processes used in the measurements calculated as described in section 3.4.

	Process	$\sigma(\cdot BR)$[pb] (7 TeV)	$\sigma(\cdot BR)$[pb] (8 TeV)
Single top	t-channel, t	41.80	56.4
	t-channel, $\bar{t}$	22.02	30.7
	s-channel, t	2.76	3.79
	s-channel, $\bar{t}$	1.52	1.76
	tW channel, t	7.87	11.19
	tW channel, $\bar{t}$	7.87	11.19
	$t\bar{t}$	177.31	245.8
	$W(\rightarrow l\nu) + jets$	31314	36257.2
	$Z/\gamma^*(\rightarrow l^+l^-) + jets$, $m_{\mathrm{ll}} > 50\,\mathrm{GeV}/c^2$	3048	3503.71
	WW	43	54.838
	WZ	18.2	32.3161
	ZZ	5.9	8.059
	γ+jets, $40 < H_T < 100\,\mathrm{GeV}/c$	23620	
	γ+jets, $100 < H_T < 200\,\mathrm{GeV}/c$	3476	
	γ+jets, $H_T > 200\,\mathrm{GeV}/c$	485	1008
Multijet QCD	μ-enriched, $\hat{p}_T > 20\,\mathrm{GeV}/c$, $p_T^{\mu} > 15\,\mathrm{GeV}/c$	$8.5 \cdot 10^4$	$1.35 \cdot 10^5$
	$b/c \rightarrow e$, $20 < \hat{p}_T < 30\,\mathrm{GeV}/c$	$1.32 \cdot 10^5$	$1.67 \cdot 10^6$
	$b/c \rightarrow e$, $30 < \hat{p}_T < 80\,\mathrm{GeV}/c$	$1.37 \cdot 10^5$	$1.67 \cdot 10^5$
	$b/c \rightarrow e$, $80 < \hat{p}_T < 170\,\mathrm{GeV}/c$	9360	$1.30 \cdot 10^4$
	$b/c \rightarrow e$, $\hat{p}_T > 170\,\mathrm{GeV}/c$		758
	EM-enriched, $20 < \hat{p}_T < 30\,\mathrm{GeV}/c$	$2.45 \cdot 10^6$	$2.91 \cdot 10^6$
	EM-enriched, $30 < \hat{p}_T < 80\,\mathrm{GeV}/c$	$3.87 \cdot 10^6$	$4.6 \cdot 10^6$
	EM-enriched, $80 < \hat{p}_T < 170\,\mathrm{GeV}/c$	$1.39 \cdot 10^5$	$1.83 \cdot 10^5$
	EM-enriched, $\hat{p}_T > 170\,\mathrm{GeV}/c$		5233

3.5.1 Trigger Selection

In the detector, we use a HLT for single muons (with an additional isolation requirement or not) or single electrons, selecting events which contain a muon or an electron above a specified p_{T} threshold and in an $|\eta|$ range. For a subset of the data at 7 TeV, a trigger selecting an electron along with a jet is used. For consistency, the same trigger requirement is applied for MC.

3.5.2 Lepton Counting

In the rest of this thesis, "lepton" will signify either a muon or an electron. Tau particles and neutrinos are considered separately because of the different nature of their detection.

We require the presence of exactly one tight lepton. To reduce the contribution of dilepton events, which can come from $\mathrm{t\bar{t}}$ or from DY processes, we veto events with additional loose muons or electrons.

3.5.3 Rejection of Multijet Events

The QCD multijet background can not be sufficiently well modelled with MC simulations. The cross section of multijet production is very large and it is not possible to simulate enough events to cover the full phase space. In our case, the acceptance after the selection cuts is too small, as we end up with only a small number of events and thus can not reliably estimate the shapes of multijet event distributions because only extreme kinematic regions pass the selection, and tail effects are the most difficult to simulate properly. As a result the multijet background has to be studied in situ on data taken by the experiment.

For the muon channel, this sample is selected by inverting the muon isolation requirement, i.e. selecting events with muons $I_{\mathrm{rel}} > 0.2$ instead of tight muons. For the electron channel, the selected electron is required to fail at least two of the three following quality requirements: $I_{\mathrm{rel}} < 0.1$, the distance of closest approach to the primary vertex on the x-y plane $\delta_{xy} <$ 0.02 cm, and the electron identification criteria discussed in section 3.2.4.

The $m_{\mathrm{T}}(\mathrm{W})$ variable for muons and the $\not\!\!E_{\mathrm{T}}$ variable for electrons are used for rejecting multijet events. This is because this process consists of jets

and does not contain W bosons or neutrinos in the final state. Although $\not{E}_T$ has lower discriminating power that $m_T(W)$, it is not dependent on the lepton-$\not{E}_T$ angular correlations and is overall more robust in the electron channel. In the cross section analyses, we select events with $m_T(W) > 40(50)\,\text{GeV}/c^2$ in muon channel at 7 TeV (8 TeV). In electron channel the $\not{E}_T > 35(45)\,\text{GeV}$ at 7 TeV (8 TeV) requirement is applied instead. In the polarisation analysis, we use a boosted decision tree (BDT) trained on multiple variables to reject multijet events.

To estimate the amount of multijet events remaining after the selection, we use the same variable to perform a two-component fit. The components are the distributions of multijet events, extracted from the selection with inverted isolation, and the summed contribution of other processes.

3.5.4 Signal Purification

The distribution of the pseudorapidity ($|\eta_{j'}|$) of the recoil jet originating from the fragmentation of a light quark in the *t*-channel scattering extends to larger valuer than for the background processes because the light parton recoils against a much heavier particle in the top quark. These forward regions in the $|\eta_{j'}|$ spectrum correspond to the tails of the distribution for SM processes. Therefore, this variable provides a useful handle to further purify our selection.

In 2J1T and in 3J2T samples it is defined as the pseudorapidity of the untagged jet. In 3J1T it is defined as the pseudorapidity of the jet with the smallest b-discriminator value. And in 2J0T, it is defined by taking the pseudorapidity of each of the two jets, and two entries per event are present.

In the cross section measurements, we select on the absolute value of this variable: $|\eta_{j'}| > 2.5$ in 2J1T. Furthermore, we use $m_{b\mu\nu}$ to further divide the 2J1T category into a *t*-channel enriched signal region (SR), defined by selecting events within the mass range $130 < m_{b\mu\nu} < 220\,\text{GeV}/c^2$, and a W boson and $t\bar{t}$ enriched sideband region (SB), defined by selecting events that are outside this $m_{b\mu\nu}$ window. In the polarisation measurement, we train a BDT that includes both of these variables and also additional ones.

The final event yields are obtained by a maximum-likelihood (ML) fit to the distribution of $|\eta_{j'}|$, or to the BDT distribution in the polarisation measurement. The fits are performed with the theta package [79]

4 Statistical Methods

4.1 Boosted Decision Trees

In the following, we briefly describe BDT classifiers, that are used in this work for discriminating between signal and background events. A more comprehensive overview of the discussed concepts can be found in [80].

4.1.1 Decision Trees

Decision trees are a popular way of representing the outcome of classification learning. They partition the feature space into a set of hyper-rectangles, and then fit a simple model, usually a constant, in each one. The partitioning rules can be summarised in the form of a tree, giving the method its name. The evaluation of new data points is performed by traversing the tree and finding the terminal node it corresponds to, i.e. we classify an observation as belonging to the most common class of training observations in the hyper-rectangle it is located in.

Various tree-growing algorithms use different methods to find the optimal partitions. Usually we try to minimise a measure of node impurity by the partition. One such measure is cross entropy, given for the case of two classes by:

$$-p \log p - (1-p) \log (1-p), \tag{4.1}$$

where p is the proportion of one of the classes at the node. The minimisation of cross entropy is weighed by the number of events in a node. Other measures, like Gini index or misclassification error, behave in a quite similar way.

Pruning is the procedure of reducing tree size to avoid overfitting. Usually a large tree is constructed first, and then pruned, as a seemingly poor partition might lead to good partitions further down the tree. Pruning is done by collapsing internal nodes in the tree and in this way finding a tree that minimises the fit error penalised by the number of nodes in the tree.

Tree-based supervised learning methods are simple and useful for interpretation, but typically not competitive with the best approaches in terms of prediction accuracy. Methods such as bagging, random forests, and boosting are used to grow multiple trees which are combined to return a single prediction. These methods are often much improved in prediction accuracy compared to decision trees, but with reduced interpretation power.

4.1.2 Boosting

Boosting is a general approach applicable to various statistical learning methods, but it is most frequently used for decision trees. Using a single large decision tree is prone to overfitting. In boosting, new trees are fitted sequentially to the data to improve this behaviour, taking into account the trees already there and trying to improve classification for the examples wrongly classified by the existing set of trees. New trees, each of the which can have just a small number of terminal nodes, are added to the model to update the residuals. The maximum tree depth parameter is used to limit the size of the trees in the algorithm. In this way classifier slowly improves in areas with poor performance. The shrinkage parameter λ is used to assign weights (≤ 1) to new trees, and this slows the process down even further.

4.1.3 Parameter Choice and Ranking

For selecting parameters to use in a statistical model, the most straightforward approach is to use best subset selection, which basically amounts to building a model with every possible combination of variables and then comparing them. For larger number of parameters, this is not computationally feasible and can also lead to overfitting. For these reasons, stepwise models, which explore a much smaller set of models due to a greedy approach, are preferred.

Forward Stepwise Selection (FSS) starts with a model containing no predictors and continues by adding variables one at a time in such a way that at each step, the variable giving the biggest additional improvement is chosen. The process continues until all the variables are added to the model.

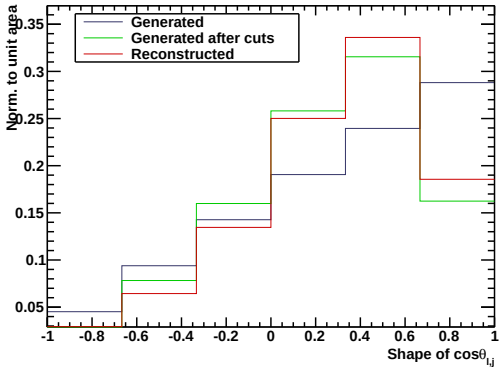

Figure 4.1: $\cos\theta^*_\mu$ distribution on generator level before and after the event selection and after the reconstruction.

Backward Stepwise Selection (BSS) takes the opposite approach – we begin with all the variables included in the model and start removing them one by one, picking the one that worsens the prediction power of the model the least. The procedure is repeated until there are no more variables left.

The FSS and BSS procedures also naturally produce a ranking of the variables. The models produced can then be validated and compared on independent test data.

4.2 Unfolding

Figure 4.1 shows the distributions of the sensitive variable on generator level before and after the event selection and on reconstruction level. One can clearly see how the shapes of the distribution are affected by the selection and reconstruction steps.

To compare the performed measurement with theories or different experiments, we are often interested in obtaining the "true" parton-level distribution. That is also the case in the measurement of single top polarisation, described in section 7. However, it can be the case that the true distribution x of variable X is not directly accessible to measurement.

Instead, we observe a sample of values y from the distribution of a random variable Y, which is different from X. The finite resolution of the detector causes the measured values not to be exact (moving an event from one bin to another in figure 4.1). The limited acceptance of the detector means not all events are measured, and the efficiency depends on the value of X, which can be seen especially in the last bin of figure 4.1. There can also be non-linear effects of the detector response, e.g. loss of energy in the detector, which can change the shape of the distribution. Unfolding refers to the problem of estimating the true distribution of some physical quantity X using observations of Y made by an imperfect measurement device.

We follow the regularised unfolding procedure described in [81]. The unfolding algorithm corrects the measured spectrum for migration and efficiency effects by applying a generalised matrix inversion method, which has been used in top quark measurements before, for example in [82, 83]).

The translation of the true spectrum x into the measured spectrum y is defined as:

$$\vec{y} = A(x, y) \cdot \vec{x}, \tag{4.2}$$

where $A(x, y)$ is the transition matrix, which accounts for migration and efficiency and $\vec{y}$ and $\vec{x}$ are used to denote the binned distributions y and x in vector form, where each bin is a vector component. The binning of the distributions is chosen in such a way that the number of bins in the reconstructed spectrum is twice as high as in the unfolded spectrum to improve the stability of the unfolding procedure. A is not known analytically, but can be derived from MC simulation, as for each reconstructed event we know the true value of X. This matrix can be factorised as the product of the migration matrix and a diagonal matrix with the efficiencies for each of the bins on the diagonal, and all other elements set to zero. These matrices are illustrated in figure 4.2, showing the event selection efficiency and migration for the $\cos\theta^*_\mu$ variable in simulated t-channel single top events generated with POWHEG, used in the polarisation measurement.

Solving equation 4.2 can be formulated as a least-squares problem. However, this is an ill-posed problem – in general, the solution is unstable and shows huge fluctuations for small changes in $\vec{x}$. To avoid this problem, a regularisation term is introduced [84], which dampens the unphysical

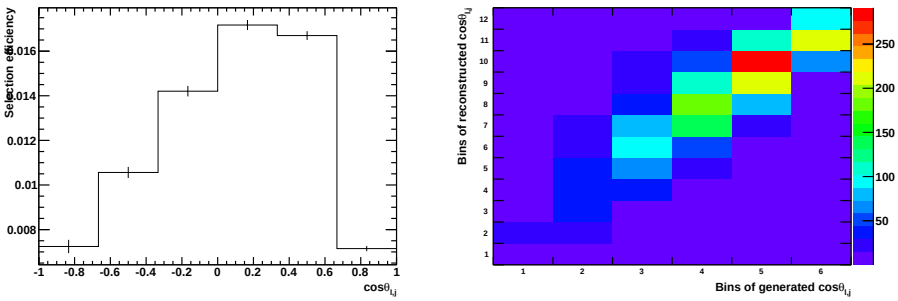

Figure 4.2: Selection efficiency (left) and migration (right) matrices for single top events.

fluctuations, but introduces a bias towards the input distribution. The mathematical details of the unfolding approach can be found in [81]. In practice, we use the package TUnfold [85] for unfolding.

5 Systematic Uncertainties

A number of systematic uncertainties are taken into account in the measurements discussed in this work. Below, we describe the systematic uncertainties common to more than one analysis. Those specific to a certain measurement are discussed in their respective sections. The jet energy scale and jet energy resolution uncertainties are fully correlated across all simulated samples. The matching and scale uncertainties are fully correlated between W+jets and Z/γ^*+jets, but are uncorrelated with $t\bar{t}$.

Jet Energy Scale (JES), jet energy resolution (JER), and missing transverse energy: All reconstructed jet four-momenta in simulated events are changed simultaneously according to the η and p_T-dependent uncertainties on the jet energy scale [86].

A smearing is applied to account for the known difference in jet energy resolution relative to data [87], increasing or decreasing the extra resolution contribution by the uncertainty on the resolution.

The variation of jet momenta causes the total momentum in the transverse plane, which is propagated to $\not{E}_T$, to change. The component of the $\not{E}_T$ that is not due to particles reconstructed as leptons and photons or clustered in jets ("unclustered $\not{E}_T$") is varied by $\pm 10\%$ [48].

b Tagging. Both b tagging and misidentification efficiencies in the data are estimated from control samples [69]. In the polarisation measurement this is done as described in [70]. Scale factors are applied to simulated samples to reproduce the measured efficiencies. The corresponding uncertainties for individual jets are propagated as systematic uncertainties.

Lepton Trigger and Reconstruction. Single lepton trigger efficiencies as a function of the lepton η and p_T are estimated with a "tag and probe" method from Drell–Yan data [88]. The efficiencies of triggers requiring a lepton plus a b tagged jet are parametrised as a function of the jet p_T and the value of the TCHP b-tag discriminator. The selection efficiencies have been validated using a reference trigger. The effect of the incorrect determination of the muon charge is negligible, while for electrons, the

uncertainty on the determination of the charge has been measured at $\sqrt{s} = 7\,\text{TeV}$ in ref. [89]. The polarisation analysis (in section 7) uses a systematic uncertainty of 1% for to the muon trigger, identification, and isolation efficiencies to cover the efficiency differences between the phase space regions sampled by this analysis and by the selection of Z/γ^*+jets events for the tag and probe procedure.

Pileup. The effect of pileup is evaluated by reweighting simulated samples to reproduce the expected number of pileup interactions in data, properly taking into account in-time and out-of-time pileup contributions. The uncertainty on the expected number of pileup interactions (5%) is propagated as a systematic uncertainty.

Limited MC Simulation Sample Size. The uncertainty due to the limited amount of MC events in the templates used for the statistical inferences is determined by using the Barlow–Beeston method [90, 91]. The limited number of simulated events can also influence the estimation of other systematic uncertainties, potentially leading to an overestimation of the associated uncertainties.

Luminosity. The luminosity is known with a relative uncertainty of $\pm 2.2\%$ [92] at 7 TeV and with $\pm 2.6\%$ [93] at 8 TeV.

Background Normalisation in the Cross Section Measurements. The uncertainties on the normalisation of each background source are listed below. They are propagated as systematic uncertainties in the cross section analyses only for dibosons and *s*- and tW-channel single top processes, while the remaining backgrounds are estimated from data. The uncertainty on the following processes is used as a Gaussian constraint in the signal-extraction fit.

- $t\bar{t}$: $\pm 15\%$, based on the statistical uncertainties in Ref. [94] at 7 TeV, $\pm 10\%$ at 8 TeV, covering the difference between theoretical predictions in [74] and [95].
- Dibosons, single top quark *s*- and tW-channels at 7 TeV: $\pm 30\%$, $\pm 15\%$, $\pm 13\%$, respectively, based on theoretical uncertainties. At 8 TeV, $\pm 30\%$, motivated by refs. [78, 74].

Multijet Events Background Yield: A 50% uncertainty is assigned to the yield obtained from the multijet events fit. (100% for the electron channel in the *7TeV* cross section analysis)

Renormalisation and Factorisation Scales. The uncertainties on the renormalisation and factorisation scales (set to a common scale equal

to the momentum transfer Q in the event) are studied with dedicated samples of single top, W+jets, Z+jets, and $t\bar{t}$ events. They are generated by doubling or halving the renormalisation and factorisation scale with respect to the nominal value equal to the Q^2 in the hard-scattering process.

In the polarisation analysis, the number of the events in these samples is low for the kinematic region of interest, so we use a reweighting procedure based on the nominal simulated samples as follows. For the signal, a reweighting procedure is applied to simulated events using the simplification of neglecting the scale dependence of the parton shower (PS). Since the signal process does not contain a QCD vertex at LO in the 5FS, the dependence of its cross section with scale Q can be written as:

$$\sigma^{\mathrm{LO}}_{t\text{-ch.}}(Q) = \int_0^1 \mathrm{d}x_1 f_{\mathrm{PDF}}(x_1, Q^2) \int_0^1 \mathrm{d}x_2 f_{\mathrm{PDF}}(x_2, Q^2)\, \hat{\sigma}(x_1, x_2), \tag{5.1}$$

where x_i are the momentum fractions of the two partons in the colliding protons, $f_{\mathrm{PDF}}(x_i, Q^2)$ is the PDF, and $\hat{\sigma}(x_1, x_2)$ denotes the partonic cross section. The event reweighting to a different scale Q' is then defined using a factor

$$w_{Q\to Q'}(x_1, x_2) = \frac{f_{\mathrm{PDF}}(x_1, Q'^2)\, f_{\mathrm{PDF}}(x_2, Q'^2)}{f_{\mathrm{PDF}}(x_1, Q^2)\, f_{\mathrm{PDF}}(x_2, Q^2)}. \tag{5.2}$$

The dedicated simulated samples with doubled and halved scales are used to verify the validity of the approximation of ignoring the effect of scale in PS simulation for the signal process. The reweighting is preferred over use of these dedicated samples because of their limited number of events.

For the $t\bar{t}$ and W+jets backgrounds, a looser selection is applied in simulated samples that have a changed Q scale to increase the number of selected events. This provides a $\cos\theta^*_\mu$ distribution that agrees, within the limited statistical uncertainty of the simulation, with the shape obtained by applying the nominal $\mathrm{BDT}_{\mathrm{W}/t\bar{t}}$ discriminant threshold.

Matrix Element/Parton Shower Matching Threshold. The uncertainty due to extra hard parton radiation is studied using dedicated samples in which the threshold for the MLM jet matching scheme [71] is either doubled or halved, independently for W+jets, Z+jets, and $t\bar{t}$ processes.

Signal Generator. The results obtained by using the nominal POWHEG signal samples are compared with the result obtained using signal samples generated by COMPHEP. Half of the difference is taken as systematic

uncertainty. In general, the largest model deviations occur in the kinematic distributions of the spectator b quark [96].

The polarisation analysis uses an unfolding matrix from a signal sample generated with aMC@NLO, interfaced with PYTHIA 8 for parton showering for comparisons with the nominal result, taking the difference as a systematic uncertainty.

Parton Distribution Functions. The uncertainty due to the choice of the parton distribution functions (PDF) is estimated using pseudo-experiments, reweighting the simulated events with each of the 40 eigenvectors of the CTEQ6 [73] PDF set and the central set of CTEQ10 [60], and repeating the nominal signal extraction procedure. For reweighting the simulated events, the LHAPDF [97] package is used, according to the PDF4LHC recommendations [63]. At 8 TeV, we use the envelope of the CT10 [60], MSTW [61, 98], and NNPDF [62] PDF sets as the uncertainty.

6 Measurement of Single Top Quark Cross Section

6.1 Measurement of Single Top Quark Cross Section at 7 TeV

6.1.1 Introduction

The first measurements of the single top quark t-channel production cross section in pp collisions at 7 TeV were performed by CMS [99] and ATLAS [100]. The analysis documented in [1], which is discussed in the following, extends the previous CMS measurement [99] of the t-channel cross section to a larger data set. The measurement is based on pp collision data at $\sqrt{s} = 7\,\text{TeV}$ collected during 2011 with the CMS experiment, corresponding to integrated luminosities of 1.17 and 1.56 fb^{-1} with muon and electron final states, respectively. Events with leptonically decaying W bosons are selected: $\text{t} \to \text{bW} \to \text{b}\ell\nu$ ($\ell = \text{e}$ or μ).

Previous measurements are compatible with expectations based on approximate NLO and next-to-next-to-leading logarithm (NNLL) perturbative QCD calculations. In these, the t-channel cross section for a top quark mass of $m_\text{t} = 172.5\,\text{GeV}/c^2$ is expected to be [101]:

$$\sigma^\text{th}_{t\text{-ch.}} = 64.6^{+2.1}_{-0.7}\,(\text{scale})^{+1.5}_{-1.7}(\text{PDF})\,\text{pb}. \tag{6.1}$$

The uncertainties are due to the PDFs and the missing higher-order corrections, which are estimated by varying the factorisation and renormalisation scales by a multiplicative factor of 0.5 or 2.0.

The selection is performed as described in section 3.5 and then measurements with two complementary approaches are performed. The first approach exploits the $m_{\text{b}\mu\nu}$ and $|\eta_{\text{j}'}|$ distributions and is referred to as the $|\eta_{\text{j}'}|$ analysis. It is straightforward with little model dependence. The

second approach uses multivariate classifiers to optimise the discrimination between signal and background. Because of the complexity involved in this, two independent multivariate analyses cross-checking each other are conducted, one based on a NN and the other on a BDT. The description of the multivariate analyses can be found in [1], and will not be discussed here further, except for the results. After validating the consistency of the results, the final result is determined by combining the three analyses.

6.1.2 Event Selection and Reconstruction

The HLT for the muon channel is based on the presence of at least one isolated muon with $p_T > 17\,\text{GeV}/c$. For the electron channel, an isolated electron trigger with $p_T > 27\,\text{GeV}/c$ was used for the initial data-taking period, corresponding to an integrated luminosity of 216 pb^{-1}. For the remaining data-taking period, a trigger selecting at least one electron with $p_T > 25\,\text{GeV}/c$ and a jet with $p_T > 30\,\text{GeV}/c$ was used. The jet is identified in the trigger processing as coming from a fragmentation of a b quark using the TCHE b tagging algorithm. In the offline analysis, the TCHP discriminator is used for b tagging

The signal content is extracted from the 2J1T SR, with 2J1T SB, 2J0T and 3J2T used to check background modelling. The modelling of $\text{t}\bar{\text{t}}$ background is checked in the 3J2T category. In general, the event yields are reasonably well reproduced by the simulation within the systematic uncertainties. The shapes of the relevant variables, $|\eta_{\text{j}'}|$ and $m_{\text{b}\mu\nu}$, show good agreement between data and simulation. The estimation of QCD multijet background is described in section 6.1.3. The determination of W+jets background is described in section 6.1.4 and signal extraction is section 6.1.5.

The event yield in the SR is summarised in table 6.1 for the muon and electron channels, together with expectations from simulated signal and backgrounds, and for QCD multijet events, which are determined from control samples of data, as described in section 6.1.3.

6.1.3 QCD Multijet Background Estimation

The yield of the QCD multijet background is measured by performing maximum-likelihood (ML) fits to the distributions of $m_T(\text{W})$ in the muon channel and $\not{E}_T$ in the electron channel, separately for different $NJMT$

Table 6.1: Event yield with statistical uncertainties of the $|\eta_{j'}|$ analysis for the signal and main background processes in the signal region, after applying the $m_{b\mu\nu}$ mass requirement for the μ and e channels. The yields are taken from simulation except for the QCD multijet yield, which is obtained from control samples of data as described in section 6.1.3. The normalisation of the Wc($\bar{c}$) and Wb($\bar{b}$) processes is further discussed in section 6.1.4.

Process	Muon yield	Electron yield
t-channel	617 ± 3	337 ± 2
tW channel	107 ± 1	70.2 ± 0.9
s-channel	25.6 ± 0.5	14.7 ± 0.4
$t\bar{t}$	661 ± 6	484 ± 5
W + light partons	92 ± 7	38 ± 4
Wc($\bar{c}$)	432 ± 14	201 ± 9
Wb($\bar{b}$)	504 ± 14	236 ± 10
Z + jets	87 ± 3	13 ± 1
Dibosons	23.3 ± 0.4	10.7 ± 0.3
QCD multijet	77 ± 3	62 ± 3
Total	2626 ± 22	1468 ± 16
Data	3076	1588

categories. We assume the parametrisation:

$$F(x) = a \cdot S(x) + b \cdot B(x), \tag{6.2}$$

where x is $m_{\mathrm{T}}(\mathrm{W})$ or $\not{E}_{\mathrm{T}}$ for the muon and electron channels, respectively. $B(x)$ is the expected distribution for QCD multijet events and $S(x)$ is the expected distributions for the sum of all other processes. The function $S(x)$ is taken from simulation, while $B(x)$ is extracted directly from data samples enriched in QCD multijet events, which are described in section 3.5.3.

The fit is used to determine the parameters a and b. The QCD multijet background yield is estimated to be the area under the fitted curve $b \cdot B(x)$ in the range $m_{\mathrm{T}}(\mathrm{W}) > 40\,\mathrm{GeV}/c^2$ for the muon channel and $\not{E}_{\mathrm{T}} > 35\,\mathrm{GeV}$ for the electron channel, as discussed in section 3.5.3. The fit is performed on the entire 2J1T sample, without separating it to SR and SB, to keep

statistical uncertainty down. The results for the SR and SB regions are determined by scaling the total yield from the fit by the fraction of QCD multijet events in the two regions (SB and SR) of the $m_{\mathrm{b}\mu\nu}$ distribution. The QCD multijet fits are shown in figure 6.1 and the yields in the SR are reported in table 6.1.

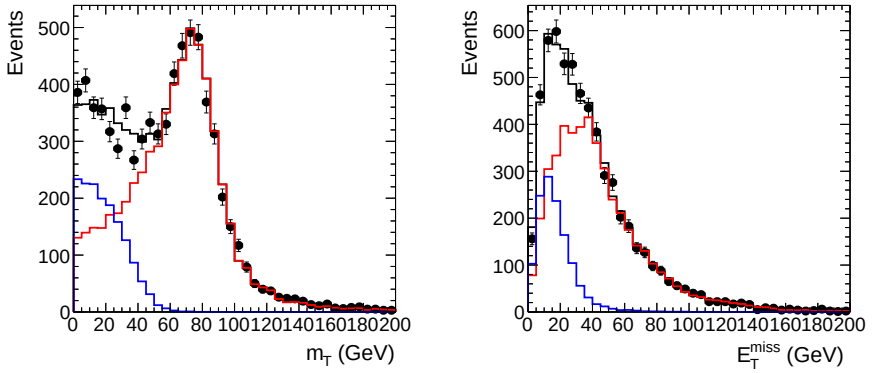

Figure 6.1: QCD multijet fit of the $m_{\mathrm{T}}(\mathrm{W})$ distribution for muons (left) and the fit of the $\not{E}_{\mathrm{T}}$ distribution for electrons (left). Blue line is the QCD multijet template, red line the non-multijet component.

Several cross checks have been performed to check the stability of the fit. One is repeating the measurement with the distribution $B(x)$ obtained from QCD multijet simulation. Another performed check is to invert the choice of $x = m_{\mathrm{T}}(\mathrm{W})$ or $\not{E}_{\mathrm{T}}$ between the muon and electron channels. The results of the different cross checks are used to assign relative uncertainties on the QCD multijet yield estimates of $\pm 50\%$ for the muon channel and $\pm 100\%$ for the electron channel, which conservatively cover the results of all of the cross checks.

6.1.4 W+Jets Background Estimation

A check of the modelling for the W+jets background is carried out in the 2J0T category, which is highly enriched in W+light jet events.

Table 6.1 shows a difference between the total observed and expected yields. This difference can be attributed to excesses in data for the Wb+X and Wc+X processes. The ATLAS collaboration has reported that the

fiducial W+b-jet cross section in the lepton and one or two jets final state is a factor of 2.1 larger than the NLO prediction, but is still consistent at the level of 1.5 standard deviations with this SM prediction [102].

Motivated by these observed excesses in comparison to the SM NLO calculations, we determine the W/Z+jets background yield and $|\eta_{j'}|$ distribution from data. The jets in 2J0T originate mostly from light quarks (u, d, s) or gluons. These tend to behave differently from heavy-flavour jets from c and b quarks, and thus we use the SB region, which has a similar composition in terms of W/Z+heavy flavours as 2J1T SR, to extract the $|\eta_{j'}|$ distribution for W/Z+jets. This is done by subtracting the $|\eta_{j'}|$ contributions of all other processes from the data. These $|\eta_{j'}|$ distributions and event yields for the subtractions are taken from simulations of $t\bar{t}$, single top and diboson production, with the signal scaled to SM cross section prediction. The QCD multijet event yield and $|\eta_{j'}|$ distribution are extracted from data and extrapolated to the SB as described in section 6.1.3. The $|\eta_{j'}|$ distribution for W/Z+jets processes in the SB is therefore used in the SR for the signal extraction procedure (described in section 6.1.5), assuming that the shapes in the SB and SR are compatible with each other.

The compatibility of the distributions in the two regions has been verified through Kolmogorov–Smirnov (KS) and χ^2 compatibility tests. For the muon channel, the KS test yields a p-value of 0.47, and the χ^2 test a p-value of 0.63, while for the electron channel, the p-values are 0.51 and 0.60, respectively. The stability of the extracted shape has been tested by varying the sample composition in terms of $t\bar{t}$ and signal fractions by 20% and 100%, respectively. The extracted shapes are compatible with a p-value greater than 0.9 in both cases.

6.1.5 Signal Extraction

The signal yield is extracted using a ML fit to the observed distribution of $|\eta_{j'}|$, which is performed with four components. The signal distribution for the fit is taken from simulation. The EW background component consists of the W/Z+jets contribution normalised to the value obtained from the procedure described in section 6.1.4, plus the diboson processes. Both of the signal and EW components are unconstrained. The top quark component consists of $t\bar{t}$ and single top s- and tW-channels, with a Gaussian constraint on the yield. The QCD multijet component is fixed to the result

determined in section 6.1.3. The fit is performed separately for muon and electron channels as well as simultaneously for both to obtain a combined result. Figure 6.2 shows the distribution of $|\eta_{j'}|$ obtained from the fit.

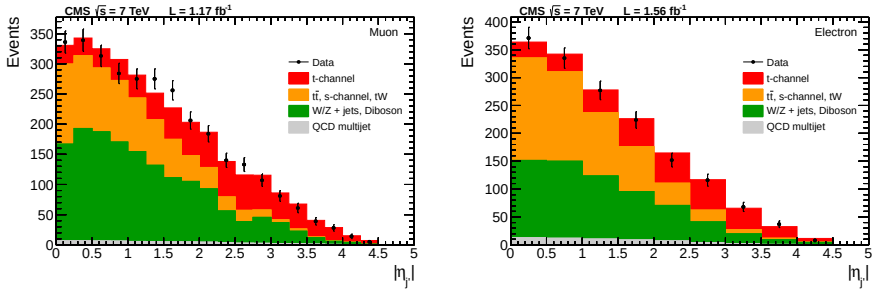

Figure 6.2: Result of a simultaneous fit to $|\eta_{j'}|$ in the muon (left) and electron (right) decay channels.

The fit results in a signal yield of N_s, which can be used to calculate the cross section according to the formula:

$$\sigma_t = \frac{N_s}{\epsilon \cdot \mathcal{B}(t \to \ell\nu b) \cdot L}, \tag{6.3}$$

where ϵ is the signal selection efficiency, $\mathcal{B}(t \to \ell\nu b) = 0.1080$ [7] is the leptonic branching fraction of the top quark and L is the integrated luminosity. For the muon and electron channels, the signal selection efficiencies are estimated from simulation to be $\epsilon_{mu} = 0.84\%$ and $\epsilon_{ele} = 0.35\%$, respectively.

To further purify the sample single top quark events, we select events with $|\eta_{j'}| > 2.8$. Figure 6.3 shows the distribution of $m_{b\mu\nu}$ after this selection, normalised to the fit results to illustrate that the modelling is correct after applying the fit results.

The pure selection enables to also have a look at t-channel distributions of other variables of interest. Figure 6.4 depicts the observed charge asymmetry and the $\cos\theta^*$ distributions for combined muon plus electron events.

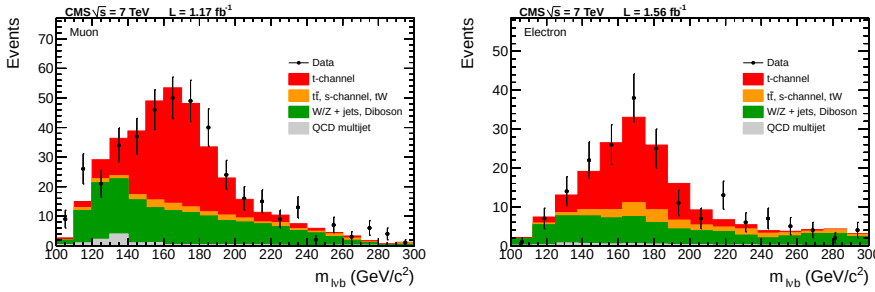

Figure 6.3: Distributions of $m_{b\mu\nu}$ requiring $|\eta_{j'}| > 2.8$, for muons (left) and electrons (right), obtained by normalising each process yield to the value from the fit. Because of limited simulated data, the background distribution is smoothed by using a simple spline curve.

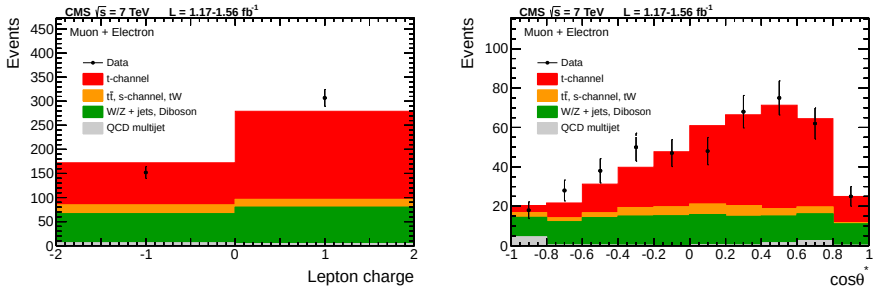

Figure 6.4: Distinct single top quark t-channel features in the SR for $|\eta_{j'}| > 2.8$, for the electron and muon final states combined. The charge of the lepton (left) and $\cos\theta^*$ (right). All processes are normalised to the fit results. Because of limited simulated data, the background distribution is smoothed by using a simple spline curve (right).

6.1.6 Systematic Uncertainties and Measurement Sensitivity

The systematic uncertainties are evaluated by pseudo-experiments, which are generated taking into account the effect of the corresponding systematic source on the distribution of $|\eta_{j'}|$ and on the event yield of the

Table 6.2: Sources of uncertainty on the cross section measurement.

	Uncertainty source	Magnitude
Experimental uncert.	Statistical	$\pm 8.5\%$
	Limited MC data	$\pm 0.9\%$
	Jet energy scale	$-3.9/+4.1\%$
	Jet energy resolution	$-0.7/+1.2\%$
	b tagging	$\pm 3.1\%$
	Muon trigger + reco.	$-1.5/+1.7\%$
	Electron trigger + reco.	$-0.8/+0.9\%$
	Hadronic trigger	$\pm 3.0\%$
	Pileup	$-0.3/+0.2\%$
	$\not{E}_T$ modelling	$\pm 0.5\%$
Backg. rates	W+jets	$\pm 5.9\%$
	$t\bar{t}$	$\pm 3.3\%$
	QCD, muon	$\pm 0.9\%$
	QCD, electron	$-0.4/+0.3\%$
	s-, tW ch., dibosons, Z+jets	$\pm 0.5\%$
	Luminosity	$\pm 2.2\%$
Theor. uncert.	Scale, $t\bar{t}$	$-4.0/+2.1\%$
	Scale, *t*-, *s*-, tW channels	$-2.2/+2.3\%$
	Matching, $t\bar{t}$	$\pm 0.4\%$
	t-channel generator	$\pm 2.5\%$
	PDF	$\pm 2.5\%$
	Total theor. uncertainty	$-5.6/+4.9\%$
Syst. + theor. + luminosity uncert.		$\pm 10.8\%$
Total (stat. + syst. + theor. + lum.)		$\pm 13.8\%$

physics processes. Pseudo-experiments are generated separately with templates varied by $\pm 1\,\sigma$ of the corresponding uncertainty. A fit to $|\eta_{j'}|$ is then performed on each pseudo-experiment. The mean shift of the fit results, with respect to the value obtained in the nominal scenario, is taken as the corresponding uncertainty.

The systematic uncertainties are described in section 5. Table 6.2 summarises the different contributions to the systematic uncertainty on the combined (muon and electron) cross section measurement.

6.1.7 Results

The analysis yields the following cross section measurements for the muon and electron channels:

$$\sigma_{t\text{-ch.}} = 73.3 \pm 10.4 \text{ (stat. + syst. + lum.)} \pm 4.0 \text{ (theor.) pb} \quad \text{(muons)},$$
$$\sigma_{t\text{-ch.}} = 61.6 \pm 13.9 \text{ (stat. + syst. + lum.)} \pm 3.5 \text{ (theor.) pb} \quad \text{(electrons)}.$$

Taking into account uncertainties and the correlations between them, the two measurements are compatible. Combining the muon and electron measurements as described in section 6.1.5 gives:

$$\sigma_{t\text{-ch.}} = 70.0 \pm 6.0 \text{ (stat.)} \pm 6.5 \text{ (syst.)} \pm 3.6 \text{ (theor.)} \pm 1.5 \text{ (lum.) pb}.$$

For comparison, the measured cross section in the NN analysis is:

$$\sigma_{t\text{-ch.}} = 69.7^{+7.2}_{-7.0} \text{ (stat. + syst. + lum.)} \pm 3.6 \text{ (theor.) pb} \quad \text{(muons)},$$
$$\sigma_{t\text{-ch.}} = 65.1^{+9.2}_{-8.9} \text{ (stat. + syst. + lum.)} \pm 3.5 \text{ (theor.) pb} \quad \text{(electrons)},$$

which are again compatible within uncertainties. The combination of the NN muon and electron measurements gives:

$$\sigma_{t\text{-ch.}} = 68.1 \pm 4.1 \text{ (stat.)} \pm 3.4 \text{ (syst.)}^{+3.3}_{-4.3} \text{ (theor.)} \pm 1.5 \text{ (lum.) pb}.$$

Finally, in the BDT analysis, the measured cross section is:

$$\sigma_{t\text{-ch.}} = 66.6^{+7.0}_{-6.6} \text{ (stat. + syst. + lum.)}^{+6.4}_{-3.5} \text{ (theor.) pb} \quad \text{(muons)},$$
$$\sigma_{t\text{-ch.}} = 66.4^{+8.4}_{-7.9} \text{ (stat. + syst. + lum.)}^{+5.4}_{-5.4} \text{ (theor.) pb} \quad \text{(electrons)},$$

and the combined result:

$$\sigma_{t\text{-ch.}} = 66.6 \pm 4.0 \text{ (stat.)} \pm 3.3 \text{ (syst.)}^{+3.9}_{-3.3} \text{ (theor.)} \pm 1.5 \text{ (lum.) pb}.$$

The results of the three analyses are consistent with the SM prediction.

6.1.8 Combination

The results of the three analyses are combined using the BLUE [103] method. The BDT and NN analyses marginalise the experimental systematic uncertainties with the Bayesian method in contrast to the $|\eta_{j'}|$ analysis, which uses pseudoexperiments to quantify the effect. The statistical

correlation between each pair of measurements is estimated by generating dedicated pseudo-experiments. The correlations are 60% between NN and $|\eta_{j'}|$, 69% between BDT and $|\eta_{j'}|$, and 74% between NN and BDT. Correlations for the jet energy scale and resolution, b tagging, and $\not{E}_{\mathrm{T}}$ modelling between $|\eta_{j'}|$ and the two multivariate analyses are expected to be small. This is because the determination of the corresponding nuisance parameters, from the marginalisation adopted in the BDT and NN analyses, is dominated by in-situ constraints from data samples independent of those used to determine uncertainties in the $|\eta_{j'}|$ analysis. The assumed correlation for those uncertainties is taken to be 20%. The correlation has, nevertheless, been varied from 0% to 50%, with a corresponding variation of the central value by -0.03 pb, and no appreciable variation has been observed for the combined uncertainty. For trigger uncertainties, the correlation between $|\eta_{j'}|$ and the two multivariate analyses is more difficult to ascertain. Varying the correlations in the combination from 0% to 100% results in a variation of the central value of 0.03 pb, with no appreciable variation of the combined uncertainty. All other uncertainties are determined mostly from the same data samples used by the two analyses, hence 100% correlation is assumed.

The BLUE method is applied iteratively, as previously carried out in Ref. [99]. In each iteration, the absolute uncertainty is calculated by scaling the relative uncertainties given in table 6.2 with the combined value from the previous iteration. This is repeated until the combined value remains constant. There are no appreciable changes with respect to the non-iterative BLUE method. The 0.03 pb variation in the central value, due to changes in correlation coefficients, is added in quadrature to the total uncertainty. However, this results in a negligible additional contribution.

The χ^2 obtained by the BLUE combination of the three analyses is 0.19, corresponding to a p-value of 0.90, meaning the results of the individual analyses are consistent with each other. The combined result of the measured single top quark t-channel production cross section at $\sqrt{s} = 7$ TeV is:

$$\begin{aligned}\sigma_{t\text{-ch.}} &= 67.2 \pm 6.1 \text{ pb} \\ &= 67.2 \pm 3.7 \text{ (stat.)} \pm 3.0 \text{ (syst.)} \pm 3.5 \text{ (theor.)} \pm 1.5 \text{ (lum.) pb}\end{aligned}$$

for an assumed top quark mass of 172.5 GeV/c^2, which was the mass used in simulations for the analysis.

6.1.9 $|V_{tb}|$ Extraction

Using equation 1.21, which takes into account a possible anomalous Wtb coupling, with the SM prediction calculated assuming $|V_{tb}| = 1$ [101], we get:

$$|V_L V_{tb}| = \sqrt{\frac{\sigma_{t\text{-ch.}}}{\sigma^{th}_{t\text{-ch.}}}} = 1.020 \pm 0.046 \text{ (meas.)} \pm 0.017 \text{ (theor.)}$$

Here the first uncertainty term contains all uncertainties of the cross section measurement including theoretical ones, and the second term is the uncertainty on the SM theoretical prediction. Assuming $|V_{tb}| \leq 1$ and $V_L = 1$, a confidence interval for $|V_{tb}|$, is determined using the unified approach of Feldman-Cousins [104] to be:

$$0.92 < |V_{tb}| \leq 1, \quad \text{at the 95\% confidence level.}$$

6.2 Measurement of Single Top Quark Cross Section at 8 TeV

6.2.1 Introduction

The measurement of single top quark cross section, published in [2], is presented in the following. It is performed on a data sample collected during 2012 at centre-of-mass energy $\sqrt{s} = 8\,\text{TeV}$, corresponding to an integrated luminosity of $19.7\,\text{fb}^{-1}$. We measure the inclusive single top quark production cross section in the t-channel as well as the cross sections of single t and $\bar{\text{t}}$ separately.

The prediction for the theoretical cross section for SM t-channel single top quark production in pp collisions at $\sqrt{s} = 8\,\text{TeV}$ is:

$$\sigma^{\text{theo.}}_{t\text{-ch.}} = 87.2^{+2.8}_{-1.0}\,(\text{scale})^{+2.0}_{-2.2}\,(\text{PDF})\,\text{pb}, \tag{6.4}$$

as obtained in QCD NNLO calculation including resummation of the soft-gluon emission with NNLL calculation [74].

The calculation is performed using the PDF set MSTW08NNLO [61] in the 5FS, with the top quark mass m_{t} set to $173\,\text{GeV}/c^2$, (updated from $172.5\,\text{GeV}/c^2$ used in the previous analysis, which had been closer to the measured value at the time), and the factorisation and renormalisation scales both set to m_{t}.

For single t and $\bar{\text{t}}$ separately, the same calculations predict:

$$\begin{aligned} \sigma^{\text{theo.}}_{t\text{-ch.}}(\text{t}) &= 56.4^{+2.1}_{-0.3}\,(\text{scale}) \pm 1.1\,(\text{PDF})\,\text{pb}, \\ \sigma^{\text{theo.}}_{t\text{-ch.}}(\bar{\text{t}}) &= 30.7 \pm 0.7\,(\text{scale})^{+0.9}_{-1.1}\,(\text{PDF})\,\text{pb}. \end{aligned} \tag{6.5}$$

Complementarily, we can also measure the ratio of t-channel production cross sections at $\sqrt{s} = 8\,\text{TeV}$ and 7 TeV, $R_{8/7}$, the prediction given by [74] is:

$$R^{\text{theo.}}_{8/7} = 1.32^{+0.06}_{-0.02}\,(\text{scale})^{+0.04}_{-0.05}\,(\text{PDF}). \tag{6.6}$$

The analysis strategy closely follows the cross section measurement at 7 TeV using the $|\eta_{\text{j}'}|$ analysis method, which was described in section 6.1. The signal yield is extracted from a ML fit to the distribution of $|\eta_{\text{j}'}|$, with independent fit procedures to extract the t and $\bar{\text{t}}$ production cross sections separately.

6.2.2 Event Selection and Reconstruction

The signal events are defined by the decay of $t \to Wb \to b\ell\nu$, where $\ell = \mu, e$. The $t \to Wb \to b\tau\nu$ decay contributes to the signal when a τ decays leptonically.

The online event selection uses a HLT requiring the presence of either one isolated muon with $p_T > 24\,\text{GeV}/c$ and $|\eta| < 2.1$, or one isolated electron with $p_T > 27\,\text{GeV}/c$ and $|\eta| < 2.5$.

For b tagging, we use the TCHPT algorithm, which has an efficiency of selecting jets coming from b quarks of 46%, and a probability to misidentify as b jets the jets originating from light quarks or gluons of 0.3%, determined from simulation. The choice of the algorithm is due to its good discriminating power against W+c-jet events, which is the main background not containing actual b jets.

The top quark reconstruction, $|\eta_{j'}|$ variable, used $NJMT$ regions, and signal and sideband regions of $m_{b\mu\nu}$ are defined in the same way as described in section 6.1.2. The only addition is the use of the 3J1T selection as a control region.

Table 6.3: Event yield for the main processes in the 2J1T SR and SB, for the muon and electron decay channels. Expected yields are taken from simulation and their uncertainties are due to the finite size of the MC sample with the exception of multijet QCD yield (see section 6.2.3), and W/Z+jets yield (see section 6.2.5), whose yields and uncertainties are taken as the statistical component of the uncertainty in the estimation from data.

Process	Muon		Electron	
	SR	SB	SR	SB
$t\bar{t}$	17214 ± 49	8238 ± 35	11162 ± 38	8036 ± 33
W/Z+jets	10760 ± 104	9442 ± 97	4821 ± 69	6512 ± 81
QCD	765 ± 5	271 ± 4	1050 ± 6	1350 ± 6
Diboson	179 ± 4	161 ± 4	95 ± 3	134 ± 3
tW	1914 ± 28	969 ± 20	1060 ± 28	858 ± 18
s-channel	343 ± 1	118 ± 1	180 ± 1	96 ± 1
t-channel	6792 ± 25	944 ± 9	3616 ± 17	753 ± 8
Total expected	37967 ± 121	20143 ± 106	21984 ± 85	17740 ± 90
Data	38202	20237	22597	17700

Table 6.4: Event yield for the main processes in the 2J1T SR, for events with positively and negatively charged muons and electrons. Expected yields are taken from simulation and their uncertainties are due to the finite size of the MC sample with the exception of multijet QCD yield (see section 6.2.3), and W/Z+jets yield (see section 6.2.5).

Process	Muon		Electron	
	+	−	+	−
$t\bar{t}$	8620 ± 35	8594 ± 35	5574 ± 27	5588 ± 27
W/Z+jets	5581 ± 75	4989 ± 71	2618 ± 52	2121 ± 46
QCD	361 ± 1	366 ± 1	697 ± 2	679 ± 2
Diboson	106 ± 3	73 ± 2	58 ± 2	39 ± 2
tW	964 ± 20	951 ± 20	535 ± 14	525 ± 14
s-channel	225 ± 1	118 ± 1	118 ± 1	62 ± 1
t-channel	4325 ± 19	2467 ± 16	2320 ± 13	1295 ± 11
Total expected	20181 ± 87	17557 ± 83	11920 ± 61	10310 ± 56
Data	20514	17688	12035	10562

The total yields for events in the 2J1T SR and SB regions for muons and electrons are listed in table 6.3, while the separate event yields for positively and negatively charged muons and electrons in the SR are reported in table 6.4.

6.2.3 QCD multijet background

A large proportion of QCD multijet events are successfully rejected applying the selection described in section 3.5.3.

The QCD multijet contribution in our analysis is estimated from data with a ML fit to the distribution of the $m_{\mathrm{T}}(\mathrm{W})$ ($\not{E}_{\mathrm{T}}$) for muons(electrons), performed assuming the parametrisation in equation 6.2. The sum of all other processes (including the signal) $S(x)$ is taken from simulation, while The QCD multijet distribution $B(x)$ is obtained by taking muons and electrons with the same criteria as defined in sections 3.2.3 and 3.2.4, but with reversed isolation requirements for both leptons, selecting muons with $I_{\mathrm{rel}}^{\beta-corr.} > 0.2$ or electrons with $I_{\mathrm{rel}}^{\rho-corr.} > 0.15$.

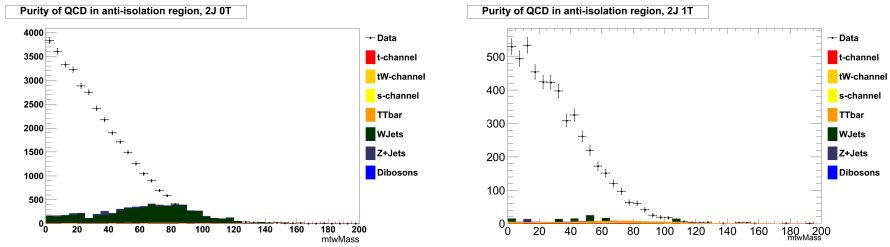

(a) (b)

Figure 6.5: The $m_{\mathrm{T}}(\mathrm{W})$ distributions for data and for non-multijet simulated events in the selection with reversed isolation used to extract the multijet distribution in the muon channel for 2J0T (a) and 2J1T (b).

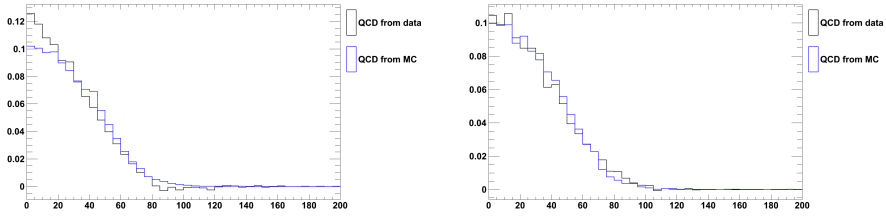

(a) (b)

Figure 6.6: The $m_{\mathrm{T}}(\mathrm{W})$ distributions for QCD multijet distribution extracted from data (black) and from simulation (blue) in the muon channel for 2J0T (a) and 2J1T (b).

These data samples contain a fraction of 98% (muon channel) – 99% (electron channel) events originating from QCD multijet processes in 2J1T. The purity of the samples for the 2J0T and 2J1T regions in the muon channel is illustrated in figure 6.5, showing the residual contribution from other processes as expected from simulation. This contribution is subtracted from data to obtain the QCD multijet contribution. The resulting shapes are compared to the ones from simulation in figure 6.6 in the 2J0T and 2J1T regions in the muon channel, and are similar. Comparison of the shapes obtained for the 2J1T SR and SB is shown in figure 6.7, demonstrating good compatibility with $\frac{\chi^2}{n_{\text{dof}}} \approx 1.3$.

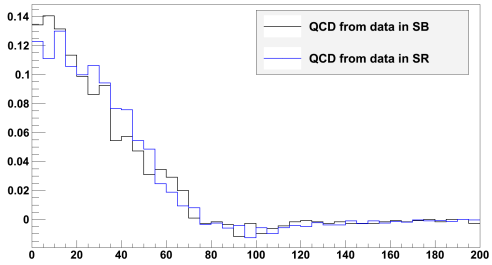

Figure 6.7: The $m_{\text{T}}(\text{W})$ distributions for QCD multijet distribution extracted from data in the muon channel for 2J1T SR (blue) and 2J1T SB (black).

The results of the fits are shown in figure 6.8 for 2J1T. The resulting yield is split according to the ratio of positive and negatively charged leptons in the anti-isolated region.

The fit procedure is repeated using different QCD multijet models, which are obtained by changing the following inputs:

- The isolation range to define the multijet-enriched control region
- The variable fitted on (switching $\not{E}_{\text{T}}$ and $m_{\text{T}}(\text{W})$)
- The range of variable used for fitting (e.g. fitting only on the region not part of analysis after selecting for multijet rejection etc.)
- Using the distribution simulated events instead of the one extracted from data

To conservatively cover the range of values obtained with these different models, we assign a 50% uncertainty on the fitted QCD multijet event yield to be used in the analysis.

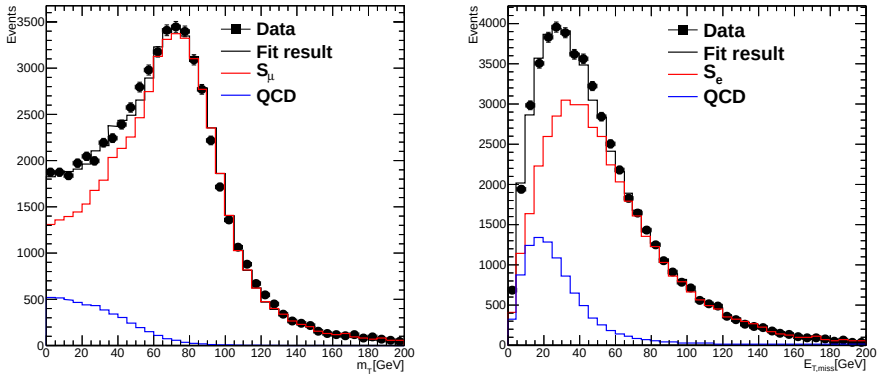

(a) (b)

Figure 6.8: Fit to the $m_{\mathrm{T}}(\mathrm{W})/\not{E}_{\mathrm{T}}$ distribution in the 2J1T regions for (a) muons and (b) electrons. The QCD multijet model is taken from data.

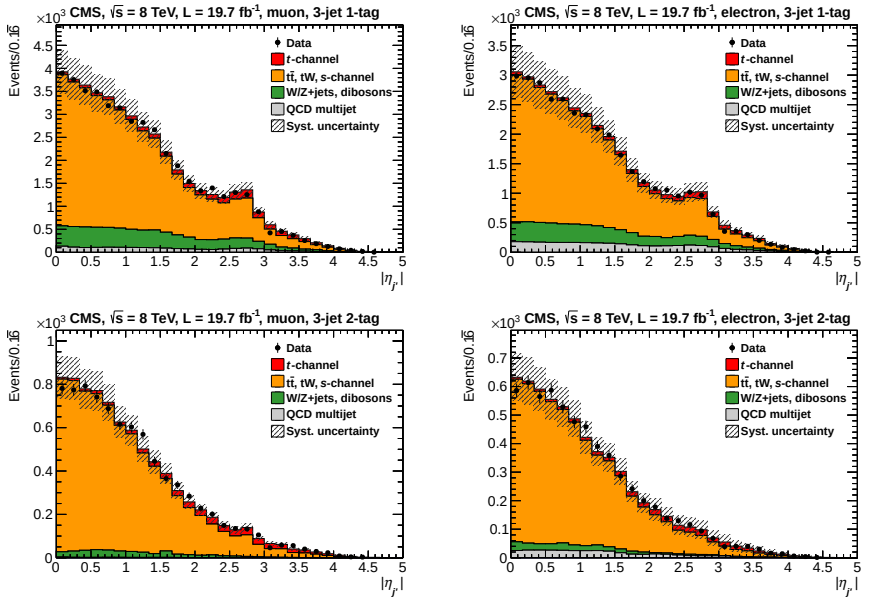

Figure 6.9: Distribution of $|\eta_{j'}|$ in the 3J1T (top) and 3J2T (bottom) regions for muon (left) and electron (right) decay channels. The yield of the simulated processes is normalised to the results of the fit described in section 6.2.6. Systematic uncertainty bands include all uncertainties.

6.2.4 Top quark pair background

The $t\bar{t}$ events tend to contain more b tagged jets than signal events. To study $t\bar{t}$ modelling, we use the 3J1T and 3J2T control regions, which are enriched in $t\bar{t}$ events. The $|\eta_{j'}|$ distribution in these samples is shown in figure 6.9, showing good agreement between data and simulation. The lepton charge in the 3J1T and 3J2T regions is shown in figure 6.10 and the corresponding charge ratio in figure 6.11. The ratio is close to one, as expected for $t\bar{t}$.

To reduce the measurement dependence on the modelling of $t\bar{t}$, we use the $|\eta_{j'}|$ distribution in the 3J2T region to adjust the $|\eta_{j'}|$ distribution used for signal extraction in the 2J1T region. This is done by subtracting from data the contribution of all other SM processes except $t\bar{t}$ in 3J2T. The bin-

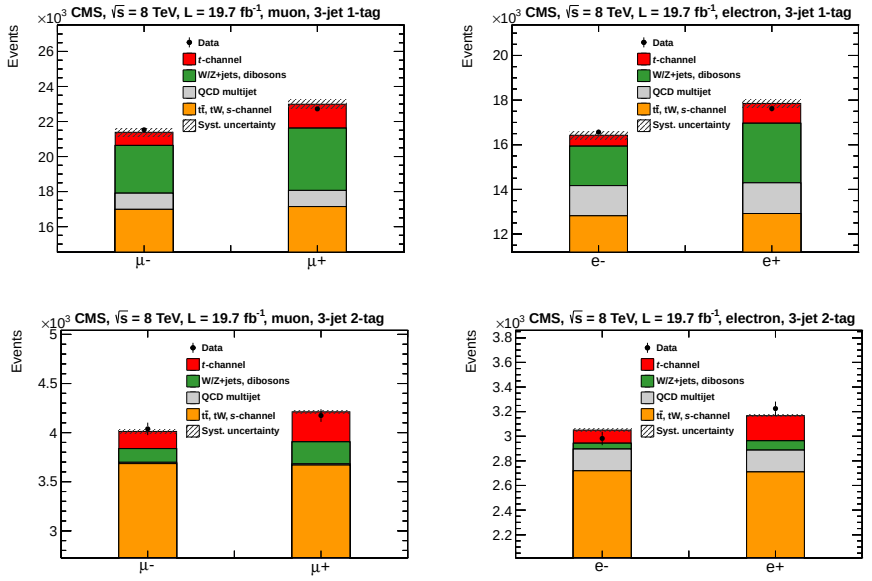

Figure 6.10: Charge of the lepton in the 3J1T (top) and 3J2T (bottom) regions for muon (left) and electron (right) decay channels. The sum of all predictions is normalised to the data yield. Systematic uncertainty bands include all uncertainties on the charge ratio.

by-bin ratio of the resulting distribution and the simulated $t\bar{t}$ distribution is used as an $|\eta_{j'}|$-dependent correction factor for the $t\bar{t}$ distribution in 2J1T. The systematic uncertainties resulting from this procedure are discussed in section 6.2.7.

6.2.5 The W/Z+jets background

The 2J0T control region is used for W/Z+jets background studies. The distribution of $|\eta_{j'}|$ in 2J0T is displayed in figure 6.12, showing good agreement between data and simulation. The lepton charge in 2J0T sample is shown in figure 6.13 and the corresponding charge ratio in figure 6.14.

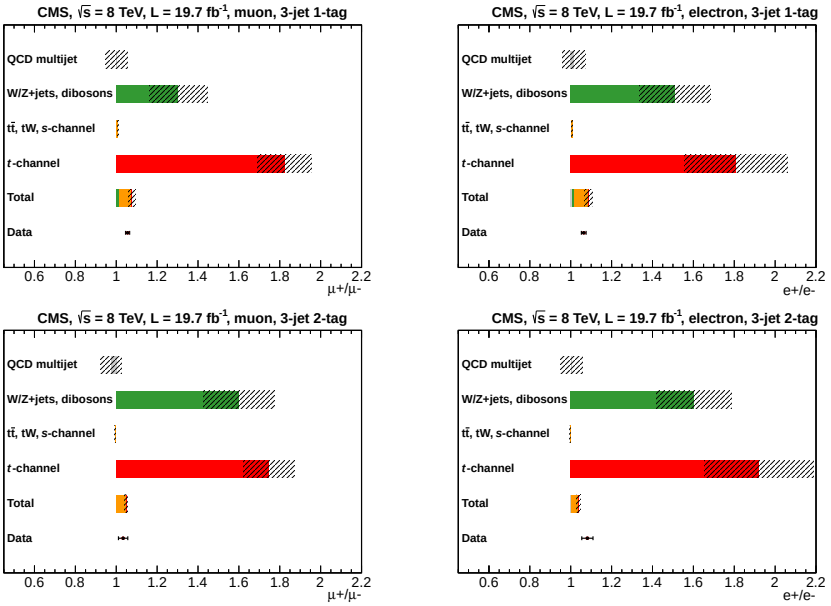

Figure 6.11: Charge ratio between positively and negatively charged leptons in the 3J1T (top) and 3J2T (bottom) regions for muon (left) and electron (right) decay channels. The charge ratio is shown separately for each process, as well as after normalising the sum of all predictions to the data yield. Systematic uncertainty bands include all uncertainties.

The imbalance in the production of positively and negatively charged leptons, which is characteristic to W+jets events, can be seen clearly.

The W+jets extraction from data follows the same principles as the one described in section 6.1.4, with the difference that the $t\bar{t}$ contribution to be subtracted is no longer taken from simulation, but is estimated with the technique described above. This procedure is performed for the inclusive distribution, as well as for positively and negatively charged leptons separately, estimating also the W+jets charge ratio from data in the process. The uncertainty from this procedure is discussed in section 6.2.7.

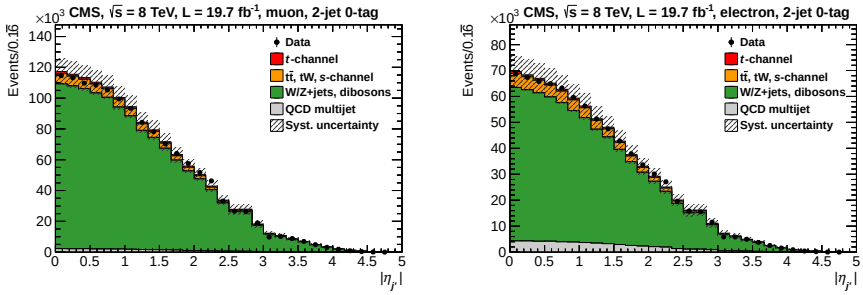

Figure 6.12: Distribution of $|\eta_{j'}|$ in the 2J0T region for muon (left) and electron (right) decay channels. The QCD multijet contribution is derived from the fit to $m_{\mathrm{T}}(\mathrm{W})$ and $\not{E}_{\mathrm{T}}$. Systematic uncertainty bands include pre-fit uncertainties, both on the normalisation and on the shape of the distributions.

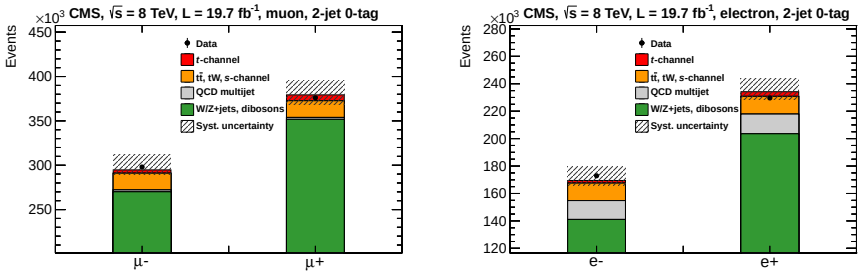

Figure 6.13: Charge of the lepton in the 2J0T region for muon (left) and electron (right) decay channels. The sum of all predictions is normalised to the data yield. Systematic uncertainty bands include all uncertainties on the charge ratio.

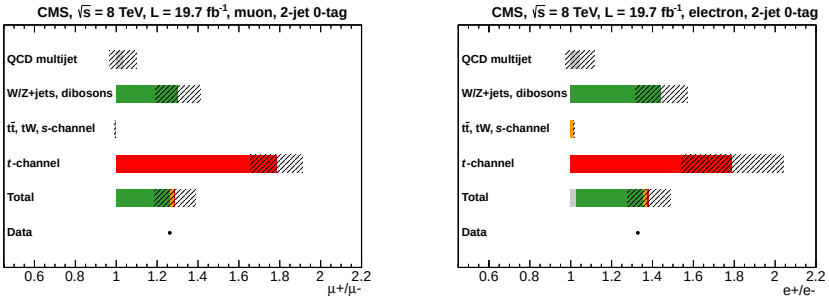

Figure 6.14: Ratio of positively and negatively charged leptons in the 2J0T region for muon (left) and electron (right) decay channels. The charge ratio is shown separately for each process after normalising the sum of all predictions to the data yield. Systematic uncertainty bands include all uncertainties.

6.2.6 Signal Extraction and Cross Section Measurement

Using binned ML fits to the $|\eta_{j'}|$ distributions of the events in the 2J1T SR, we extract the inclusive single top quark cross section, as well as separate cross sections for single t and $\bar{t}$.

The expected number of events in each $|\eta_{j'}|$ bin is modelled with the following likelihood function:

$$n(|\eta_{j'}|) = N_s P_s(|\eta_{j'}|) + N_t P_t(|\eta_{j'}|) + N_{EW} P_{EW}(|\eta_{j'}|) + N_{MJ} P_{MJ}(|\eta_{j'}|), \quad (6.7)$$

where, N_s, N_b, (b=EW, t, MJ) are the yields of the signal and of the three background components, and P_s, P_b are their binned probability distribution functions. We consider the following components:

- **Signal** (indicated with subscript s): P_s is taken from simulation and the total yield N_s is fitted unconstrained.
- **EW background** component (composed of W/Z+jets and dibosons): The P_{EW} distribution is taken as the sum of the contribution of W/Z+jets estimated from the $m_{b\mu\nu}$ sideband with the method described in section 6.2.5, adding the diboson processes from simulation. A gaussian constraint is placed on the yield with a standard deviation of the difference between the data-based yield of W/Z+jets and the expectation from simulation in the sideband region to take

into account the knowledge of the normalisation gained from the sideband.

- **Top quark background** component (subscript t, composed of $t\bar{t}$ and single top quark tW and *s*-channel processes): P_t is taken as the sum of $t\bar{t}$ prediction from the procedure described in section 6.2.4 and the tW and *s*-channel processes normalised to prediction from simulation. This contribution is separated by lepton flavour and charge assuming charge symmetry of $t\bar{t}$ and tW events. The *s*-channel charge ratio is fixed to the SM prediction. The yield is then fitted with a Gaussian constraint of $\pm 10\%$, chosen to cover experimental and theoretical uncertainties on the $t\bar{t}$ cross section.
- **QCD multijet**: P_{MJ} is taken from the QCD multijet enriched sample as described in section 6.2.3, with the yield fixed to the result of the corresponding fit.

The inclusive cross section is extracted from events with positively or negatively charged leptons, using equation 6.7 and defining one likelihood function per lepton flavour, then fitting simultaneously the two distributions for muons and electrons. The single t and $\bar{t}$ cross sections are extracted by further dividing the events by lepton charge, defining one likelihood function per lepton flavour and per charge, then simultaneously fitting the four distributions.

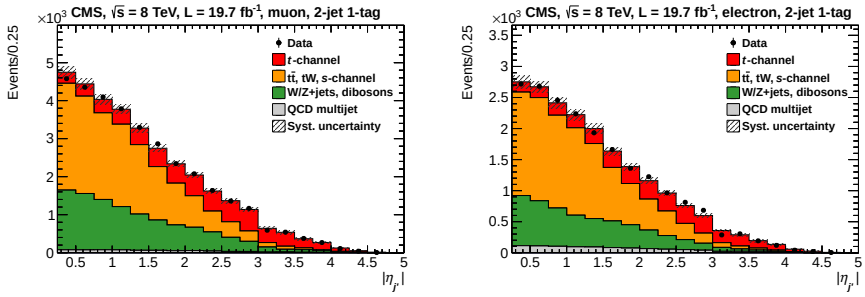

Figure 6.15: Fitted $|\eta_{j'}|$ distributions for muon (left) and electron (right) decay channels, normalised to the yields obtained from the combined total cross section fit. Systematic uncertainty bands include the shape uncertainties on the distributions.

The fit strategy is focused on constraining the major background contributions of W/Z+jets and $t\bar{t}$. In the case of the single t and $\bar{t}$ cross section fit, the event ratio of positively and negatively charged W bosons is also constrained, giving an additional uncertainty. For this reason, the inclusive cross section measurement is more precise. The cross sections are extracted using the detector acceptance derived from the simulated signal sample. The $|\eta_{j'}|$ distributions for the muon and electron decay channels are obtained by normalising the contribution of each process to the fit results, and are shown in figure 6.15 for the inclusive case and in figure 6.16 separated by charge.

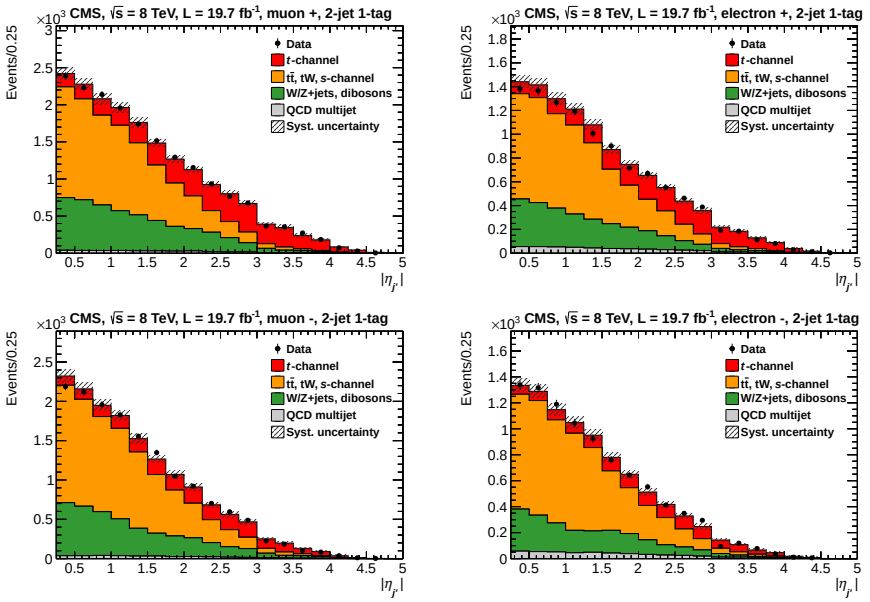

Figure 6.16: Fitted $|\eta_{j'}|$ distributions for muon (left) and electron (right) decay channels, normalised to the yields obtained from the combined single t (above) and $\bar{t}$ (below) cross section ratio fit. Systematic uncertainty bands include the shape uncertainties on the distributions.

The reconstructed top-quark mass $m_{b\mu\nu}$ in the region with $|\eta_{j'}| > 2.5$, after scaling each process contribution to the normalisation obtained from

the fit, is shown in figure 6.17 to illustrate the validity of the fit procedure. The characteristic peak around the top quark mass can be clearly seen in both the muon and the electron channels as the selection is highly enriched in t-channel signal events.

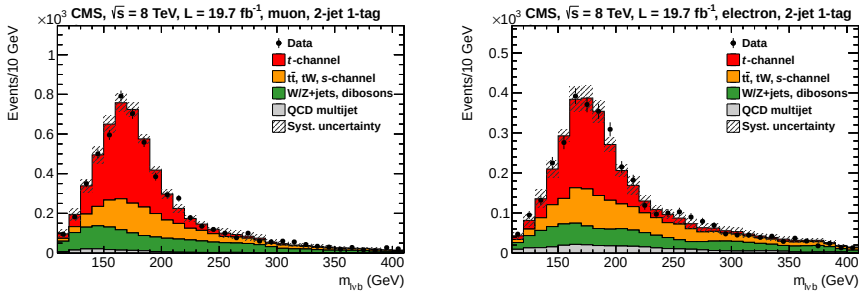

Figure 6.17: Distribution of reconstructed top-quark mass $m_{\mathrm{b}\mu\nu}$ for muon (left) and electron (right) decay channels, in the region with $|\eta_{j'}| > 2.5$, the contribution of each process is scaled to the cross section derived from the fit. Systematic uncertainty bands include the shape uncertainties on the distributions and uncertainties on the normalisation in the $|\eta_{j'}| > 2.5$ region.

6.2.7 Systematic Uncertainties

The treatment of the uncertainties on the background estimation was described in section 6.2.2. Other contributions to the total systematic uncertainty, except the size of the simulated samples, are evaluated by constructing pseudo-experiments for each process, using the distributions and the yields generated considering the altered scenario. Then a fit to the $|\eta_{j'}|$ distribution is performed for each pseudo-experiment,and the mean shift of the fit results with respect to the value obtained for the nominal fit is taken as the corresponding uncertainty. The majority of the systematic uncertainties are described in detail in section 5, while uncertainties specific to this analysis are described below.

The QCD multijet normalisation is varied by $\pm 50\%$ independently for muon and electron decay channels, as discussed in section 6.2.3. The uncertainty related to the W+jets and $t\bar{t}$ estimation is evaluated by generating pseudo-experiments in the SB and in the 3J2T region, respectively. The background estimation is repeated, and then the fit to $|\eta_{j'}|$ is performed and the uncertainty is taken as the RMS of the distribution of fit results. An additional uncertainty for the W+jets contribution is obtained using alternative $|\eta_{j'}|$ shapes from simulation with W+b-jets and the W+c-jets background fractions varied by $\pm 30\%$ independently in the SR and SB regions. An additional uncertainty in the $t\bar{t}$ estimation procedure is determined by performing the signal extraction using the $t\bar{t}$ distribution in the entire $m_{b\mu\nu}$ range, then using two different distributions for SR and SB, with the difference between the two results is taken as the uncertainty. All other systematic uncertainties are coherently propagated through the estimation procedure.

The contribution of each source of uncertainty to the cross section and their ratio measurements is shown in tables 6.5 and 6.6, respectively. Uncertainties affecting the signal efficiency in a similar way for single t and $\bar{t}$, such as b tagging, trigger, reconstruction efficiencies, and luminosity, tend to cancel in the cross section ratio and hence have a smaller effect there. The uncertainties on the background processes, which are independent of the lepton charge, such as $t\bar{t}$ or QCD, have a larger impact on the single $\bar{t}$ cross section, for which the signal-to-background ratio is less favourable, and thus do not cancel out entirely in the ratio measurement. The uncertainties due to the limited size of simulated event samples have a

Table 6.5: Relative impact of systematic uncertainties for the combined muon and electron decay channels.

Uncertainty source	$\sigma_{t\text{-ch.}}$ (%)
Statistical uncertainty	$\pm$ 2.7
JES, JER, MET, and pileup	$\pm$ 4.3
b-tagging and mis-tag	$\pm$ 2.5
Lepton reconstruction/trig.	$\pm$ 0.6
QCD estimation	$\pm$ 2.3
W+jets, $t\bar{t}$ estimation	$\pm$ 2.2
Other backgrounds ratio	$\pm$ 0.3
Signal modeling	$\pm$ 5.7
PDF uncertainty	$\pm$ 1.9
Simulation sample size	$\pm$ 0.7
Luminosity	$\pm$ 2.6
Total systematic	$\pm$ 8.9
Total uncertainty	$\pm$ 9.3

larger impact on the ratio than on the total cross section. The PDF uncertainties for single t and $\bar{t}$ production are largely anticorrelated, enhancing corresponding contribution in the charge ratio measurement.

Because of these differences, the results of the inclusive and exclusive (t and $\bar{t}$) cross section fits are not numerically identical, giving different values for the total cross section. Nevertheless, keeping two separate procedures is motivated by the fact that the inclusive fit has a better overall performance regarding the systematic uncertainties in the inclusive cross section measurement.

6.2.8 Results

Cross section measurements

The measured inclusive single top quark production cross section in the t-channel is

$$\sigma_{t\text{-ch.}} = 83.6 \pm 2.3\,(\text{stat.}) \pm 7.4\,(\text{syst.})\,\text{pb}. \tag{6.8}$$

Table 6.6: Relative impact of systematic uncertainties on the exclusive single t and $\bar{t}$ production cross sections and the ratio measurements.

Uncertainty source	$\sigma_{t\text{-ch.}}(t)$ (%)	$\sigma_{t\text{-ch.}}(\bar{t})$ (%)	$R_{t\text{-ch.}}$ (%)
Statistical uncertainty	$\pm$ 2.7	$\pm$ 4.9	$\pm$ 5.1
JES, JER, MET, and pileup	$\pm$ 4.2	$\pm$ 5.2	$\pm$ 1.1
b-tagging and mis-tag	$\pm$ 2.6	$\pm$ 2.6	$\pm$ 0.2
Lepton reconstruction/trig.	$\pm$ 0.5	$\pm$ 0.5	$\pm$0.3
QCD estimation	$\pm$ 1.6	$\pm$ 3.5	$\pm$1.9
W+jets, $t\bar{t}$ estimation	$\pm$ 1.7	$\pm$ 3.6	$\pm$ 3.0
Other backgrounds ratio	$\pm$ 0.1	$\pm$ 0.2	$\pm$ 0.6
Signal modeling	$\pm$ 4.9	$\pm$ 9.4	$\pm$ 6.1
PDF uncertainty	$\pm$ 2.5	$\pm$ 4.8	$\pm$ 6.2
Simulation sample size	$\pm$ 0.6	$\pm$ 1.1	$\pm$ 1.2
Luminosity	$\pm$ 2.6	$\pm$ 2.6	—
Total systematic	$\pm$ 8.2	$\pm$ 13.4	$\pm$ 9.6
Total uncertainty	$\pm$ 8.7	$\pm$ 14.2	$\pm$ 10.9
Measured cross section or ratio	53.8 ± 4.7 pb	27.6 ± 3.9 pb	1.95 ± 0.21

The measured single t and $\bar{t}$ production cross sections in the *t*-channel are

$$\begin{aligned} \sigma_{t\text{-ch.}}(t) &= 53.8 \pm 1.5\,(\text{stat.}) \pm 4.4\,(\text{syst.})\,\text{pb}, \\ \sigma_{t\text{-ch.}}(\bar{t}) &= 27.6 \pm 1.3\,(\text{stat.}) \pm 3.7\,(\text{syst.})\,\text{pb}. \end{aligned} \tag{6.9}$$

Cross section ratios

The ratio of *t*-channel production cross sections at $\sqrt{s} = 8$ and 7 TeV, $R_{8/7}$, is derived with respect to the result reported in ref. [1], which combines three measurements, as described in section 6.1. The correlations between the sources of uncertainties reported in sections 6.1.6 and 6.2.7 are determined as follows: the uncertainties related to signal extraction and background estimation from data are treated as fully uncorrelated, while for the rest of the uncertainties the 8 TeV analysis is considered fully correlated to its 7 TeV $|\eta_{j'}|$ counterpart, and the same choices for correlations as in [1] are adopted between the 8 TeV $|\eta_{j'}|$ analysis and the two 7 TeV

multivariate analyses. The ratio measured in such a way is:

$$R_{8/7} = \sigma_{t\text{-ch.}}(8\,\text{TeV})/\sigma_{t\text{-ch.}}(7\,\text{TeV}) = 1.24 \pm 0.08\,(\text{stat.}) \pm 0.12\ (\text{syst.}). \tag{6.10}$$

The measured ratio of single t to $\bar{\text{t}}$ production cross sections at $\sqrt{s} = 8\,\text{TeV}$ is:

$$R_{t\text{-ch.}} = \sigma_{t\text{-ch.}}(\text{t})/\sigma_{t\text{-ch.}}(\bar{\text{t}}) = 1.95 \pm 0.10\,(\text{stat.}) \pm 0.19\,(\text{syst.}), \tag{6.11}$$

and in figure 6.18 it is compared to the predictions obtained with several PDF sets: MSTW2008NLO [61], HERAPDF1.5 NLO [105], ABM11 [106], CT10, CT10w [60], and NNPDF [62]. The fixed 4FS scheme PDFs are used For MSTW2008NLO, NNPDF, ABM, and CT10w together with the POWHEG 4FS calculation, while the POWHEG calculation in the 5FS is used for the other PDFs, which are derived from a variable flavour scheme. The nominal value for the top-quark mass used is $173.0\,\text{GeV}/c^2$. Error bars for the CMS measurement include the statistical (light yellow) and systematic (dark green) components.

Error bars for the different PDF sets include the statistical uncertainty, the uncertainty in the factorisation and renormalisation scales, derived varying both of them by factors of 1/2 and 2, and the uncertainty in the top-quark mass, derived varying the top-quark mass between 172.0 and $174.0\,\text{GeV}/c^2$. It can be seen that the predictions for this observable obtained with different PDF sets are not always compatible with within the respective uncertainties, showing the potential of this measurement to discriminate between the different sets, should a better precision be achieved.

6.2.9 Extraction of $|V_{\text{tb}}|$

Using equation 1.21 and inserting the measured cross section from equation 6.8 and the theoretical cross section from equation 6.4 and using the assumptions discussed in section 1.3 results in:

$$|f_{\text{Lv}} V_{\text{tb}}| = 0.979 \pm 0.045\,(\text{exp.}) \pm 0.016\,(\text{theo.}). \tag{6.12}$$

The experimental uncertainty comes from the uncertainties on the measurement of $\sigma_{t\text{-ch.}}$, while the theoretical uncertainty is due to the uncertainties on $\sigma^{\text{theo.}}_{t\text{-ch.}}$.

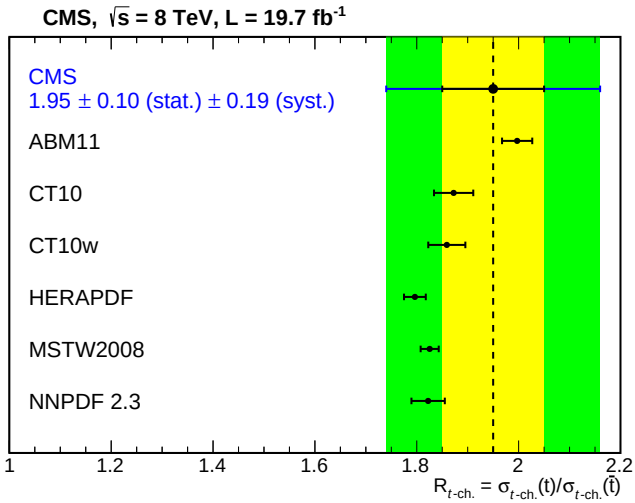

Figure 6.18: Comparison of the measured $R_{t\text{-ch.}}$ with the predictions obtained using different PDF sets.

Combining the measurement with the one performed in section 6.1.9 using BLUE, considering the full correlation matrix amongst the four measurements and the correlations described for the $R_{8/7}$ measurement, we obtain the following result:

$$|f_{\text{Lv}} V_{\text{tb}}| = 0.998 \pm 0.038\,(\text{exp.}) \pm 0.016\,(\text{theo.}) \qquad \text{(7+8 TeV combination)}. \tag{6.13}$$

Using the Feldman–Cousins unified approach [104], the confidence interval for $|V_{\text{tb}}|$, assuming the constraints $|V_{\text{tb}}| \leq 1$ and $f_{\text{Lv}} = 1$ is determined from the result in equation 6.13, giving:

$$|V_{\text{tb}}| > 0.92 \text{ at the 95\% confidence level.} \tag{6.14}$$

The combined limit does not improve compared to the 7 TeV measurement because the observed value is lower at 8 TeV.

7 Measurement of Single Top Quark Polarisation

7.1 Introduction

The measurement of top quark polarisation in single top production [3] is based on proton-proton collisions recorded by the CMS detector at a centre-of-mass energy 8 TeV in 2012 at the LHC, corresponding to an integrated luminosity of 19.7 ± 0.5 fb^{-1}. The muon is used as the spin analyser through the decay $t \to bW \to b\mu\nu$ for its high spin analysing power as described in section 1.4, and also because the muon identification efficiency is very high in the CMS detector. To be sensitive to potential CP-violation effects predicted by some BSM models, the measurement is also done separately for top quark and antiquark events.

The analysis strategy is to select events in such a way obtain a set of relatively high purity t-channel single top quark events, from these estimate the signal and background composition of data using a ML fit, and apply an unfolding technique to obtain the differential cross section of an angular distribution sensitive to polarisation at parton level, as described by eq. 1.23. Finally, the top quark spin asymmetry and the corresponding polarisation are calculated for top quark and antiquark events and their combination from the unfolded distribution according to eq. 1.22.

7.2 Event Selection

The HLT election for muons is the same as in section 6.2.2, containing at least one isolated muon with $p_T > 24\,\text{GeV}/c$ and $|\eta| < 2.1$. We use the CSV algorithm for b-tagging with a tight selection, corresponding to an

efficiency of ≈50% for jets originating from true b quarks in simulated signal events and a mistagging rate of ≈0.1% for other jets.

Statistically independent control samples are used for a number of purposes in this measurement. Samples with inverted isolation requirement on the muon are used to extract templates for estimating the contamination by QCD multijet events, the size of which is determined using a BDT classifier, as described in section 7.3. Samples with different jet and b-tagged jet multiplicities are used to validate the simulation of W+jets (2J0T), discussed in section 7.4, and $t\bar{t}$ (3J1T and 3J2T) events, discussed in section 7.6. The 3J2T control region is also used provide additional constraints on the determination of background and signal strengths relative to the SM.

7.3 Estimation and Rejection of Multijet Events Background

7.3.1 Anti-multijet BDT

To achieve maximal separation between the signal and QCD multijet background, and to reduce impact of the large uncertainties related to this specific background on the analysis, a multivariate technique is applied. The events for training the MVA are taken the 2J1T region. The training is performed only on signal and multijet events. We use independently generated samples for training and testing. For multijet events, we use data extracted from the selection with reversed isolation as described in section 6.2.3, with events split randomly between training and testing samples. The signal events used for training are also used for training the signal vs. background BDT, but not anywhere else, while the data events used for training are also used for fitting further in the analysis. Selecting multijet training events from the 2J0T region was considered, but the BDT distribution in 2J0T did not agree with 2J1T distribution.

Variables

The list of variables that were considered as for discriminating between signal and multijet events (the set will be reduced by selecting the best variables):

- $m_{\mathrm{T}}(\mathrm{W})$ – transverse mass of the W-boson candidate
- $\not{E}_{\mathrm{T}}$ – missing transverse energy
- $m_{\mathrm{b}\mu\nu}$ – the invariant mass of the top quark candidate
- $|\eta_{\mathrm{t}}|$ – the absolute pseudorapidity of the top quark candidate
- $C - 3 \cdot (q_1 * q_2 + q_1 * q_3 + q_2 * q_3)$, where $0 <= q_1 <= q_2 <= q_3$ are the eigenvalues of the momentum tensor $\sum p_j[a] * p_j[b] / \sum p_j^2$ normalised to 1. Return value is between 0 and 1 and measures the 3-jet structure of the event (C vanishes for a "perfect" 2-jet event).
- $D - 27 \cdot (q_1 * q_2 * q_3)$, where $q_i$are defined as above. The value is between 0 and 1 and measures the 4-jet structure of the event (D vanishes for a planar event).
- $isotropy - (\mathcal{S}_{\max} - \mathcal{S}_{\min})/\mathcal{S}_{\max}$ with $\mathcal{S} \equiv \sum_{i}^{\mu,\text{jets}} |\vec{n} \cdot \vec{p}_i|$, where the unit vector in the transverse r–ϕ plane, $\vec{n} = (\cos\phi, \sin\phi)$, can be chosen to either maximise or minimise $\mathcal{S}$.
- $thrust - max_{|\vec{n}|=1} \frac{\sum \vec{n} \cdot \vec{p}_i}{\sum |\vec{p}_i|}$. The allowed range is $1/2 \leq thrust \leq 1$, with a 2-jet event corresponding to $thrust \approx 1$ and an isotropic event to $thrust \approx 1/2$.
- $aplanarity - 1.5 \cdot q_1$, where q_1 us defined as above. Return values are 0.5 for spherical and 0 for planar and linear events.
- m_{bj} – mass of the b-tagged jet
- m_{lj} – mass of the untagged jet
- p_T^{bj} – the transverse momentum of the b-tagged jet
- p_T^{lj} – the transverse momentum of the untagged jet

Muon p_{T} is another variable that seemed to discriminate very well between signal and multijet events, but it was found to be highly correlated with muon isolation, so it was unusable as the multijet-enriched sideband is defined by inverting the relative isolation criterion. The normalised distributions of the potential discriminating variables for background and signal are shown in figure 7.1, and the correlations between them are shown in figure 7.2.

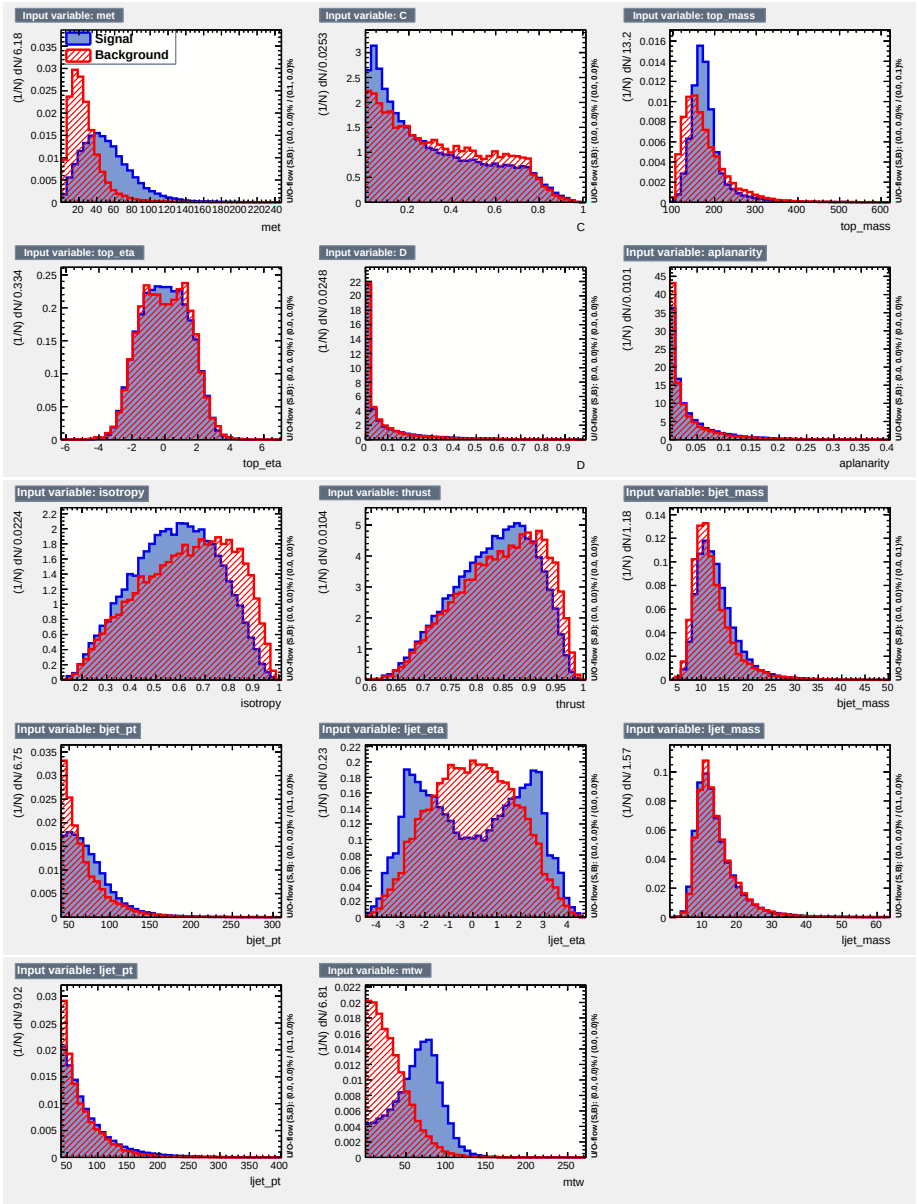

Figure 7.1: BDT input variable candidates. Blue are t-channel events and red QCD multijet events.

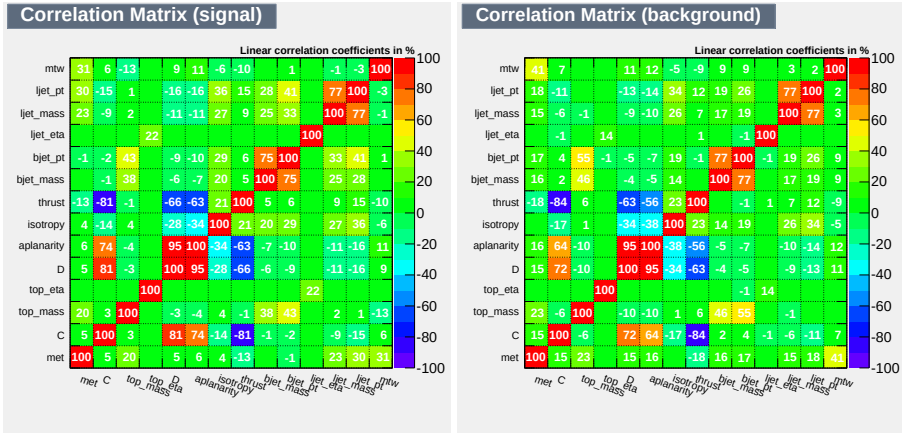

Figure 7.2: BDT candidate variable correlations for signal (left) and background (right).

The BDT is trained with the TMVA package[107]. Our configuration utilises 50 decision trees with boosting done using the Gradient boost method. Even though the gradient boosting algorithm is already relatively resilient to overtraining, we reduce it further by setting the shrinkage variable to 0.1. We do not use bagging in our training. The precise settings used for the MVA training are listed below:

- NTrees=50
- BoostType=Grad
- Shrinkage=0.1
- !UseBaggedGrad
- SeparationType=CrossEntropy
- nCuts=200
- nEventsMin=250
- PruneStrength=7
- PruneMethod=CostComplexity
- MaxDepth=2

Variable ranking

To check which variables are most useful in discriminating signal and multijet, we obtained a variable ranking using the Forward Stepwise Selection and Backward Stepwise Selection methods, which were discussed in section 4.1.3- For both, we started by fixing the signal efficiency and measured the multijet rejection achieved by including different variables. The signal efficiency in the muon channel was fixed at 70%. The step-by-step results using FSS are:

1. Only $m_{\mathrm{T}}(\mathrm{W})$ - 82.6% multijet rejection
2. After adding $\not{E}_{\mathrm{T}}$ - 87.5%
3. After adding Isotropy - 88.7%
4. After adding $m_{\mathrm{b}\mu\nu}$ - 89.3%
5. After adding $p_{\mathrm{T}}^{\mathrm{j}'}$ - 90.2%
6. After adding $m_{\mathrm{j}'}$ - 90.6%
7. After adding m_{b} - 90.7%

No further improvement was gained from adding other variables. The same thing using BSS gave the following results: The rejection did not decrease from baseline by removing C, D, aplanarity, thrust, m_{b}, $p_{\mathrm{T}}^{\mathrm{b}}$ or $m_{\mathrm{j}'}$.

1. After removing $m_{\mathrm{T}}(\mathrm{W})$ - 79.6%
2. After removing $\not{E}_{\mathrm{T}}$ - 67.2%
3. After removing $m_{\mathrm{b}\mu\nu}$ - 55.5%
4. After removing Isotropy - 34.6%
5. After removing $p_{\mathrm{T}}^{\mathrm{j}'}$ - 32.7%
6. After removing $|\eta_{\mathrm{t}}|$ - no variables left

Clearly, $m_{\mathrm{T}}(\mathrm{W})$, which has been used as the discriminating variable in previous analyses, provides the largest discrimination power, but additional power is provided by other variables. Based on these results, we restrict the number of variables to be used in the training to the 5 that were found to have an effect in both FSS and BSS procedures:

1. $m_{\mathrm{T}}(\mathrm{W})$
2. $\not{E}_{\mathrm{T}}$
3. isotropy
4. $m_{\mathrm{b}\mu\nu}$
5. $p_{\mathrm{T}}^{\mathrm{j}'}$

The ROC curves for adding these variables one by one are shown of Fig 7.3.

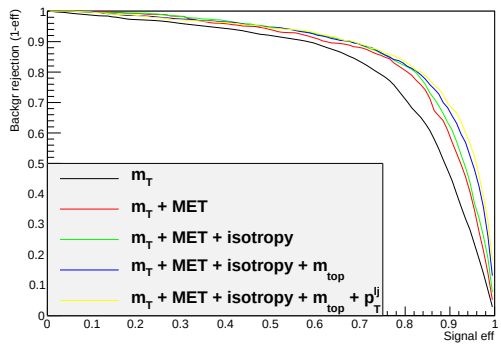

Figure 7.3: $\mathrm{BDT}_{\mathrm{multijet}}$ response ROC with variables added one by one.

Results

The output of $\mathrm{BDT}_{\mathrm{multijet}}$ can be seen on figure 7.4. The working point for the $\mathrm{BDT}_{\mathrm{multijet}}$ selection has been chosen such that it gives approximately the same signal efficiency as the cut-based multijet rejection with $m_{\mathrm{T}}(\mathrm{W})$.

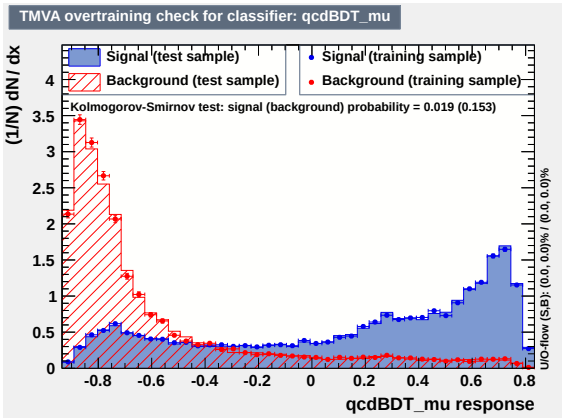

Figure 7.4: $\mathrm{BDT}_{\mathrm{multijet}}$ response with training and testing events shown.

The final working point for the $\mathrm{BDT}_{\mathrm{multijet}}$ discriminator is -0.15. The efficiency of the $\mathrm{BDT}_{\mathrm{multijet}}$ compared to $m_{\mathrm{T}}(\mathrm{W})$ is demonstrated in figure 7.5 and can be seen to be approximately twice as effective as using the $m_{\mathrm{T}}(\mathrm{W})$ variable alone for rejecting multijet events.

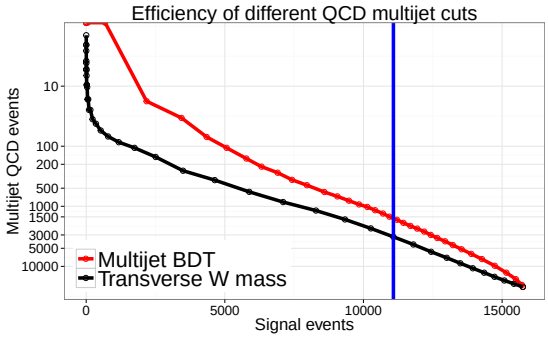

Figure 7.5: $\mathrm{BDT}_{\mathrm{multijet}}$ response ROC (red) compared to $m_{\mathrm{T}}(\mathrm{W})$ (black). Cut point shown with blue line.

7.3.2 QCD Multijet Estimation

The event yields of multijet QCD events in the signal region and control regions are measured performing a ML fit to the distributions of the $\mathrm{BDT}_{\mathrm{multijet}}$ distribution, again assuming the parametrisation in equation 6.2, with x now representing the value for the $\mathrm{BDT}_{\mathrm{multijet}}$ classifier. The fit is performed on region of the $\mathrm{BDT}_{\mathrm{multijet}}$ not used in further analysis (i.e. $\mathrm{BDT}_{\mathrm{multijet}} < -0.15$), and extrapolated to the whole region. The QCD multijet contribution is considered unconstrained in the fit, while a log-normal constraint of $\pm 20\%$ is taken for $S(x)$. The $\mathrm{BDT}_{\mathrm{multijet}}$ shapes for the different physical processes are shown in figure 7.6. It can be seen that the QCD multijet distribution shape is clearly distinct and the rest of the processes have fairly similar shapes. The only exception is DY+jets, but its contribution in yield is negligible, so it is added to the signal-like $S(x)$ component. The effect of this choice is examined in section 7.3.3.

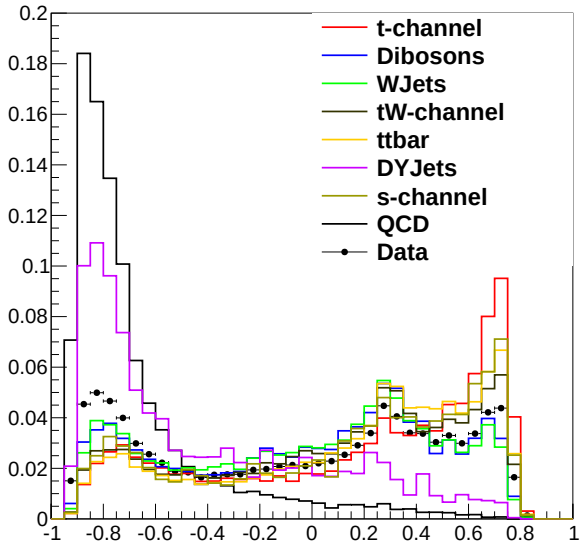

Figure 7.6: The $\mathrm{BDT}_{\mathrm{multijet}}$ distribution of data, QCD template and signal-like processes in 2J1T.

The contamination of non-QCD processes in the anti-isolated data sample is estimated by the MC-simulation and is subtracted from the QCD template. The purity in 2J1T is 93% for the full $BDT_{multijet}$ range and 98% in the fit range. In the control regions, all the purities are over 80%, except for the 3J2T sample for muons, where it is 64%. Illustration is shown in figure 7.7. We can see that the contamination is concentrated in the region of high values of $BDT_{multijet}$. The effect of this on the MC subtraction is examined in section 7.3.3.

Table 7.1: Multijet fit results

Region	Scale factor	Event yields with $BDT_{multijet} > -0.15$	$\frac{\chi^2}{NDF}$
2J1T	Multijet: 0.65 ± 0.02 Signal-like: 1.17 ± 0.02	1606.7 ± 31.4 90027.8 ± 811.2	11.0
2J0T	Multijet: 0.91 ± 0.02 Signal-like: 1.04 ± 0.01	13830.3 ± 168.1 1130387.0 ± 3571.7	67.1
3J1T	Multijet: 0.58 ± 0.04 Signal-like: 1.08 ± 0.02	488.4 ± 28.3 69980.3 ± 726.6	5.0
3J2T	Multijet: 1.34 ± 0.42 Signal-like: 1.09 ± 0.03	89.6 ± 27.8 17502.4 ± 381.6	1.8

The fit results are illustrated in figure 7.8 are shown in table 7.1. The uncertainty show in the table is composed of fit uncertainty and the uncertainty due to limited size of the MC samples. Some discrepancy can be observed in the $BDT_{multijet}$ variable region containing no multijet contribution. However, this can be attributed to different normalisation of signal-like components, which will be fitted later in the analysis.

7.3.3 Cross-checks

The stability of the result is tested by performing alternative fits with different settings. The amount of multijet events in the 3J1T and 3J2T regions is negligible, so the results for the cross-check will not be shown, although the same checks were performed and the conclusions also apply to those regions.

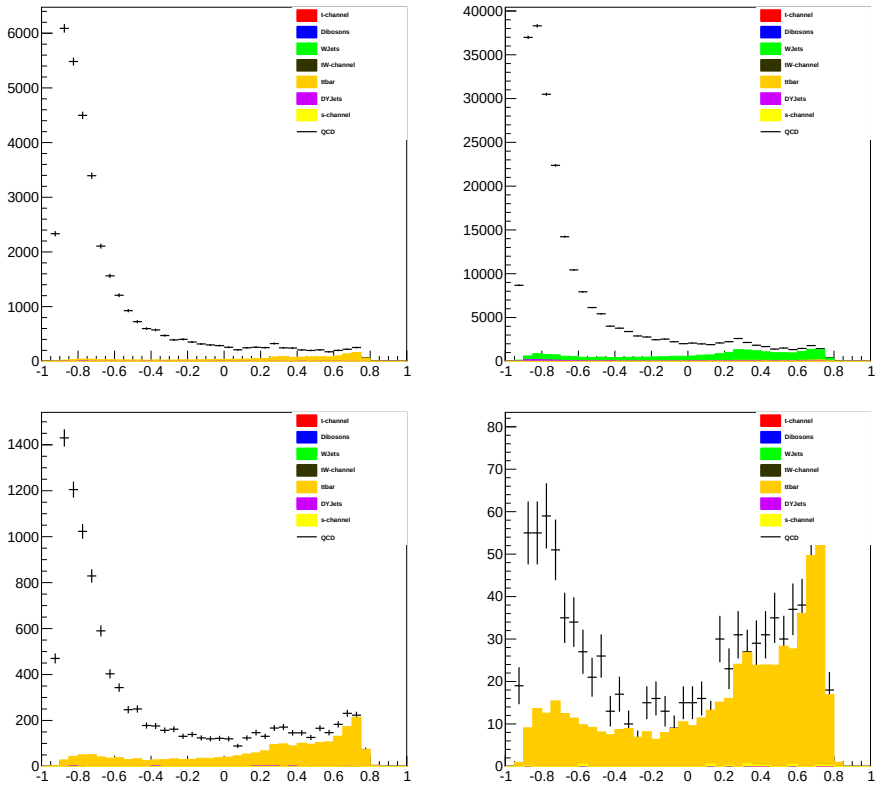

Figure 7.7: The $\mathrm{BDT}_{\mathrm{multijet}}$ distribution of the QCD multijet template in the 2J1T sample (top-left), the 2J0T sample (top-right), the 3J1T sample (bottom-left) and the 3J2T sample (bottom-right). The distribution of simulated multijet events is not shown due to the very high event weights. Orange is contamination from $\mathrm{t\bar{t}}$ events and green is contamination from W+jets events as predicted by simulation.

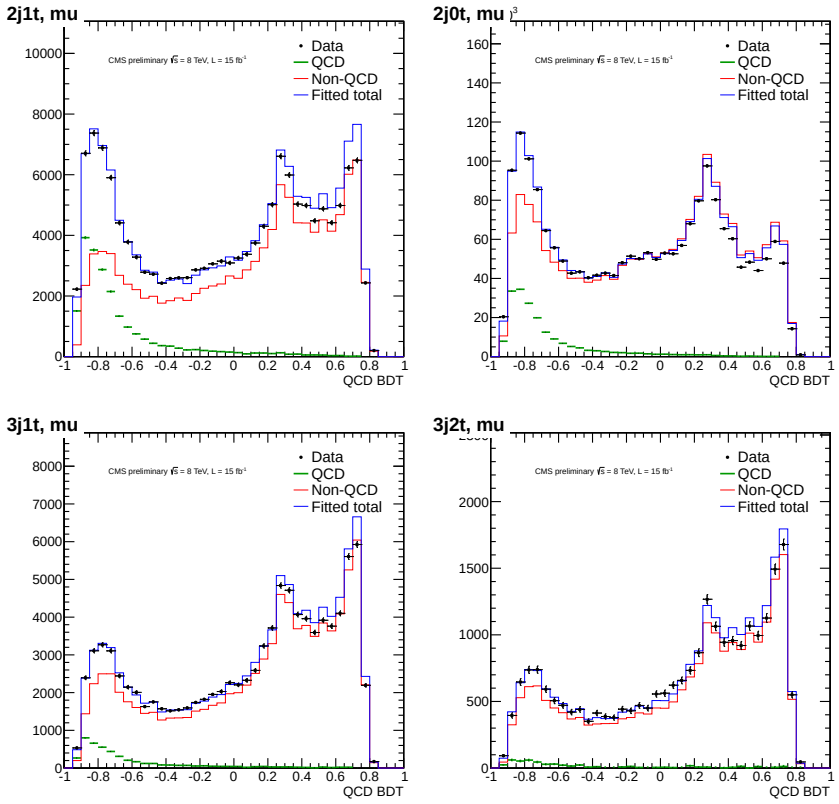

Figure 7.8: The $BDT_{multijet}$ distribution scaled to the the fit results in 2J1T (top-left), 2J0T (top-right), 3J1T (bottom-left) and 3J2T (bottom-right).

Table 7.2: QCD multijet fit results with changed boundaries of the region with reversed isolation cut.

Region	Anti-iso	Scale factors	Event yields $\mathrm{BDT}_{\mathrm{multijet}} > -0.15$	$\frac{\chi^2}{NDF}$
2J1T	Up	Multijet: 1.27 ± 0.03 Signal-like: 1.16 ± 0.02	1764.5 ± 40 88854 ± 1007	10.1
2J1T	Down	Multijet: 1.32 ± 0.03 Signal-like: 1.19 ± 0.02	1760.8 ± 41 91374 ± 985	11.9
2J0T	Up	Multijet: 1.74 ± 0.02 Signal-like: 1.04 ± 0.01	17075 ± 132 1126775 ± 2062	67.0
2J0T	Down	Multijet: 1.90 ± 0.02 Signal-like: 1.04 ± 0.01	20136 ± 166 1128381 ± 2940	68.2

Variation of anti-isolated region boundaries

To check the effect of our choice of isolation range, we perform the fit with multijet templates extracted from different regions, splitting the region with reversed isolation cut roughly in half by number of events: "anti-iso down": ($0.2 < I_{\mathrm{rel}}^{\beta-corr.} < 0.3$) and "anti-iso up": ($0.3 < I_{\mathrm{rel}}^{\beta-corr.} < 0.5$). The results are shown in table 7.2.

Using full range of $\mathrm{BDT}_{\mathrm{multijet}}$ variable for fitting

To check the stability of the fit in relation to selecting a sub-range of the $\mathrm{BDT}_{\mathrm{multijet}}$ variable for fitting, we perform the fit on the full range of the $\mathrm{BDT}_{\mathrm{multijet}}$ variable. The results are presented in table 7.3 and agree well with the nominal result, so we can generalise the fit result in a sub-region to the whole $\mathrm{BDT}_{\mathrm{multijet}}$ region.

Comparing the $\mathrm{BDT}_{\mathrm{multijet}}$ fit to the $m_{\mathrm{T}}(\mathrm{W})$ fit

The fit result is also compared to the fit using the shape of $m_{\mathrm{T}}(\mathrm{W})$ distribution, which was used in the cross section analyses. The results using $m_{\mathrm{T}}(\mathrm{W})$ are shown in figure 7.9 and listed in table 7.4. Again, the agreement is reasonable.

Table 7.3: QCD multijet fit results, fitted on full $\mathrm{BDT}_{\mathrm{multijet}}$ region

Region	Scale factors	Event yields $\mathrm{BDT}_{\mathrm{multijet}} > -0.15$	$\frac{\chi^2}{NDF}$
2J1T	Multijet: 0.71 ± 0.01 Signal-like: 1.10 ± 0.01	1767 ± 26 84308 ± 338	8.6
2J0T	Multijet: 1.06 ± 0.01 Signal-like: 0.99 ± 0.01	16189 ± 111 1070901 ± 665	51.0

Table 7.4: Multijet fit results with the $m_{\mathrm{T}}(\mathrm{W})$ variable. NB! Event yields with $m_{\mathrm{T}}(\mathrm{W}) > 50$ are not directly comparable to the nominal fit, as the selection is performed on a different variable

Region	Scale factors	Event yields $m_{\mathrm{T}}(\mathrm{W}) > 50$	$\frac{\chi^2}{NDF}$
2J1T	Multijet: 0.69 ± 0.03 Signal-like: 1.07 ± 0.02	3301 ± 128 82423 ± 1653	5.2
2J0T	Multijet: 0.76 ± 0.02 Signal-like: 1.02 ± 0.01	22240 ± 511 1230263 ± 6408	17.0

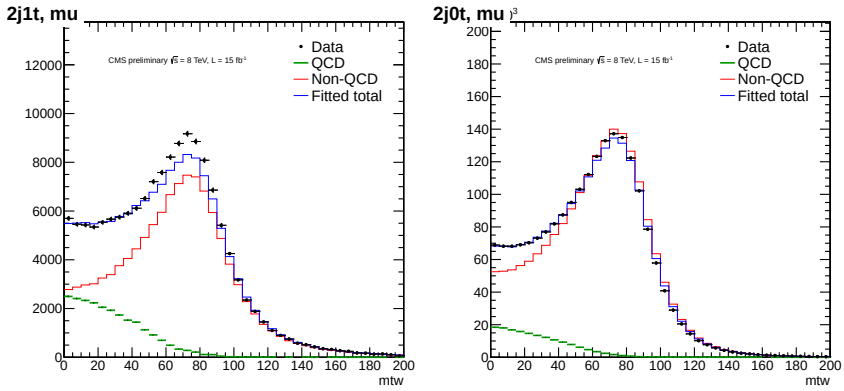

Figure 7.9: The fitted $m_{\mathrm{T}}(\mathrm{W})$ distribution in 2J1T (left) and 2J0T (right)

Table 7.5: 4-component multijet fit results

Region	Scale factors	Event yields $BDT_{multijet} > -0.15$	$\frac{\chi^2}{NDF}$
2J1T	Multijet: 0.65 ± 0.02	1611 ± 40	1.6
	Top: 0.89 ± 0.08	51140 ± 4690	
	EW: 1.79 ± 0.17	32481 ± 3078	
	DY: 0.90 ± 0.16	1049 ± 184	
2J0T	Multijet: 1.06 ± 0.02	16122 ± 291	82.8
	Top: 0.82 ± 0.15	56059 ± 10219	
	EW: 1.10 ± 0.01	1070394 ± 8658	
	DY: 0.48 ± 0.06	21084 ± 2685	

Fit with more components

As seen in figure 7.6, the shapes of the signal-like components differ to some degree. To estimate the effect of this, the multijet estimation was performed by fitting 4 components instead of 2. The components were Multijet, DY, Electroweak V production and top processes. The results are shown in table 7.5 and they are similar to the 2-component fit. Although the χ^2 value goes down a lot in 2J1T, the resulting multijet event yield is almost identical. We can conclude that changing the number of components does not significantly affect the multijet estimation and proceed by using the 2-component fit.

Effects of MC subtraction

As can be seen from figure 7.7, the purity of the multijet template drops sharply at high $BDT_{multijet}$ values. As the final shape is obtained by subtracting simulated signal-like process templates from the anti-isolated data template, the resulting shape might be vulnerable to fluctuations in the templates. To check, we changed the MC templates to be subtracted by changing their normalisation. All the templates were changed together, by 30% for W+jets and by 10% for all the other processes. The fit results are shown in table 7.6. The fit results are consistent with the nominal fit, with some discrepancies in the W+jets control region and the 3J2T region for the muon channel.

Table 7.6: Multijet fit results with changed MC subtraction.

Region	Yield change	Scale factors	Event yields $BDT_{multijet} > -0.15$	$\frac{\chi^2}{NDF}$
2J1T	Up	Multijet: 0.65 ± 0.02 Signal-like: 1.17 ± 0.01	1451 ± 29 90188 ± 945	11.0
2J1T	Down	Multijet: 0.65 ± 0.01 Signal-like: 1.17 ± 0.01	1770 ± 30 89867 ± 835	11.1
2J0T	Up	Multijet: 0.91 ± 0.02 Signal-like: 1.05 ± 0.01	9743 ± 126 1133863 ± 3890	66.9
2J0T	Down	Multijet: 0.91 ± 0.01 Signal-like: 1.04 ± 0.01	18579 ± 179 1126906 ± 3006	69.3

Conclusion

In what follows, we use the data-driven multijet estimate. The uncertainty on the multijet rate is conservatively set to ±50%, which covers the estimated statistical and systematic uncertainties discussed above. In addition, we use the shape differences obtained with different isolation selections for the template as discussed in section 7.3.3 as a shape uncertainty.

The distribution of the $BDT_{multijet}$ discriminant is shown in figure 7.10.

7.4 W+jets Model Correction and Validation

After the multijet events contribution to the signal region has been estimated, the agreement between the SM expectation and the data is verified in several control regions for all the $BDT_{W/t\bar{t}}$ inputs, the $BDT_{W/t\bar{t}}$ response, the $\cos\theta^*_\mu$ variable, and a number of additional variables. In the 2J0T control region,$\cos\theta^*_\mu$ and p_T of the reconstructed W boson are observed to be mismodelled, This region is expected to be enriched in events with a W boson produced in association with jets from gluon fragmentation.

7.4.1 W+jets p_T Reweighting

The mismodelled p_T^W distribution is shown in figure 7.11(a). It is corrected for by reweighting the distribution to data after contributions from

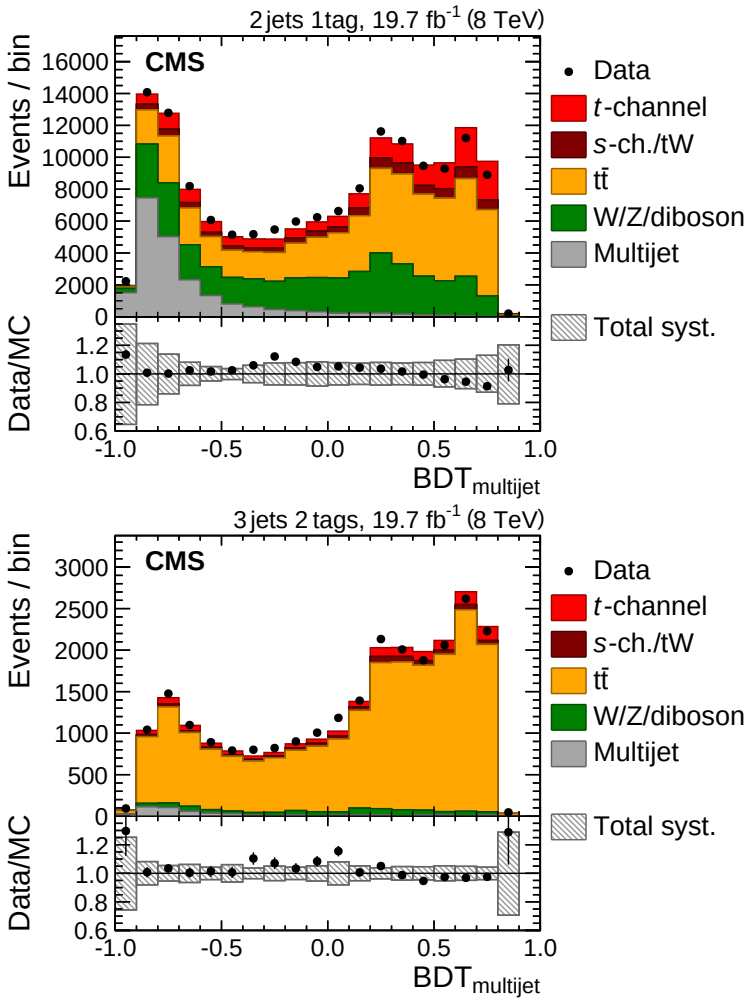

Figure 7.10: Distributions of the $BDT_{multijet}$ discriminant in the 2J1T (top) and 3J2T (bottom) categories. The predictions are normalised to the results of the fit described in section 7.8. The bottom panels in both plots show the ratio between observed and predicted event counts, with a shaded area to indicate the systematic uncertainties affecting the background prediction and vertical bars indicating statistical uncertainties.

other processes have been subtracted. The weights obtained in 2J0T are applied to all W+jets events in the analysis and the difference between applying and not applying them is taken as a systematic uncertainty. Figure 7.11(b) shows the reweighted distribution. This procedure does not have a considerable effect in 2J1T.

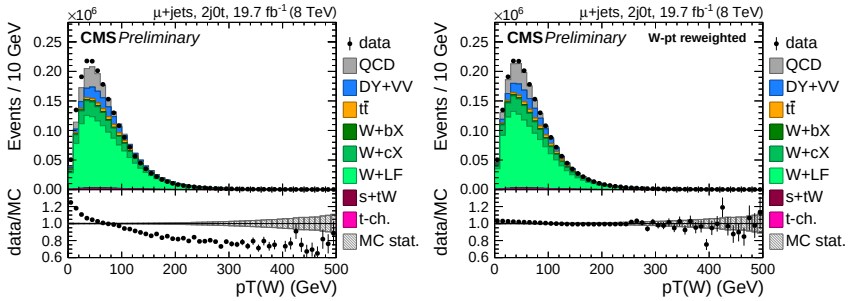

(a) before (b) after

Figure 7.11: W+jets p_{T} reweighting (a) before and (b) after applying the reweighting.

7.4.2 W+jets $\cos\theta^*_\mu$ Reweighting

The mismodelled $\cos\theta^*_\mu$ distribution is shown in figure 7.12(a). A similar disagreement between data and the MADGRAPH prediction in the $\cos\theta^*_\mu$ distribution is observed in the context of the cross section measurement at 7 TeV [1]. Although this control region is not used for the measurement, investigation was performed to check whether this mismodelling can also affect the signal region.

Comparing the MADGRAPH modelling with the one provided with SHERPA shows that SHERPA provides a better description of the $\cos\theta^*_\mu$ shape in this control region at both centre-of-mass energies. This is illustrated in figure 7.12(c)

However, in the kinematic region studied by this analysis, SHERPA was not able to reproduce the W+jets kinematic distributions as well as MADGRAPH, it was decided to deploy a reweighting procedure of the $\cos\theta^*_\mu$ shape and use the MADGRAPH/SHERPA shape difference as an

additional uncertainty. In addition, for computational reasons, the used SHERPA sample was produced with the simplification of $m_c = m_b = 0$, causing the relative fraction of heavy quarks to be equal to that of light quarks, which is unrealistically large. When reweighting the fractions of different final states ($W + bb$, $W + bc$, $W + bX$, $W + cc$, $W + cX$, $W + gg$, $W + gX$, $W + XX$ where $X = (u, d, s)$) in SHERPA to those in MADGRAPH, we obtain the distribution shown in figure 7.12(d) and the reweighing is applied taking this into account. The result of the reweighing is shown in figure 7.12(b). From these comparisons can observed that the optimal shape seems to lie somewhere between the reweighted and MADGRAPH shapes. We assign an uncertainty to this procedure corresponding to the shape difference between the two cases, which includes this optimal shape.

The reweighting scale factors obtained from 2J0T are applied to 2J1T, and corresponding plots shown with $\mathrm{BDT}_{\mathrm{W/t\bar{t}}} < 0$ in figure 7.13. Here, the W+light jet component is small and the reweighting has a negligible effect on the distribution, which is well modelled.

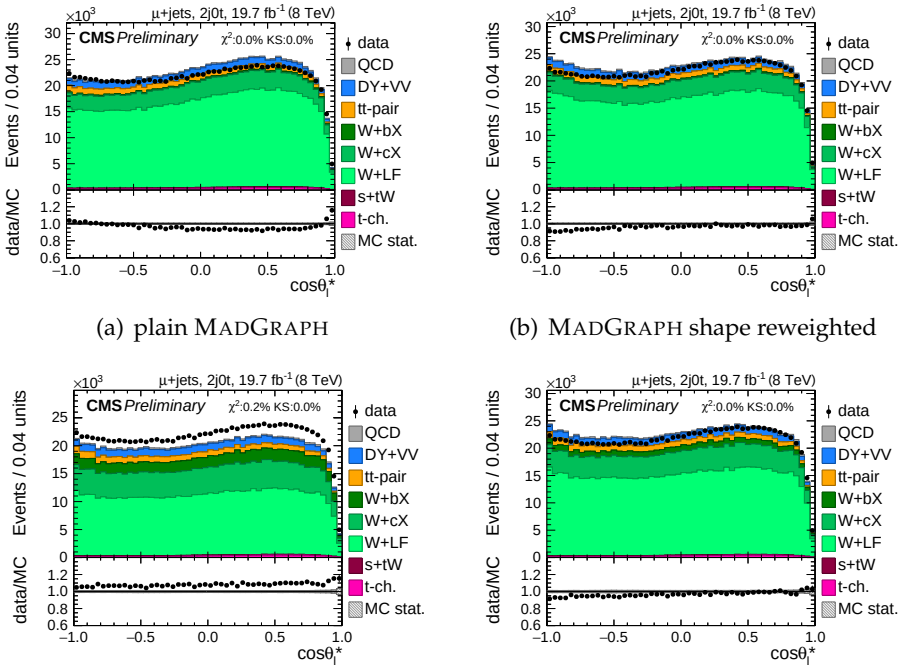

(a) plain MADGRAPH

(b) MADGRAPH shape reweighted

(c) plain SHERPA

(d) SHERPA flavour fractions reweighted

Figure 7.12: W+jets reweighting in 2J0T control region. The $\cos\theta^*_\mu$ shape in the using (a) plain MADGRAPH, (b) MADGRAPH shape reweighted to the SHERPA shape (used in the analysis), (c) plain SHERPA (c), and (d) SHERPA with flavour fractions reweighted to the flavor fractions of MADGRAPH (d)

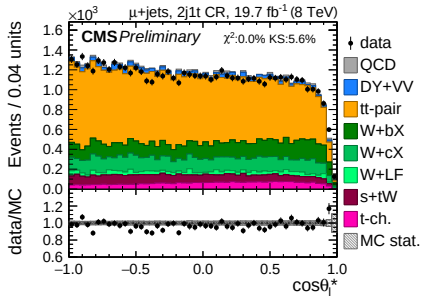

(a) plain MADGRAPH

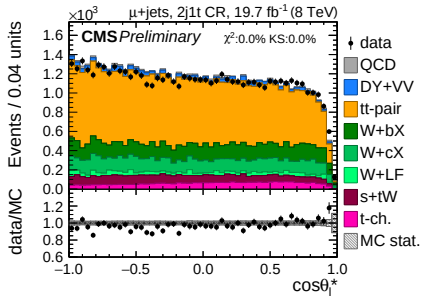

(b) MADGRAPH shape reweighted

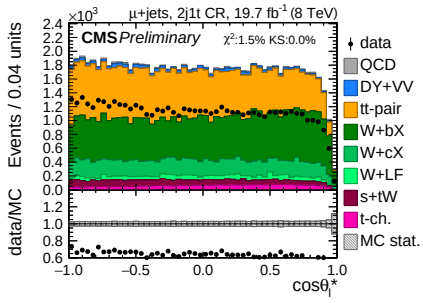

(c) plain SHERPA

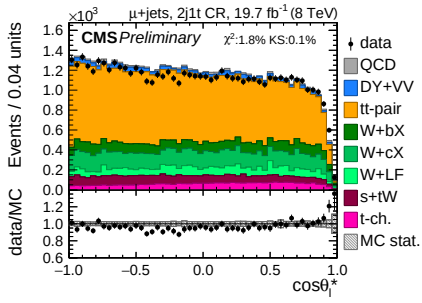

(d) SHERPA flavor fractions reweighted

Figure 7.13: W+jets reweighting in 2J1T with $\mathrm{BDT}_{\mathrm{W}/\mathrm{t\bar{t}}} < 0$.

7.5 Rejection of $t\bar{t}$ and W+jets Backgrounds

To discriminate between signal events and the primary backgrounds (W+jets, $t\bar{t}$), we train a BDT, $BDT_{W/t\bar{t}}$. We train on events passing the HLT and containing exactly 1 tight muon and 0 additional loose leptons, and additionally passing the anti-multijet selection. $BDT_{W/t\bar{t}}$ was trained and tested on statistically independent simulated datasets, and the events are weighted by the cross-section and the pile-up corrections. The signal training and testing events are selected from the 2J1T region, while for the backgrounds, additional events are selected also from the 2J0T and 3J2T control regions to improve discrimination against different kinds of $t\bar{t}$ and W+jets events.

7.5.1 Discriminating Variables

In training $BDT_{W/t\bar{t}}$ we use the following variables, which are ranked by the BSS method:

1. $m_{b\mu\nu}$ - the reconstructed top quark candidate mass
2. p_T^{μ} - transverse momentum of the muon
3. $|\eta_{j'}|$ - the pseudorapidity of the light quark jet
4. m_b - mass of the b-tagged jet
5. $|\eta_b|$ - the pseudorapidity of the b-tagged jet
6. $\not{E}_T$ - missing transverse energy
7. H_t - the transverse momentum of the hadronic final state system, i.e. $\left(\vec{p}_b + \vec{p}_{j'}\right)_T$
8. $\hat{S}$ - the total invariant mass of the top quark candidate and light quark system
9. p_T^b - transverse momentum of the b-tagged jet
10. $m_T(W)$ - transverse mass of the W-boson candidate

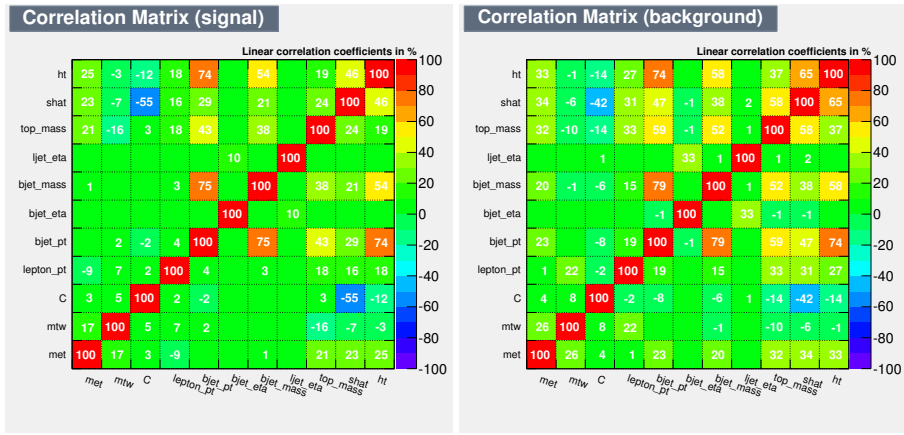

Figure 7.14: BDT candidate variable correlations for signal (left) and background (right).

The correlations between the variables are shown in figure 7.14

We validate the BDT input variables by comparing the prediction to measured data in 2J1T. All of the variables are well modelled, with some of them shown in figures 7.15 to 7.22, where the scale factors derived from the fit described in section 7.8 are applied on the components.

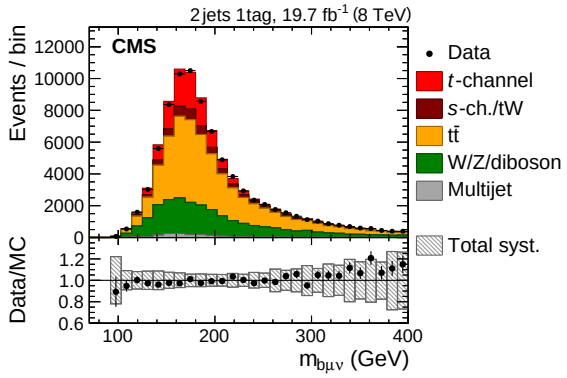

Figure 7.15: Distributions of the $m_{b\mu\nu}$ variable in the 2J1T category. From this figure on, unless specified otherwise, all the following descriptions apply. Rejection of multijet events is performed by requiring $\mathrm{BDT}_{\mathrm{multijet}} > -0.15$. The predictions are normalised to the results of the fit described in section 7.8. The bottom panel shows the ratio between observed and predicted event counts, with a shaded area to indicate the systematic uncertainties affecting the background prediction and vertical bars indicating statistical uncertainties.

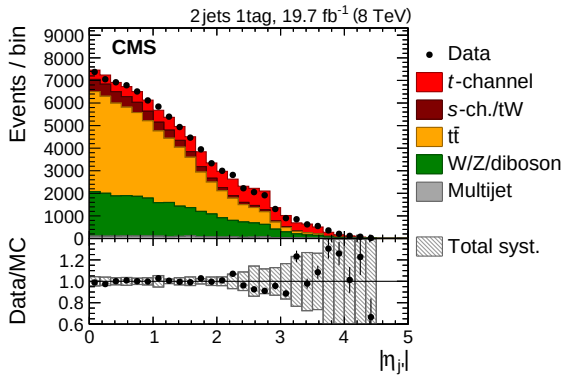

Figure 7.16: Distribution of the $|\eta_{j'}|$ variable in the 2J1T category.

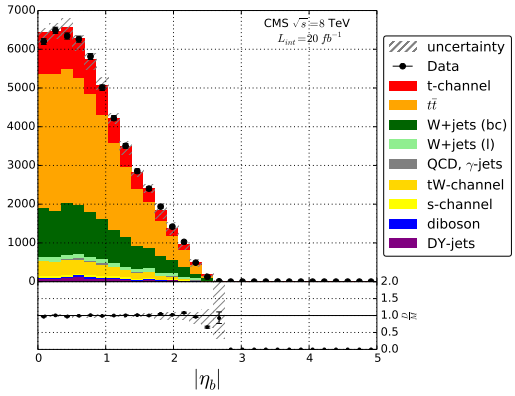

Figure 7.17: Predicted and observed distributions of the absolute value of the pseudorapidity of the b-tagged jet.

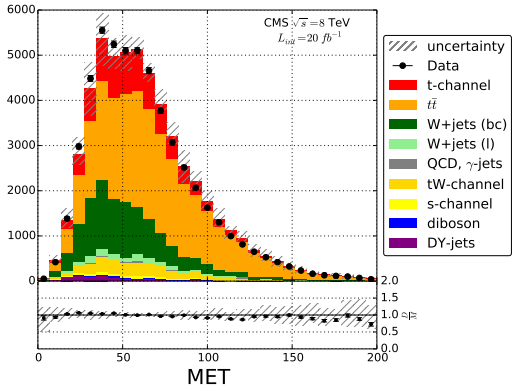

Figure 7.18: Predicted and observed distributions of the missing transverse energy.

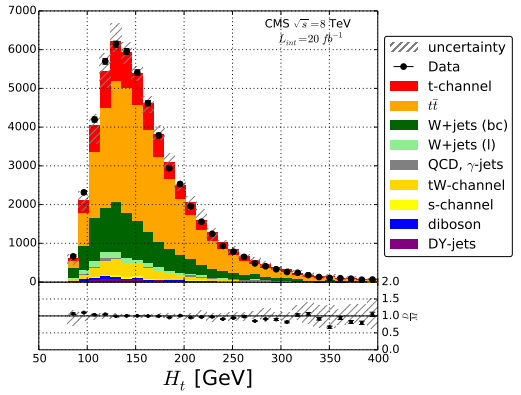

Figure 7.19: Predicted and observed distributions of the scalar sum of the hadronic transverse momenta.

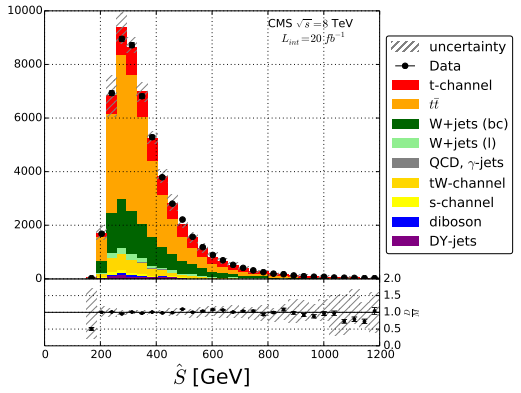

Figure 7.20: Predicted and observed distributions of the invariant mass of the top quark candidate and the light jet system.

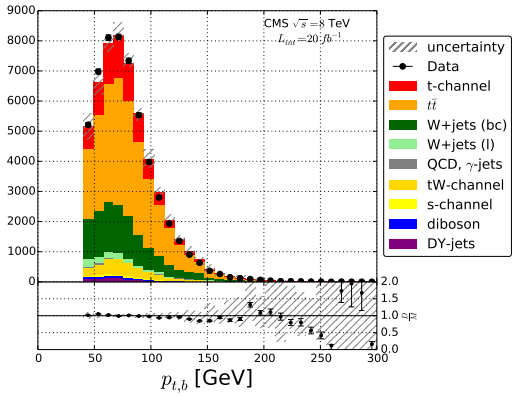

Figure 7.21: Predicted and observed distributions of the transverse momenta of the jet with the highest b-discriminator value.

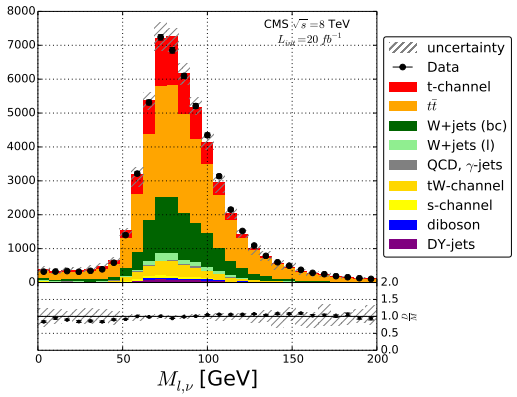

Figure 7.22: Predicted and observed distributions of the reconstructed W boson mass.

7.5.2 BDT Outputs

We check for overtraining by comparing the $BDT_{W/t\bar{t}}$ distributions as predicted by MC for the signal and background testing and training datasets. The shapes are found to be compatible, as seen on figure 7.23.

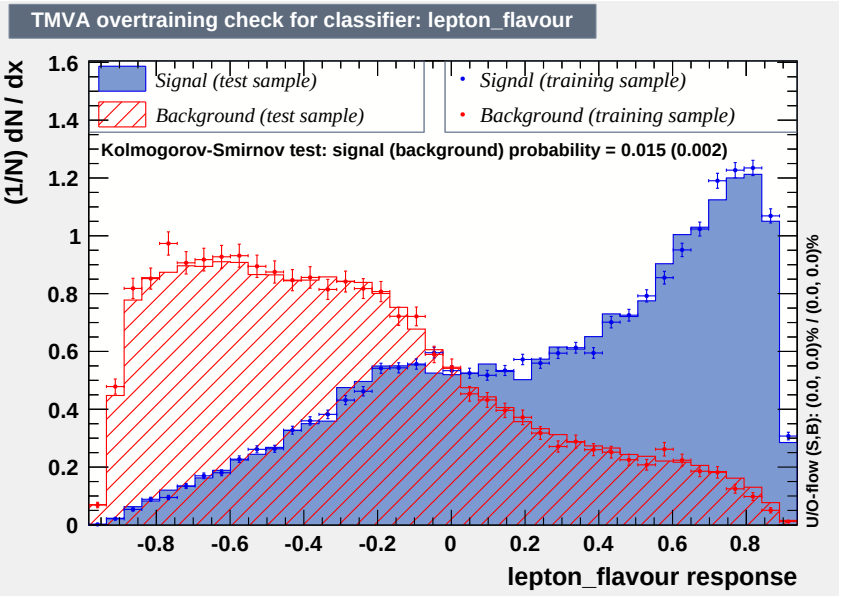

Figure 7.23: The overtraining check for the $BDT_{W/t\bar{t}}$ classifier. The training and test samples are statistically independent both for signal (blue) and background (red). All the training and test events are included in the plot. No significant overtraining is observed.

Figure 7.24 shows the distribution of the $BDT_{W/t\bar{t}}$ discriminant in the 2J1T and 3J2T categories after applying the selection requirement on the $BDT_{multijet}$ discriminant.

Working point selection

The optimal working point for the $BDT_{W/t\bar{t}}$ discriminant discriminant is selected by studying the analysis sensitivity with pseudo-data from

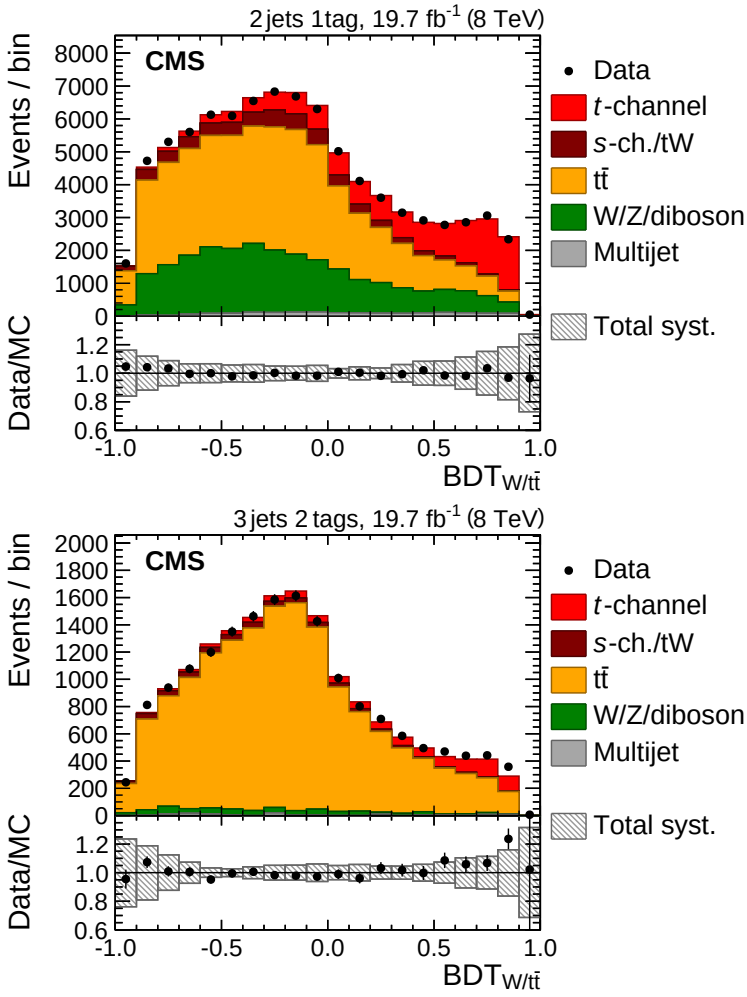

Figure 7.24: Distributions of the $\mathrm{BDT}_{\mathrm{W}/\mathrm{t\bar{t}}}$ discriminant in the 2J1T (top) and 3J2T (bottom) categories.

simulated events. Figure 7.25 shows the expected uncertainty at different working points, the treatment of systematic uncertainties is explained in section 7.10. Additionally, the contributions of some of the major uncertainties are depicted. At very high working points ($BDT_{W/t\bar{t}} > 0.7$) the procedure breaks down because of limited number of events in the samples for systematic uncertainties. The optimal working point is found to be $BDT_{W/t\bar{t}}$ discriminant > 0.45.

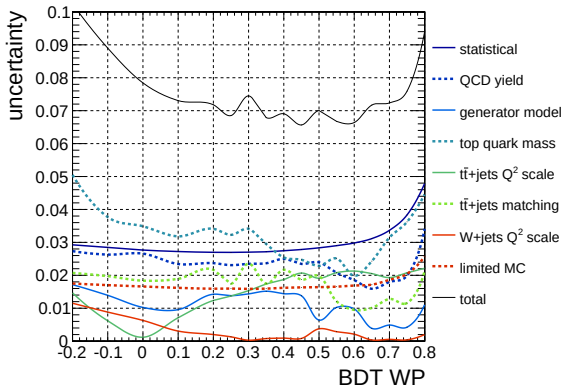

Figure 7.25: Optimisation of the $BDT_{W/t\bar{t}}$ working point.

7.6 $t\bar{t}$ Model Validation

The MADGRAPH model of $t\bar{t}$ production is known to predict a harder top quark p_T (p_T^t) spectrum than is observed in data [108, 109]. The spectrum of generator-level top quarks in $t\bar{t}$ events is therefore reweighted to reproduce the measured differential cross section as a function of p_T^t.

To validate the modelling of $t\bar{t}$ events, we compare simulated events to data in the 3J1T and 3J2T control regions. The most most relevant observables, $BDT_{multijet}$ and $BDT_{W/t\bar{t}}$ discriminants, and the $\cos\theta_\mu^*$ distribution, are shown for 3J2T in figures 7.10 (right), 7.24 (right), and 7.26 (right), respectively. The 3J2T region is also used in the fit described in section 7.8. After applying the p_T^t reweighting, the $t\bar{t}$ modelling provided by MADGRAPH is found to be in reasonable agreement with data.

7.7 The $\cos\theta_\mu^*$ Distribution of Top Quark Decay Products

Figure 7.26 shows the reconstructed distribution of $\cos\theta_\mu^*$ in the 2J1T (for $BDT_{W/t\bar{t}} > 0.45$) and 3J2T categories. The observed distribution is expected to differ from the parton-level prediction because of detector effects and the kinematic selection, most notably in the small number of selected events close to $\cos\theta_\mu^* = 1$. In the ratio between data and simulation we observe a trend that suggests a slightly less asymmetric shape than predicted by the SM. In this measurement, we unfold the $\cos\theta_\mu^*$ differential cross section and perform a χ^2-fit on the unfolded distribution to estimate A_μ based on equation (1.23).

7.8 Extraction of Signal and Background Yields

The signal and background components are estimated by means of a simultaneous ML fit to the distribution of the $BDT_{W/t\bar{t}}$ discriminant in the 2J1T and 3J2T regions. The inclusion of the $t\bar{t}$-dominated 3J2T region in the fit is used to provide an additional constraint on the $t\bar{t}$ background and to reduce correlations of the estimated $t\bar{t}$ yield with other contributions.

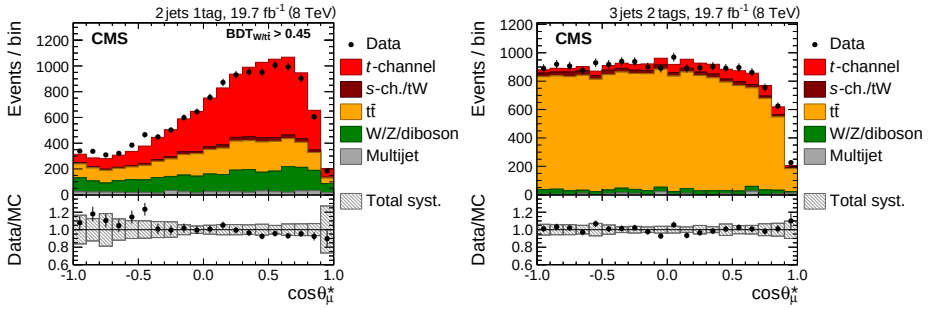

Figure 7.26: Distributions of $\cos\theta^*_\mu$ in the (left) signal region defined by $\mathrm{BDT}_{\mathrm{W/t\bar{t}}} > 0.45$ in the 2J1T category and (right) 3J2T control region. In both plots, the rejection of multijet events is performed by requiring $\mathrm{BDT}_{\mathrm{multijet}} > -0.15$. The predictions are normalised to the results of the fit described in section 7.8. The bottom panels in both plots show the ratio between observed and predicted event counts, with a shaded area to indicate the systematic uncertainties affecting the background prediction, and vertical bars indicating statistical uncertainties.

We use templates from MC simulation for all background processes except multijet events. The multijet events template is obtained from data by inverting the isolation selection as described in section 3.5.3 and its normalisation is kept fixed to the estimated yield described in section 7.3. Several processes with similar distributions in both $\cos\theta^*_\mu$ and the $\mathrm{BDT}_{\mathrm{W/t\bar{t}}}$ discriminant are merged to reduce the number of free parameters:

- Signal: t-channel single top quark production, treated as unconstrained.
- Top quark background: $\mathrm{t\bar{t}}$, s- and tW-channel single top quark production, with their relative fractions taken from simulation; a constraint of $\pm 20\%$ using a log-normal prior is applied.
- W/Z/diboson: W+jets, Z/γ^*+jets, and diboson production, with their relative fractions taken from simulation, having a constraint of $\pm 50\%$ using a log-normal prior.

The results of the three fits, and the post-fit uncertainties for top quark events, top antiquark events, and their combination, are presented as scale factors to be applied to simulation yields in table 7.7. Table 7.8 shows the

Table 7.7: Estimated scale factors and uncertainties from the simultaneous ML fit to the distribution of the $BDT_{W/t\bar{t}}$ discriminant in the 2J1T and 3J2T categories.

Processes	t	$\bar{t}$	$t+\bar{t}$
Signal	1.10 ± 0.03	1.20 ± 0.05	1.13 ± 0.03
Top quark bkg.	1.06 ± 0.02	1.08 ± 0.02	1.07 ± 0.01
W/Z/diboson	1.26 ± 0.05	1.21 ± 0.06	1.24 ± 0.04

Table 7.8: The expected number of signal and background events in the 2J1T signal region ($BDT_{W/t\bar{t}} > 0.45$) after scaling to the results of the ML fit. The uncertainties reflect the limited number of MC events and the estimated scale factor uncertainties, where appropriate.

Process	t	$\bar{t}$	$t+\bar{t}$
$t\bar{t}$	1543 ± 24	1573 ± 23	3118 ± 34
tW	143 ± 8	168 ± 9	311 ± 12
s-channel	44 ± 4	27 ± 3	72 ± 4
W+jets	1332 ± 60	1022 ± 56	2353 ± 81
Z/γ^*+jets	181 ± 23	189 ± 23	371 ± 32
Diboson	21 ± 2	13 ± 1	33 ± 2
Multijet	219 ± 110	208 ± 105	427 ± 214
t-channel	3852 ± 101	2202 ± 90	6049 ± 136
Total expected	7334 ± 165	5402 ± 153	12733 ± 271
Data	7223	5281	12504

number of events for different processes exceeding the threshold on the $BDT_{W/t\bar{t}}$ discriminant >0.45.

7.9 Unfolding

An unfolding procedure is used to determine the differential *t*-channel cross section as a function of $\cos\theta^*_\mu$ at the parton level. The procedure accounts for distortions caused by detector acceptance, selection efficiencies, imperfect reconstruction of the top quark candidate, and the

approximation made in treating the direction of the untagged jet as the spectator quark direction.

First, the remaining background contributions are subtracted from the reconstructed data distribution in 2J1T figure 7.26, using the fitted number of events and their uncertainties, estimated in section 7.8, to obtain the distribution of single top t-channel events. After that, an unfolding procedure described in section 4.2 is applied.

The parton-level definition of $\cos\theta^*_\mu$ in simulated events is based on the generated muon from the decay chain of a top quark or antiquark and the spectator quark scattering off the top quark or antiquark via virtual W boson exchange, with all momenta boosted into the rest frame of the generated top quark or antiquark. To preserve the spin information from the W decay, the response matrix takes into account the case in which the muon is from the $W \to \tau\nu \to \mu\nu\nu$ decay by unfolding the angular distribution to the τ lepton.

The performance of the unfolding algorithm is checked using sets of pseudo-experiments, which show no sign that the uncertainties are treated incorrectly. A bias test is performed by injecting anomalous Wtb-vertex coupling events, generated with COMPHEP, as pseudo-data. In general, the coupling structure can influence the distributions of the BDT input variables and thus the BDT output. The test results are shown in figure 7.27 and show that anomalous couplings can be correctly measured with our analysis. We observe a small bias that will be accounted for as a systematic uncertainty.

The value of A_μ is extracted using a χ^2-fit of the unfolded $\cos\theta^*_\mu$ distribution, taking into account the bin-by-bin correlations induced in the unfolding procedure, under the assumption that equation (1.23) holds. As a cross check, an alternative procedure, based on analytic matrix inversion with only two bins in the $\cos\theta^*_\mu$ distribution (corresponding to forward- and backward-going muons) is used. The results of the cross check are in agreement with the main result, but the expected precision of the analytic matrix inversion is slightly worse when tested using pseudo-data.

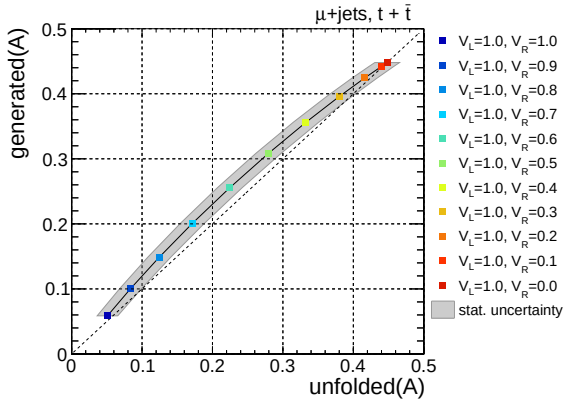

Figure 7.27: Comparison of generated and unfolded asymmetries for different Wtb coupling structures, estimated with pseudo-experiments. The uncertainty band quotes the expected statistical uncertainty only.

7.10 Systematic Uncertainties

The differential cross section and asymmetry measurement presented here can be affected by several sources of systematic uncertainty. The impact of each source is evaluated independently by using the corresponding systematically shifted simulated templates and response matrices to perform a new background estimation and repeating the measurement. The expected systematic uncertainty for each source is taken to be the maximal shift in the values of the asymmetry between the nominal asymmetry and the one measured using the shifted templates.

Most of the uncertainties are described in section 5, below are mentioned the systematical uncertainties specific to this measurement:

ML fit uncertainty is determined by propagating the uncertainty associated with the background normalisation from the fit through the unfolding procedure.

Other background fractions: An uncertainty is assigned to the fraction of each minor process that is combined with a larger shapewise-similar process in the fit. These are dibosons and Z/γ^*+jets production for the W/Z/diboson component, and the tW and *s*-channel production processes

for the top quark component. A yield uncertainty of 50% is used for each of those templates.

Multijet events background shape: A shape uncertainty is taken into account by changing the range of inverted isolation requirement to extract the multijet templates as described in section 7.3.2.

$\mathrm{t\bar{t}}$ top quark p_T reweighting: The p_T^t spectrum is reweighted as described in section 7.6. A systematic uncertainty is applied by either doubling the reweighting or not using any.

Top quark mass: Additional samples of $\mathrm{t\bar{t}}$ and signal events are generated with the top quark mass changed by $\pm 3\,\mathrm{GeV}/c^2$ to determine the effect of the uncertainty of the top quark mass. This is a conservative estimate as the current world average is $173.3 \pm 0.8\,\mathrm{GeV}/c^2$ [8].

$\cos\theta_\mu^*$ and W boson p_T reweighting in W+jets: The reweighting procedures are described is section 7.4.

Unfolding bias: A small bias in the unfolding procedure is described in section 7.9.

Table 7.9 shows the impact of the different sources of systematic uncertainties on the asymmetry measurements, while the same information is visualised in figure 7.28, compared to the results obtained with the 2-bin unfolding.

Table 7.9: List of systematic uncertainties and their induced shifts from the nominal measured asymmetry for the top quark ($\delta A_\mu(\mathrm{t})$), antiquark ($\delta A_\mu(\bar{\mathrm{t}})$), and their combination ($\delta A_\mu(\mathrm{t}+\bar{\mathrm{t}})$).

	$\frac{\delta A_\mu(\mathrm{t})}{10^{-2}}$	$\frac{\delta A_\mu(\bar{\mathrm{t}})}{10^{-2}}$	$\frac{\delta A_\mu(\mathrm{t}+\bar{\mathrm{t}})}{10^{-2}}$
Statistical	3.2	4.6	2.6
ML fit uncertainty	0.7	1.2	0.6
Diboson bkg. fraction	< 0.1	< 0.1	< 0.1
Z/γ^*+jets bkg. fraction	< 0.1	< 0.1	< 0.1
s-channel bkg. fraction	0.3	0.2	0.2
tW bkg. fraction	0.1	0.7	0.2
Multijet events shape	0.5	0.7	0.5
Multijet events yield	1.9	1.2	1.7
b tagging	0.7	1.2	0.9
Mistagging	< 0.1	0.1	< 0.1
Jet energy resolution	2.7	1.8	2.0
Jet energy scale	1.3	2.6	1.1
Unclustered $\not{E}_\mathrm{T}$	1.1	3.3	1.3
Pileup	0.3	0.2	0.2
Lepton identification	< 0.1	< 0.1	< 0.1
Lepton isolation	< 0.1	< 0.1	< 0.1
Muon trigger efficiency	< 0.1	< 0.1	< 0.1
Top quark p_T reweighting	0.3	0.3	0.3
W+jets W boson p_T reweighting	0.1	0.1	0.1
W+jets heavy-flavour fraction	4.7	6.2	5.3
W+jets light-flavour fraction	< 0.1	< 0.1	0.1
W+jets $\cos\theta^*_\mu$ reweighting	2.9	3.4	3.1
Unfolding bias	2.5	4.2	3.1
Generator model	1.6	3.5	0.3
Top quark mass	1.9	2.9	1.8
PDF	0.9	1.6	1.2
t-channel renorm./fact. scales	0.2	0.2	0.2
$\mathrm{t\bar{t}}$ renorm./fact. scales	2.2	3.4	2.7
$\mathrm{t\bar{t}}$ ME/PS matching	2.2	0.5	1.6
W+jets renorm./fact. scales	3.7	4.6	4.0
W+jets ME/PS matching	3.8	3.0	3.4
Limited MC events	2.1	3.2	1.8
Total uncertainty	10.5	13.8	10.5

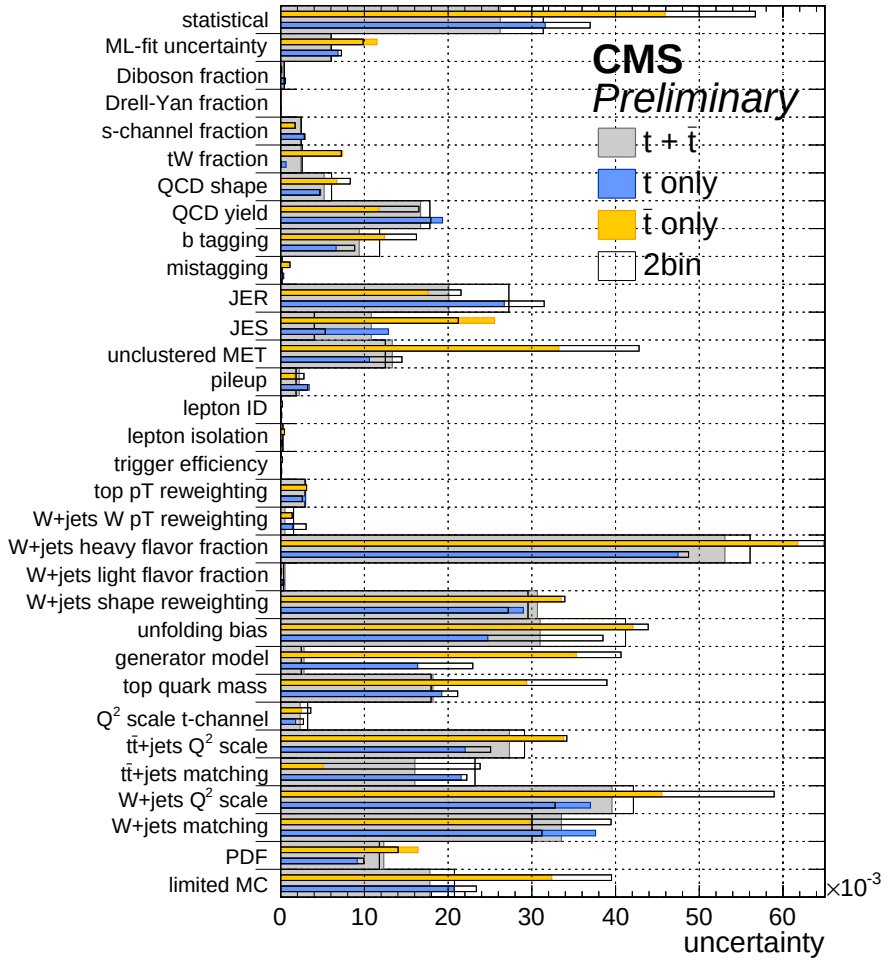

Figure 7.28: Impact of systematic uncertainties estimated using TUnfold compared to the 2-bin analytic method from pseudo-data.

7.11 Results

Figure 7.29 shows the differential cross sections obtained from the unfolding procedure for single top quark and antiquark production, and for their combination, with a comparison to the SM expectations from POWHEG, aMC@NLO, and COMPHEP. Uncertainties arising from the renormalisation and factorisation scale and PDF variations have been found to be negligible for the predicted differential distributions and are therefore not shown.

The asymmetry A_μ is extracted from the differential cross section according to equation. (1.23), taking into account correlations: We obtain the following values:

$$A_\mu(\mathrm{t}) = 0.29 \pm 0.03\,(\text{stat.}) \pm 0.10\,(\text{syst.}) = 0.29 \pm 0.11, \tag{7.1}$$

$$A_\mu(\bar{\mathrm{t}}) = 0.21 \pm 0.05\,(\text{stat.}) \pm 0.13\,(\text{syst.}) = 0.21 \pm 0.14, \tag{7.2}$$

$$A_\mu(\mathrm{t}+\bar{\mathrm{t}}) = 0.26 \pm 0.03\,(\text{stat.}) \pm 0.10\,(\text{syst.}) = 0.26 \pm 0.11, \tag{7.3}$$

The combined result is compatible with the SM with a p-value of $p(\text{data}|\text{SM}) = 4.6\%$, corresponding to a difference of 2.0 standard deviations compared to the expected SM asymmetry of 0.44 predicted by POWHEG (NLO). An alternative compatibility with the hypothetical case of $A_\mu = 0$ is smaller, yielding a p-value of $p(\text{data}|A_\mu = 0) = 0.7\%$, and corresponding to 2.7 standard deviations.

The SM asymmetry predictions for POWHEG simulated top quark and antiquark events are equal, while [9] predicts a $\mathcal{O}(1\%)$ difference, which is small compared to the precision of the current measurement.

The analytic 2-bin unfolding gives a compatible but slightly less precise value for A_μ of:

$$A_\mu(\mathrm{t}+\bar{\mathrm{t}}) = 0.28 \pm 0.03\,(\text{stat.}) \pm 0.1\,(\text{syst.}) = 0.28 \pm 0.12. \tag{7.4}$$

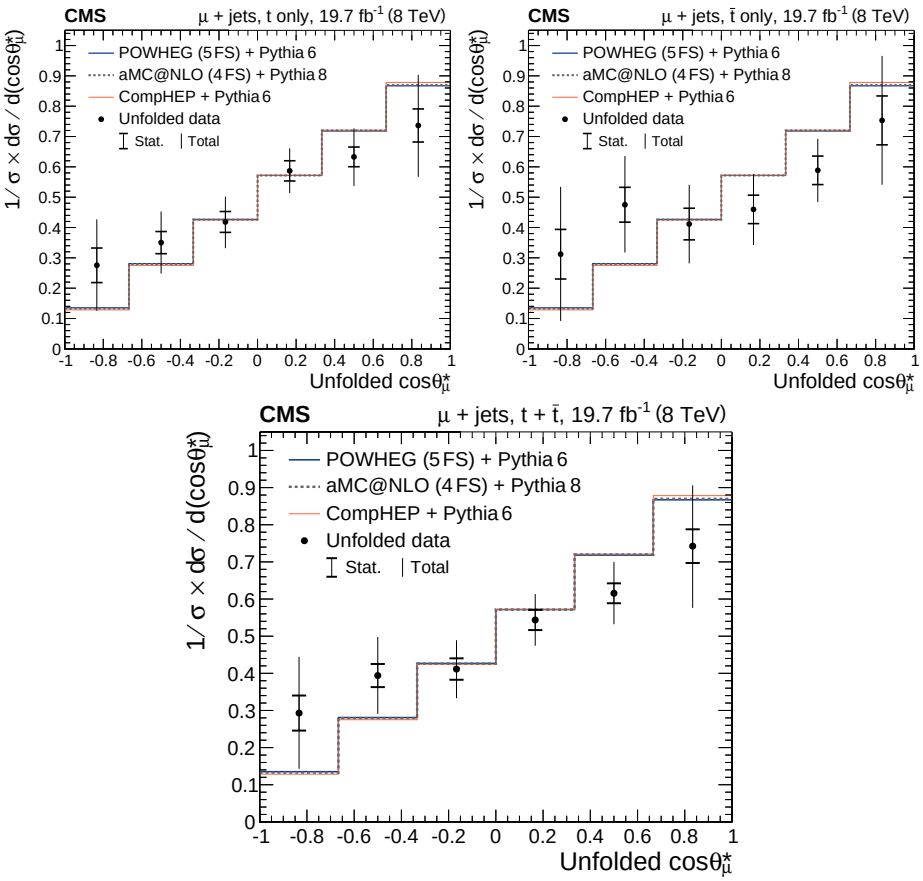

Figure 7.29: The normalised differential cross sections as a function of unfolded $\cos\theta^*_\mu$ for (top left) top quark, (top right) antiquark, and (bottom) top quark and antiquark combined, compared to the predictions from POWHEG, aMC@NLO, and CompHEP. The inner (outer) bars represent the statistical (total) uncertainties.

8 Conclusions

The main result of this thesis is the first measurement of the top quark spin asymmetry in t-channel single top quark production, sensitive to the top quark polarisation. It was performed based on a sample of pp collisions at a centre-of-mass energy of 8 TeV, corresponding to an integrated luminosity of $19.7\,\text{fb}^{-1}$.

The asymmetry, A_μ, is obtained by performing a differential cross section measurement of $\cos\theta^*_\mu$, between forward- and backward-going muons with respect to the direction of the spectator quark in the top quark rest frame. The measurement yields $A_\mu = 0.26 \pm 0.03\,(\text{stat.}) \pm 0.10\,(\text{syst.}) = 0.26 \pm 0.11$, which is compatible with a p-value of 4.6%, equivalent to 2.0 standard deviations, with the standard model expectation.

The asymmetry observed in data is smaller than the prediction. Separate results from exclusive top quark or antiquark events are compatible within the uncertainties. This difference cannot be explained by any single source of systematic uncertainty considered in the analysis.

The cross section of t-channel single top quark production has been measured in pp collisions at 7 TeV with improved precision compared to the previous CMS measurement at this energy. The measured value of the single top quark t-channel cross section is 67.2 ± 6.1 pb, which is the first measurement with a relative uncertainty below 10%. The total cross sections for production in the t-channel of single top quarks and individual single t and $\bar{\text{t}}$ have been measured in proton-proton collisions at the LHC at $\sqrt{s}$ = 8 TeV. The inclusive single top quark t-channel cross section has been measured to be $\sigma_{t\text{-ch.}} = 83.6 \pm 2.3\,(\text{stat.}) \pm 7.4\,(\text{syst.})$ pb. The single t and $\bar{\text{t}}$ cross sections have been measured to be $\sigma_{t\text{-ch.}}(\text{t}) = 53.8 \pm 1.5\,(\text{stat.}) \pm 4.4\,(\text{syst.})$ pb and $\sigma_{t\text{-ch.}}(\bar{\text{t}}) = 27.6 \pm 1.3\,(\text{stat.}) \pm 3.7\,(\text{syst.})$ pb, respectively. Their ratio has been found to be $R_{t\text{-ch.}} = 1.95 \pm 0.10\,(\text{stat.}) \pm 0.19\,(\text{syst.})$. The ratio of t-channel single top quark production cross sections at $\sqrt{s} = 8$ and 7 TeV has been measured to be $R_{8/7} = 1.24 \pm 0.08\,(\text{stat.}) \pm 0.12\,(\text{syst.})$.

These are the most precise measurements at 7 and 8 TeV and all of them are in agreement with the standard model predictions.

A comparison of the measurements of the inclusive cross section with the SM expectation obtained with a QCD computation at NLO with MCFM in the 5FS [110] and at NLO+NNLL [101] is shown in figure 8.1. The measurements $\sqrt{s} = 7\,\text{TeV}$ and $\sqrt{s} = 8\,\text{TeV}$ are compared to the Tevatron measurements at $\sqrt{s} = 1.96\,\text{TeV}$ [111, 12]. The error band (width of the curve) is obtained by varying the top quark mass within its uncertainty [112], estimating the PDF uncertainty according to the HEPDATA recommendations [113], and varying the factorisation and renormalisation scales coherently by a factor two up and down. The prediction in pp collisions can be also compared with the one at $p\bar{p}$ because the inclusive single top quark cross section does not depend on whether the light quark originates from a proton or from an antiproton.

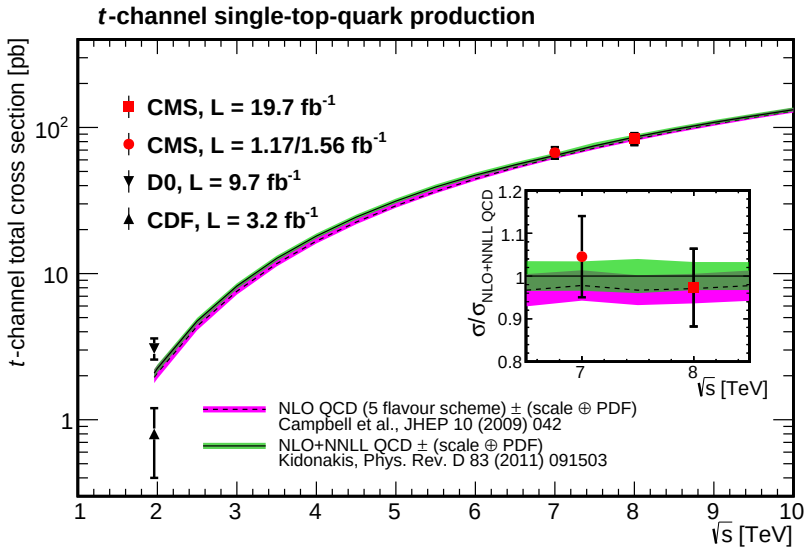

Figure 8.1: Single top quark production cross section in the t-channel versus collider centre-of-mass energy.

From the measured single top quark production cross section, the modulus of the CKM matrix element V_{tb} has been determined. The absolute value of the CKM matrix element V_{tb} is measured to be $|V_L V_{tb}| = \sqrt{\sigma_{t\text{-ch.}}/\sigma^{th}_{t\text{-ch.}}} = 1.020 \pm 0.046\,(\text{exp.}) \pm 0.017\,(\text{theo.})$ at 7 TeV. Combining this result with the measurement at 8 TeV, we get the most precise measurement of its kind to date: $|V_L V_{tb}| = 0.998 \pm 0.038\,(\text{exp.}) \pm 0.016\,(\text{theo.})$.

Assuming $V_L = 1$ and $|V_{tb}| \leq 1$, we measure the 95% confidence level interval $0.92 < |V_{tb}| \leq 1$.

9 Kokkuvõte - Üksiku t-kvargi omaduste mõõtmine CMS-detektoris

Pärast hiljutist Higgsi bosoni avastamist on leitud kõik osakestefüüsika standardmudeli (SM) poolt ennustatud osakesed. Ometi on põhjust arvata, et tegu pole lõpliku teooriaga, kuna mitmed nähtused, nagu tumeaine, neutriinode massid jms. ei ole standardmudeliga seletatavad. T-kvark on raskeim leitud elementaarosake, avastatud 1995. aastal Ta on väga eriline osake oma suure massi ja lühikese eluea ($\approx 4 \times 10^{-25}$ s) poolest, mille tõttu ta erinevalt teistest kvarkidest laguneb enne liitosakeste hadronite moodustamist. Oma omaduste tõttu mängib t-kvark olulist rolli SM-s ja paljudes selle laiendustes ning on seetõttu huvitav uurimisobjekt ning tema täpsete mõõtmiste abil saab kindlaks teha võimalikke kõrvalekaldeid SM ennustustest.

Enamus t-kvarkidest tekivad kvark-antikvark paaridena tugeva interaktsiooni kaudu gluuonite ühinemisel või kvark-antikvark paari annihileerumisel, kuid väiksemal määral t-(anti)kvarke tekib ka üksikult elektronõrga vastasmõju protsessides. Peamiseks üksikute t-kvarkide tekkemehhanismiks on t-kanal, $qb \rightarrow q't$ kus interaktsiooni toimub läbi virtuaalse W-bosoni vahetamise.

Üksikute t-kvarkide teket nähti esmakordselt alles hiljuti, 2009. aastal. Üksikute t-kvarkide abil on võimalik uurida mitmeid t-kvarkide omadusi paremini kui t-kvargi paaride abil, testides seeläbi SM ennustusi, ning ka paljud standardmudeli edasiarendused ennustavad nähtusi, mida on võimalik mõõta üksikute t-kvarkide abil.

Kõigi osakestefüüsika protsesside oluliseks omaduseks on tekkeristlõige σ, mis iseloomustab tõenäosust, et vastav protsess aset leiab. Tugev ja elektromagnetiline vastasmõju säilitavad kvarkide "lõhna," kuid nõrga interaktsiooni tõttu võib üht tüüpi kvark muutuda teiseks. Selliseid lõhna

muutvaid interaktsiooni kirjeldab Cabibbo-Kobayashi-Maskawa (CKM) segunemismaatriks.

Eeldustel, et CKM elementide vahel kehtivad seosed $V_{tb} \gg V_{td}$, $V_{tb} \gg V_{ts}$, on üksiku t-kvargi ristlõike ning t- ja b-kvarkide vahelise vasakukäelise vektorsidestusteguri V_L korrutis võrdeline $|V_{tb}|^2$-ga: $|V_L V_{tb}| = \sqrt{\sigma_{t\text{-kanal}} / \sigma^{\text{teor.}}_{t\text{-kanal}}}$. V_L väärtus SM-s on 1, kuid mitmed alternatiivsed teooriad ennustavad sellele teistsugust väärtust ning seeläbi on antud suuruse mõõtmine heaks vahendiks nende kontrollimisel, võimaldades näiteks avastada uute kvargisarnaste osakeste olemasolu.

Teine huvitav omadus on üksiku t-kvargi polarisatsioon. Oma lühikese eluea tõttu laguneb t-kvark enne kui tema spinn on jõudnud tugeva interaktsiooni tõttu muutuda ja seetõttu saab seda üksiku t-kvargi laguproduktide kaudu mõõta, kusjuures SM ennustab, et kõik elektronõrga interaktsiooni kaudu tekkinud t-kvargid peaksid olema vasakukäelised.

Suur Hadronite Põrguti (LHC) on 27 km pikkune maailma suurim ja kõrgeima energiaga osakeste kiirendi, kus põrgatatakse vastassuundades liikuvaid prootonite kimpe energiatel kuni 14 TeV.

LHC-s tegutseb seitse eksperimenti, neist ATLAS ja CMS on üldotstarbelised detektorid paljude erinevate osakesefüüsika protsesside mõõtmiseks. Antud töö kasutab CMS-iga tehtud mõõtmisi.

CMS detektori keskseks komponendiks on 6 m läbimõõduga ülijuhtiv solenoidmagnet, mille sees on silikoonist piksel- ja ribadetektoritest koosnev trajektoorimõõtja, pliivolframaadi kristallidest elektromagnetiline kalorimeeter ning messingist ja stsintilaatoritest hadronkalorimeeter. Väljaspool solenoidi on kambrid müüonite mõõtmiseks. CMS-i üldpikkus on 22 m, diameeter 15 m ja mass 14000 t. Detektoris toimuvad põrked intervalliga 25 ns, huvitavamate parameetritega sündmused salvestatakse päästikusüsteemi abil hilisemaks uurimiseks ning mõõtmistest rekonstrueeritakse erinevad osakesed algoritmiga, mis võtab arvesse kõigist alamdetektoritest saadud andmeid.

Käesolev doktoritöö kirjeldab üksiku t-kvargi tekkeristlõike mõõtmist masskeskme energiatel 7 TeV ja 8 TeV ning üksiku t-kvargi polarisatsiooni mõõtmist energial 8 TeV. Detektoris toimunud põrgete arvu iseloomustab integreeritud kirkus (ingl. k. *luminosity*), nii et integreeritud kirkuse $L = 1\,\text{fb}^{-1}$ korral leiab protsess ristlõikega $\sigma = 1\,\text{pb}$ aset keskmiselt $N = L \cdot \sigma = 1000$ korda.

Kõik käsitletud analüüsid kasutavad sarnast lähenemist, et saavutada võimalikult puhast valikut üksiku t-kvargi *t*-kanali sündmusi. Vaatleme t-kvarke, mis lagunevad leptoniliselt, st. t-kvark laguneb b-kvargiks ja W-bosoniks ning W-boson omakorda elektroniks või müüoniks ja vastavaks neutriinoks. Selliste sündmuste mõõtmisel näeme detektoris elektroni või müüonit, mõõtmata jääva neutriino tõttu puuduolevat energiat ja kahte osakeste juga. Joad on põhjustatud kvarkide poolt, mis tugeva interaktsiooni tõttu ei saa vabalt eksisteerida ja moodustavad hadroneid. Lisaks nõuame, et üks jugatest oleks märgistatud b-joana, mis tähendab, et suure tõenäosusega sai ta alguse b-kvargist. T-kvargi rekonstrueerime müüonist või elektronist, b-joast ja neutriinost.

Signaali-ja taustaprotsesside modelleerimiseks kasutatakse Monte Carlo (MC) simulatsioone või hinnatakse nende omadusi andmete kontrollpiirkondades tehtud mõõtmiste alusel. Simuleeritud põrgete mõõtmistega võrreldavuse tagamiseks läbivad need ka detektori simulatsiooni. Üksiku *t*-kvargi sündmuste eristamiseks muude sarnase signatuuriga protsesside sündmustest kasutame nendevahelistele erinevustele tundlikke muutujaid nagu puuduolev energia $\not{E}_{\mathrm{T}}$, rekonstrueeritud W-bosoni ja t-kvargi massid ($m_{\mathrm{T}}(\mathrm{W})$ ja $m_{\mathrm{b}\mu\nu}$) ning b-joana märgistamata osakeste joa pseudonobedus $|\eta_{j'}|$. Mõnel puhul kasutame ka neist ja muudest muutujatest konstrueeritud mitme muutuja klassifikaatoreid.

Üksiku t-kvargi tekkeristlõige *t*-kanalis on mõõdetud masskeskme energia 7 TeV juures, kasutades 1.17 fb^{-1} andmeid, kus t-kvark (või antikvark) laguneb müüoniks ja 1.56 fb^{-1} andmeid, kus t-kvark (või antikvark) laguneb elektroniks. Tulemuseks on ristlõige 67.2 ± 6.1 pb. See on esimene üksiku t-kvargi ristlõike mõõtmine, mille suhteline määramatus on alla 10%.

Teine mõõtmine on teostatud masskeskme energia 8 TeV juures, kasutades 19.7 fb^{-1} põrkeandmeid nii müüon- kui elektronkanalis. T-kvarkide ja antikvarkide kombineeritud ristlõikeks *t*-kanalis mõõtsime $\sigma_{t\text{-kanal}} = 83.6 \pm 2.3\,(\mathrm{stat.}) \pm 7.4\,(\mathrm{süst.})$ pb. Mõõtmine on teostatud ka eraldi kvarkide ja antikvarkide jaoks, ning tulemused on $\sigma_{t\text{-kanal}}(\mathrm{t}) = 53.8 \pm 1.5\,(\mathrm{stat.}) \pm 4.4\,(\mathrm{süst.})$ pb ja $\sigma_{t\text{-kanal}}(\bar{\mathrm{t}}) = 27.6 \pm 1.3\,(\mathrm{stat.}) \pm 3.7\,(\mathrm{süst.})$ pb. Nende suhteks on $R_{t\text{-kanal}} = 1.95 \pm 0.10\,(\mathrm{stat.}) \pm 0.19\,(\mathrm{süst.})$. Üksiku t-kvargi *t*-kanali ristlõigete suhe energiate 8 TeV ja 7 TeV jaoks on $R_{8/7} = 1.24 \pm 0.08\,(\mathrm{stat.}) \pm 0.12\,(\mathrm{süst.})$. Kõik need mõõtmised on SM ennustustega kooskõlas.

Mõõdetud ristlõikest 7 TeV juures on leitud CKM maatrikselemendi V_{tb} väärtus: $|V_L V_{\mathrm{tb}}| = \sqrt{\sigma_{t\text{-kanal}} / \sigma^{\text{teor.}}_{t\text{-kanal}}} = 1.020 \pm 0.046(\text{eksp.}) \pm 0.017(\text{teor.})$. Kombineerides selle tulemuse mõõtmisega 8 TeV juures, saame täpseima seni mõõdetud tulemuse: $|V_L V_{\mathrm{tb}}| = 0.998 \pm 0.038(\text{eksp.}) \pm 0.016(\text{teor.})$ ning kui eeldata, et $V_L = 1$ ja $|V_{\mathrm{tb}}| \leq 1$, saame seada piirangu $0.92 < |V_{\mathrm{tb}}| \leq 1$ 95% usaldusnivool.

Doktoritöö peamiseks tulemuseks on üksiku t-kvargi spinnasümmeetria A_X esmakordne mõõtmine. Spinnasümmeetria, mis on seotud t-kvargi polarisatsiooniga $P_{\mathrm{t}}^{(\vec{s})}$seose $A_X \equiv \frac{1}{2} \cdot P_{\mathrm{t}}^{(\vec{s})} \cdot \alpha_X$ kaudu, kus α_X on t-kvargi laguprodukti niinimetatud spinnianalüüsivõime, kusjuures müüonite jaoks SM-s $\alpha_\mu = 1$. See mõõtmine on sooritatud masskeskme energial 8 TeV, kasutades 19.7 fb^{-1} andmeid, kus t-kanali kaudu tekkinud t-kvark laguneb läbi müüonkanali.

Asümmeetria mõõtmiseks kasutame üksiku t-kvargi diferentsiaalset ristlõiget sõltuvalt nurgast $\cos\theta^*_\mu$ t-kvargi lagunemisel tekkinud müüoni ja t-kvargi tekkeprotsessi kaasnähtusena tekkinud kerge kvargi vahel t-kvargi taustsüsteemis. Saadud jaotus muudetakse otseselt võrreldavaks teoreetiliste ennustustega sidudes lahti (ingl. k. *unfold/deconvolute*) $\cos\theta^*_\mu$ tõelise jaotuse detektori efektidest ja sündmuste valiku mõjust. Asümmeetria on arvutatav kui $A_\mu = \frac{N(\uparrow) - N(\downarrow)}{N(\uparrow) + N(\downarrow)}$, kus $N(\uparrow)$ ja $N(\downarrow)$ on vastavalt kerge kvargiga sama- ja vastassuunaliste müüonite arvud. Mõõtmistulemuseks on $A_\mu = 0.26 \pm 0.03\,(\text{stat.}) \pm 0.10\,(\text{syst.}) = 0.26 \pm 0.11$, mis on SM ootevääртusega kooskõlas p-väärtusega 4.6%, mis vastab 2.0 standardhälbe suurusele erinevusele. Eraldi tulemused kvarkide ja antikvarkide jaoks on sellega määramatuste piires kooskõlas.

Acknowledgements

First, I would like to thank my supervisors. I thank Andrea Giammanco for his continued guidance and advice throughout my involvement in top quark physics. I thank Mario Kadastik for involving me in my first particle physics analysis and providing feedback. I thank Martti Raidal for welcoming me to the NICPB HEP group and reminding me of the bigger picture from time to time.

I would like to thank Matthias Komm and Joosep Pata for good collaboration. Additionally, I would like to thank Orso Iorio for his help in getting started with top quark analysis.

I would like to thank Jeremy Andrea and Patrizia Azzi for pre-reviewng the thesis and Oliver Maria Kind for agreeing to be the opponent. I am grateful to the CMS collaboration members from the single top group and elsewhere for providing valuable feedback. I greatly appreciate the work of my colleagues in the CERN accelerator departments for the excellent performance of the LHC and thank the technical and administrative staffs at CERN and at other CMS institutes for their contributions to the success of the CMS effort.

Special thanks go to KFV members for sharing the journey.

Thanks are also due to Michael Crichton and James Gleick for inspiring me to become a physicist.

Tänan Tiinat ja oma perekonda toetuse ja armastuse eest. Suur aitäh!

Bibliography

[1] **CMS** Collaboration, S. Chatrchyan *et al.*, "Measurement of the single-top-quark t-channel cross section in pp collisions at $\sqrt{s} = 7$ TeV," *JHEP* **12** (2012) 035, arXiv:1209.4533 [hep-ex].

[2] **CMS** Collaboration, V. Khachatryan *et al.*, "Measurement of the t-channel single-top-quark production cross section and of the $| V_{tb} |$ CKM matrix element in pp collisions at $\sqrt{s}$= 8 TeV," *JHEP* **06** (2014) 090, arXiv:1403.7366 [hep-ex].

[3] **CMS** Collaboration, V. Khachatryan *et al.*, "Measurement of top quark polarisation in t-channel single top quark production," *JHEP* **2016** no. 4, (2016) 1–42, arXiv:1511.02138 [hep-ex].

[4] M. Kobayashi and T. Maskawa, "CP-Violation in the renormalizable theory of weak interaction," *Progress of Theoretical Physics* **49** no. 2, (1973) 652–657.

[5] **CDF** Collaboration, F. Abe *et al.*, "Observation of top quark production in $\overline{p}p$ collisions with the Collider Detector at Fermilab," *Phys. Rev. Lett.* **74** (Apr, 1995) 2626–2631.

[6] **D0** Collaboration, S. Abachi *et al.*, "Observation of the top quark," *Phys. Rev. Lett.* **74** (Apr, 1995) 2632–2637.

[7] **Particle Data Group**, K. A. Olive, *et al.*, "Review of Particle Physics," *Chin. Phys.* **C38** (2014) 090001.

[8] The **ATLAS**, **CDF**, **CMS** and **D0** Collaborations, "First combination of Tevatron and LHC measurements of the top-quark mass," ATLAS-CONF-2014-008, CDF-NOTE-11071, CMS-PAS-TOP-13-014, D0-NOTE-6416, 2014. arXiv:1403.4427 [hep-ex].

[9] G. Mahlon and S. Parke, "Single top quark production at the LHC: Understanding spin," *Physics Letters B* **476** no. 3–4, (2000) 323 – 330.

[10] **ATLAS** Collaboration, G. Aad *et al.*, "Observation of a new particle in the search for the Standard Model Higgs boson with the ATLAS detector at the LHC," *Physics Letters B* **716** no. 1, (2012) 1 – 29.

[11] **CMS** Collaboration, S. Chatrchyan *et al.*, "Observation of a new boson at a mass of 125 GeV with the CMS experiment at the LHC," *Physics Letters B* **716** no. 1, (2012) 30 – 61.

[12] **CDF** Collaboration, T. Aaltonen *et al.*, "Observation of electroweak single top-quark production," *Phys. Rev. Lett.* **103** (Aug, 2009) 092002.

[13] **D0** Collaboration, V. M. Abazov *et al.*, "Observation of single top-quark production," *Phys. Rev. Lett.* **103** (Aug, 2009) 092001.

[14] **CMS** Collaboration, S. Chatrchyan *et al.*, "Observation of the associated production of a single top quark and a W boson in pp collisions at $\sqrt{s} = 8$ TeV," *Phys. Rev. Lett.* **112** (Jun, 2014) 231802.

[15] **ATLAS** Collaboration, G. Aad *et al.*, "Measurement of the production cross-section of a single top quark in association with a W boson at 8 TeV with the ATLAS experiment," *JHEP* **01** (2016) 064, `arXiv:1510.03752 [hep-ex]`.

[16] **CDF** Collaboration and **D0** Collaboration, "Observation of s-channel production of single top quarks at the Tevatron," *Phys. Rev. Lett.* **112** (Jun, 2014) 231803.

[17] **ATLAS** Collaboration, G. Aad *et al.*, "Evidence for single top-quark production in the s-channel in proton–proton collisions at with the ATLAS detector using the Matrix Element Method," *Physics Letters B* **756** (2016) 228 – 246.

[18] T. M. P. Tait and C.-P. Yuan, "Single top quark production as a window to physics beyond the standard model," *Phys. Rev. D* **63** (Dec, 2000) 014018.

[19] J. Aguilar-Saavedra, "Single top quark production at LHC with anomalous Wtb couplings," *Nucl. Phys. B* **804** (2008) 160.

[20] J. Aguilar-Saavedra, "A minimal set of top anomalous couplings," *Nuclear Physics B* **812** no. 1–2, (2009) 181 – 204.

[21] A. Giammanco, "Single top quark production at the LHC," *Reviews in Physics* **1** (2016) 1 – 12.

[22] G. L. Kane, G. A. Ladinsky, and C. P. Yuan, "Using the top quark for testing standard model polarization and CP predictions," *Phys. Rev. D* **45** (1992) 124.

[23] T. G. Rizzo, "Single top quark production as a probe for anomalous moments at hadron colliders," *Phys. Rev. D* **53** (1996) 6218, `arXiv:hep-ph/9506351 [hep-ph]`.

[24] J. Alwall, R. Frederix, J.-M. Gérard, A. Giammanco, M. Herquet, S. Kalinin, E. Kou, V. Lemaitre, and F. Maltoni, "Is $V_{tb} \approx 1$?," *Eur. Phys. J. C* **49** (2007) 791.

[25] J. Gao, C. S. Li, L. L. Yang, and H. Zhang, "Search for anomalous top quark production at the early LHC," *Phys. Rev. Lett.* **107** (2011) 092002.

[26] I. I. Y. Bigi, Y. L. Dokshitzer, V. A. Khoze, J. H. Kuhn, and P. M. Zerwas, "Production and decay properties of ultraheavy quarks," *Phys. Lett.* **B181** (1986) 157.

[27] G. Mahlon and S. Parke, "Angular correlations in top quark pair production and decay at hadron colliders," *Phys. Rev. D* **53** (May, 1996) 4886–4896.

[28] M. Jeżabek and J. Kühn, "V – A tests through leptons from polarised top quarks," *Physics Letters B* **329** no. 2–3, (1994) 317 – 324.

[29] J. Aguilar-Saavedra and J. Bernabéu, "W polarisation beyond helicity fractions in top quark decays," *Nuclear Physics B* **840** no. 1–2, (2010) 349 – 378.

[30] F. Bach and T. Ohl, "Anomalous top couplings at hadron colliders revisited," *Phys. Rev. D* **86** (Dec, 2012) 114026.

[31] **CDF** Collaboration, "The measurement of single-top polarization with 3.2 fb^{-1}," Conference Note CDF/PUB/TOP/PUBLIC/9920, FNAL, 2009. `http://www-cdf.fnal.gov/physics/new/top/2009/singletop/polarization/Public_pol_32.html`.

[32] O. S. Brüning, P. Collier, P. Lebrun, S. Myers, R. Ostojic, J. Poole, and P. Proudlock, *LHC Design Report*. CERN, Geneva, 2004. `https://cds.cern.ch/record/782076`.

[33] **ATLAS** Collaboration, G. Aad *et al.*, "The ATLAS experiment at the CERN Large Hadron Collider," *Journal of Instrumentation* **3** no. 08, (2008) S08003.

[34] **CMS** Collaboration, S. Chatrchyan *et al.*, "The CMS experiment at the CERN LHC," *Journal of Instrumentation* **3** (2008) S08004.

[35] **ALICE** Collaboration, K. Aamodt *et al.*, "The ALICE experiment at the CERN LHC," *Journal of Instrumentation* **3** no. 08, (2008) S08002.

[36] **LHCb** Collaboration, A. A. Alves Jr *et al.*, "The LHCb detector at the LHC," *Journal of Instrumentation* **3** no. 08, (2008) S08005.

[37] **TOTEM** Collaboration, G. Anelli *et al.*, "The TOTEM Experiment at the CERN Large Hadron Collider," *Journal of Instrumentation* **3** no. 08, (2008) S08007.

[38] **LHCf** Collaboration, O. Adriani *et al.*, "The LHCf detector at the CERN Large Hadron Collider," *Journal of Instrumentation* **3** no. 08, (2008) S08006.

[39] **MoEDAL** Collaboration, J. Pinfold *et al.*, "Technical Design Report of the MoEDAL Experiment," CERN-LHCC-2009-006. MoEDAL-TDR-001, CERN, Geneva, Jun, 2009. https://cds.cern.ch/record/1181486.

[40] **CMS** Collaboration, S. Chatrchyan *et al.*, "Description and performance of track and primary-vertex reconstruction with the CMS tracker," *Journal of Instrumentation* **9** (2014) P10009, arXiv:1405.6569 [physics.ins-det].

[41] **CMS** Collaboration, V. Khachatryan *et al.*, "Performance of photon reconstruction and identification with the CMS detector in proton-proton collisions at $\sqrt{s} = 8$ TeV," *Journal of Instrumentation* **10** no. 08, (2015) P08010, arXiv:1502.02702 [physics.ins-det].

[42] **CMS** Collaboration, "Particle–flow event reconstruction in CMS and performance for jets, taus, and $\not\!\!E_{\mathrm{T}}$," CMS Physics Analysis Summary CMS-PAS-PFT-09-001, 2009. http://cdsweb.cern.ch/record/1194487.

[43] **CMS** Collaboration, "Commissioning of the particle-flow event reconstruction with the first LHC collisions recorded in the CMS detector," CMS Physics Analysis Summary CMS-PAS-PFT-10-001, 2010. http://cdsweb.cern.ch/record/1247373.

[44] **CMS** Collaboration, V. Khachatryan *et al.*, "Performance of electron reconstruction and selection with the CMS detector in proton-proton collisions at $\sqrt{s} = 8$ TeV," *Journal of Instrumentation* **10** no. 6, (2015) P06005, arXiv:1502.02701 [physics.ins-det].

[45] R. Frühwirth, "Application of Kalman filtering to track and vertex fitting," *Nuclear Instruments and Methods in Physics Research Section A: Accelerators, Spectrometers, Detectors and Associated Equipment* **262** no. 2–3, (1987) 444 – 450.

[46] **CMS** Collaboration, S. Chatrchyan *et al.*, "Performance of CMS muon reconstruction in pp collision events at $\sqrt{s} = 7$ TeV," *Journal of Instrumentation* **7** (2012) P10002, arXiv:1206.4071 [physics.ins-det].

[47] M. Cacciari, G. P. Salam, and G. Soyez, "The anti-k_t jet clustering algorithm," *JHEP* **04** (2008) 063, arXiv:0802.1189 [hep-ex].

[48] **CMS** Collaboration, S. Chatrchyan *et al.*, "Determination of jet energy calibration and transverse momentum resolution in CMS," *Journal of Instrumentation* **6** (2011) P11002, arXiv:1107.4277 [physics.ins-det].

[49] T. Sjöstrand, S. Mrenna, and P. Z. Skands, "PYTHIA 6.4 physics and manual," *JHEP* **05** (2006) 026, arXiv:0603175 [hep-ph].

[50] T. Sjöstrand, S. Ask, J. R. Christiansen, R. Corke, N. Desai, P. Ilten, S. Mrenna, S. Prestel, C. O. Rasmussen, and P. Z. Skands, "An introduction to PYTHIA 8.2," *Comput. Phys. Commun.* **191** (2015) 159, arXiv:1410.3012 [hep-ph].

[51] S. Höche, F. Krauss, M. Schonherr, and F. Siegert, "Automating the POWHEG method in SHERPA," *JHEP* **04** (2011) 024, arXiv:1008.5399 [hep-ph].

[52] S. Höche, F. Krauss, M. Schonherr, and F. Siegert, "W+n-jet predictions at the Large Hadron Collider at Next-to-Leading Order matched with a parton shower," *Phys. Rev. Lett.* **110** (2013) 052001, arXiv:1201.5882 [hep-ph].

[53] S. Jadach, J. H. Kuhn, and Z. Was, "TAUOLA: A library of Monte Carlo programs to simulate decays of polarized τ leptons," *Comput. Phys. Commun.* **64** (1990) 275.

[54] S. Frixione, P. Nason, and C. Oleari, "Matching NLO QCD computations with parton shower simulations: the POWHEG method," *JHEP* **11** (2007) 070, arXiv:0709.2092 [hep-ph].

[55] F. Maltoni and T. Stelzer, "MadEvent: automatic event generation with MadGraph," *JHEP* **02** (2003) 027, arXiv:hep-ph/0208156 [hep-ph].

[56] J. Alwall, R. Frederix, S. Frixione, V. Hirschi, F. Maltoni, O. Mattelaer, H.-S. Shao, T. Stelzer, P. Torielli, and M. Zaro, "The automated computation of tree-level and next-to-leading order differential cross sections, and their matching to parton shower simulations," *JHEP* **07** (2014) 079, arXiv:1405.0301 [hep-ph].

[57] **CompHEP** Collaboration, E. Boos *et al.*, "CompHEP 4.4 – automatic computations from Lagrangians to events," *Nucl. Instrum. Meth. A* **534** (2004) 250, arXiv:hep-ph/0403113 [hep-ph].

[58] R. Frederix, E. Re, and P. Torrielli, "Single-top t-channel hadroproduction in the four-flavour scheme with POWHEG and aMC@NLO," *JHEP* **09** (2012) 130, arXiv:1207.5391 [hep-ex].

[59] M. A. Dobbs *et al.*, "Les Houches guidebook to Monte Carlo generators for hadron collider physics," in *Physics at TeV colliders. Proceedings, Workshop, Les Houches, France, May 26-June 3, 2003*, pp. 411–459. 2004. arXiv:hep-ph/0403045 [hep-ph].

[60] H.-L. Lai, M. Guzzi, J. Huston, Z. Li, P. M. Nadolsky, J. Pumplin, and C. P. Yuan, "New parton distributions for collider physics," *Phys. Rev.* **D82** (2010) 074024, arXiv:1007.2241 [hep-ph].

[61] A. D. Martin, W. J. Stirling, R. S. Thorne, and G. Watt, "Parton distributions for the LHC," *Eur. Phys. J.* **C63** (2009) 189–285, arXiv:0901.0002 [hep-ph].

[62] R. D. Ball *et al.*, "Parton distributions with LHC data," *Nucl. Phys.* **B867** (2013) 244–289, arXiv:1207.1303 [hep-ph].

[63] M. Botje *et al.*, "The PDF4LHC Working Group Interim Recommendations," arXiv:1101.0538 [hep-ph].

[64] **GEANT4** Collaboration, S. Agostinelli *et al.*, "GEANT4 – a simulation toolkit," *Nucl. Instrum. Meth. A* **506** (2003) 250.

[65] **CMS** Collaboration, S. Abdullin, P. Azzi, F. Beaudette, P. Janot, and A. Perrotta, "The fast simulation of the CMS detector at LHC," *J. Phys. Conf. Ser.* **331** (2011) 032049.

[66] **CMS** Collaboration, "Pileup removal algorithms," CMS-PAS-JME-14-001, CERN, Geneva, 2014. https://cds.cern.ch/record/1751454.

[67] A. Rizzi, F. Palla, and G. Segneri, "Track impact parameter based b-tagging with CMS," CMS-NOTE-2006-019, CERN, Geneva, Jan, 2006. https://cds.cern.ch/record/927385.

[68] C. Weiser, "A combined secondary vertex based b-tagging algorithm in CMS," CERN-CMS-NOTE-2006-014, 2006.

[69] **CMS** Collaboration, "b-jet identification in the CMS experiment," CMS-PAS-BTV-11-004, CERN, Geneva, 2012. https://cds.cern.ch/record/1427247.

[70] **CMS** Collaboration, "Performance of b tagging at $\sqrt{s} = 8$ TeV in multijet, ttbar and boosted topology events," CMS-PAS-BTV-13-001, CERN, Geneva, 2013. https://cds.cern.ch/record/1581306.

[71] M. L. Mangano, M. Moretti, F. Piccinini, and M. Treccani, "Matching matrix elements and shower evolution for top-quark production in hadronic collisions," *JHEP* **01** (2007) 013, arXiv:hep-ph/0611129 [hep-ph].

[72] J. Alwall, S. Höche, F. Krauss, N. Lavesson, L. Lönnblad, F. Maltoni, M. L. Mangano, M. Moretti, C. G. Papadopoulos, F. Piccinini, S. Schumann, M. Treccani, J. Winter, and M. Worek, "Comparative study of various algorithms for the merging of parton showers and matrix elements in hadronic collisions," *Eur. Phys. J. C* **53** (2008) 473, arXiv:0706.2569 [hep-ph].

[73] J. Pumplin, D. Stump, J. Huston, H. Lai, P. M. Nadolsky, *et al.*, "New generation of parton distributions with uncertainties from global QCD analysis," *JHEP* **07** (2002) 012, arXiv:hep-ph/0201195 [hep-ph].

[74] N. Kidonakis, "Differential and total cross sections for top pair and single top production," in *Proceedings of the XX International Workshop on Deep-Inelastic Scattering and Related Subjects*. Bonn, Germany, 2012. arXiv:1205.3453 [hep-ph]. An update can be found in arXiv:1311.0283.

[75] M. Czakon and A. Mitov, "Top++: A program for the calculation of the top-pair cross-section at hadron colliders," *Comput. Phys. Commun.* **185** (2014) 2930, arXiv:1112.5675 [hep-ph].

[76] M. Czakon, P. Fiedler, and A. Mitov, "Total top-quark pair-production cross section at hadron colliders through $\mathcal{O}(\alpha_S^4)$," *Phys. Rev. Lett.* **110** (Jun, 2013) 252004, arXiv:1303.6254 [hep-ph].

[77] R. Gavin, Y. Li, F. Petriello, and S. Quackenbush, "FEWZ 2.0: a code for hadronic Z production at next-to-next-to-leading order," *Comput. Phys. Commun.* **182** (2011) 2388, arXiv:1011.3540 [hep-ph].

[78] J. M. Campbell and R. K. Ellis, "MCFM for the Tevatron and the LHC," *Nucl. Phys. Proc. Suppl.* **205-206** (2010) 10, arXiv:1007.3492 [hep-ph].

[79] T. Müller, J. Ott, and J. Wagner-Kuhr, "theta – a framework for template-based modeling and inference." http://www-ekp.physik.uni-karlsruhe.de/~ott/theta/theta.pdf, 2010.

[80] T. Hastie, R. Tibshirani, and J. Friedman, *The Elements of Statistical Learning: Data Mining, Inference, and Prediction, Second Edition*. Springer Series in Statistics. Springer, 2009. http://statweb.stanford.edu/~tibs/ElemStatLearn/.

[81] V. Blobel, "An unfolding method for high-energy physics experiments," in *Advanced statistical techniques in particle physics. Proceedings, Conference, Durham, UK, March 18-22, 2002*, p. 258. 2002. arXiv:hep-ex/0208022 [hep-ex].

[82] **CMS** Collaboration, S. Chatrchyan *et al.*, "Measurement of the charge asymmetry in top-quark pair production in proton-proton collisions at $\sqrt{s} = 7$ TeV," *Phys. Lett. B* **709** (2012) 28, arXiv:1112.5100 [hep-ex].

[83] **CMS** Collaboration, S. Chatrchyan *et al.*, "Inclusive and differential measurements of the $t\bar{t}$ charge asymmetry in proton-proton collisions at 7 TeV," *Phys. Lett.* **B717** (2012) 129, arXiv:1207.0065 [hep-ex].

[84] A. Tikhonov, "Solution of incorrectly formulated problems and the regularization method," *Soviet Mathematics* **4** (1963) 1035–1038.

[85] S. Schmitt, "TUnfold, an algorithm for correcting migration effects in high energy physics," *Journal of Instrumentation* **7** no. 10, (2012) T10003.

[86] **CMS** Collaboration, "Determination of the jet energy scale in CMS with pp collisions at $\sqrt{s} = 7$ TeV," CMS Physics Analysis Summary CMS-PAS-JME-10-010, 2010. http://cdsweb.cern.ch/record/1308178.

[87] **CMS** Collaboration, "Jet energy resolution in CMS at $\sqrt{s} = 7$ TeV," CMS Physics Analysis Summary CMS-PAS-JME-10-014, 2010. http://cdsweb.cern.ch/record/1339945.

[88] **CMS** Collaboration, V. Khachatryan *et al.*, "Measurements of inclusive W and Z cross sections in pp collisions at $\sqrt{s} = 7$ TeV," *JHEP* **01** (2011) 080, arXiv:1012.2466 [hep-ex].

[89] **CMS** Collaboration, S. Chatrchyan *et al.*, "Measurement of the lepton charge asymmetry in inclusive W production in pp collisions at $\sqrt{s} = 7$ TeV," *JHEP* **04** (2011) 050.

[90] R. J. Barlow and C. Beeston, "Fitting using finite Monte Carlo samples," *Comput. Phys. Commun.* **77** (1993) 219.

[91] J. S. Conway, "Nuisance parameters in likelihoods for multisource spectra," in *Proceedings of PHYSTAT 2011 Workshop on Statistical Issues Related to Discovery Claims in Search Experiments and Unfolding*, H. B. Prosper and L. Lyons, eds., p. 115. CERN, 2011. arXiv:1103.0354 [physics.data-an]. http://cdsweb.cern.ch/record/1306523.

[92] **CMS** Collaboration, "Absolute calibration of the luminosity measurement at CMS: Winter 2012 update," CMS Physics Analysis Summary CMS-PAS-SMP-12-008, 2012. http://cdsweb.cern.ch/record/1434360.

[93] **CMS** Collaboration, "CMS luminosity based on pixel cluster counting - summer 2013 update," CMS Physics Analysis Summary CMS-PAS-LUM-13-001, CERN, 2013. https://cdsweb.cern.ch/record/1598864.

[94] **CMS** Collaboration, S. Chatrchyan *et al.*, "Measurement of the $\mathrm{t\bar{t}}$ production cross section in pp collisions at 7 TeV in lepton + jets events using b-quark jet identification," *Phys. Rev. D* **84** (2011) 092004, arXiv:1108.3773 [hep-ex].

[95] M. Cacciari, M. Czakon, M. Mangano, A. Mitov, and P. Nason, "Top-pair production at hadron colliders with next-to-next-to-leading logarithmic

soft-gluon resummation," *Phys. Lett. B* **710** (2012) 612, arXiv:1111.5869 [hep-ph].

[96] J. M. Campbell, R. Frederix, F. Maltoni, and F. Tramontano, "Next-to-Leading-Order predictions for t-channel single-top production at hadron colliders," *Phys.Rev.Lett.* **102** (2009) 182003, arXiv:0903.0005 [hep-ph].

[97] M. Whalley, D. Bourilkov, and R. Group, "The Les Houches accord PDFs (LHAPDF) and LHAGLUE," (2005) , arXiv:hep-ph/0508110 [hep-ph].

[98] A. D. Martin, A. J. T. M. Mathijssen, W. J. Stirling, R. S. Thorne, B. J. A. Watt, and G. Watt, "Extended parameterisations for MSTW PDFs and their effect on lepton charge asymmetry from W decays," *Eur. Phys. J. C* **73** (2013) 2318, arXiv:1211.1215 [hep-ph].

[99] **CMS** Collaboration, S. Chatrchyan *et al.*, "Measurement of the t-channel single top quark production cross section in pp collisions at $\sqrt{s} = 7$ TeV," *Phys. Rev. Lett.* **107** (2011) 091802, arXiv:1106.3052 [hep-ex].

[100] **ATLAS** Collaboration, G. Aad *et al.*, "Measurement of the t-channel single top-quark production cross section in pp collisions at $\sqrt{s} = 7$ TeV with the ATLAS detector," *Phys. Lett. B* **717** (2012) 330, arXiv:1205.3130 [hep-ex].

[101] N. Kidonakis, "Next-to-next-to-leading-order collinear and soft gluon corrections for t-channel single top quark production," *Phys. Rev. D* **83** (2011) 091503, arXiv:1103.2792 [hep-ph].

[102] **ATLAS** Collaboration, G. Aad *et al.*, "Measurement of the cross section for the production of a W boson in association with b-jets in pp collisions at $\sqrt{s} = 7$ TeV with the ATLAS detector," *Phys. Lett. B* **707** (2012) 418, arXiv:1109.1470 [hep-ex].

[103] L. Lyons, D. Gibaut, and P. Clifford, "How to combine correlated estimates of a single physical quantity," *Nucl. Instr. and Meth. A* **270** (1988) 110.

[104] G. J. Feldman and R. D. Cousins, "A unified approach to the classical statistical analysis of small signals," *Phys. Rev. D* **57** (1998) 3873, arXiv:physics/9711021 [physics.data-an].

[105] **H1** and **ZEUS** collaborations, "Combined measurement and QCD analysis of the inclusive $e^{\pm}p$ scattering cross sections at *HERA* ," *JHEP* **01** (2010) 109, arXiv:0911.0884 [hep-ph].

[106] S. Alekhin, J. Blümlein, and S. Moch, "Parton distribution functions and benchmark cross sections at NNLO," *Phys. Rev. D* **86** (2012) 0054009, arXiv:1202.2281 [hep-ph].

[107] A. Hocker *et al.*, "TMVA - Toolkit for Multivariate Data Analysis," in *Proceedings, 11th International Workshop on Advanced computing and analysis techniques in physics research (ACAT 2007)*, vol. ACAT, p. 040. 2007. arXiv:physics/0703039 [physics.data-an].

[108] **CMS** Collaboration, S. Chatrchyan *et al.*, "Measurement of differential top-quark pair production cross sections in pp collisions at $\sqrt{s} = 7$ TeV," *Eur. Phys. J. C* **73** (2013) 2339, arXiv:1211.2220 [hep-ex].

[109] **CMS** Collaboration, V. Khachatryan *et al.*, "Measurement of the differential cross section for top quark pair production in pp collisions at $\sqrt{s} = 8$ TeV," *Eur. Phys. J. C* **75** (2015) 542, arXiv:1505.04480 [hep-ex].

[110] J. M. Campbell, R. Frederix, F. Maltoni, and F. Tramontano, "NLO predictions for *t*-channel production of single top and fourth generation quarks at hadron colliders," *JHEP* **10** (2009) 042, arXiv:0907.3933 [hep-ph].

[111] **D0** Collaboration, V. Abazov *et al.*, "Model-independent measurement of t-channel single top quark production in $p\bar{p}$ collisions at $\sqrt{(s)} = 1.96 TeV$," *Physics Letters B* **705** no. 4, (2011) 313 – 319.

[112] **CDF** and **D0** Collaborations, "Combination of the top-quark mass measurements from the Tevatron collider," *Phys. Rev. D* **86** (2012) 092003, arXiv:1207.1069. An update can be found in arXiv:1305.3929.

[113] J. M. Campbell, J. W. Huston, and W. J. Stirling, "Hard interactions of quarks and gluons: A primer for LHC physics," *Rept. Prog. Phys.* **70** (2007) 89, arXiv:hep-ph/0611148.

Curriculum Vitae

Andres Tiko ✉ *andres.tiko@cern.ch*

Haridus

2010–2016 **Füüsika doktoriõpe**, *Tartu Ülikool.*

lõputöö *Measuring single top quark properties with the CMS detector*

juhendajad Andrea Giammanco, Mario Kadastik ja Martti Raidal

2007–2009 **Informaatika magister**, *Tartu Ülikool.*

lõputöö *Ripple-down rule sets and MDL learning*

juhendajad Jaak Vilo ja Meelis Kull

2003–2007 **Füüsika bakalaureus**, *Tartu Ülikool.*

lõputöö *Ülijuhtivusomadused kahetsoonilises pilustatud mudelis*

juhendaja N. Kristoffel

2003 **Keskharidus**, *Tallinna Reaalkool.*

Publikatsioonid

2016 CMS collaboration. "**Measurement of top quark polarisation in t-channel single top quark production**". *JHEP*, 2016.4, pp. 1–42.

2015 A. Tiko on behalf of the CMS collaboration. "**Measurement of top quark properties in single top production**". *Proceedings, 2015 European Physical Society Conference on High Energy Physics (EPS-HEP 2015)*, EPS-HEP2015.

2014 CMS collaboration. "**Measurement of the t-channel single-top-quark production cross section and of the $|V_{tb}|$ CKM matrix element in pp collisions at $\sqrt{s} = 8$ TeV**". *Journal of High Energy Physics*, 2014.6, 90.

2012 CMS collaboration. "**Measurement of the single-top-quark t-channel cross section in pp collisions at $\sqrt{s} = 7$ TeV.**" *Journal of High Energy Physics*, 12, p. 035.

Ettekanded ja postrid

2016 "Poster **Measurement of top quark polarisation in t-channel single top quark production**". *TOP2016: 9th International Workshop on Top Quark Physics.*

2015 "**Measurement of top quark properties in single top production**". *EPS-HEP 2015: European Physical Society Conference on High Energy Physics.*

2014 "**Higgsi bosoni avastamine**". *Eesti füüsikapäevad.*

2014 "Poster **Measurement of top quark polarization in t-channel single-top production**". *FMTDK doktorikooli konverents.*

2014 "Poster **Measurement of top quark polarization in t-channel single-top production**". *LHC students poster session.* CERN.

2013 "**Measurement of top polarization in t-channel single-top roduction in pp collisions at $\sqrt{s} = 8$ TeV**". *Tartu-Tuorla kosmoloogiakonverents.*

2012 "**Measuring top properties with the CMS detector**". *Tippkeskuse "Dark Matter in (Astro)particle Physics and Cosmology" seminar "From Cosmology to HEP and vice versa".*

Täielik publikatsioonide nimekiri: `https://inspirehep.net/author/profile/A.Tiko.2`

Täiendõpe

2012 **European School of High Energy Physics**.

2012 **CMS Data Analysis School**.

2011 **50. Internationale Universitätswochen für Theoretische Physik - Prospects of Particle Physics**.

2011 **Mass 2011 LHC Training School**.

2011 **CERNi suveüliõpilane**.

Õpetamine ja juhendamine

2013 **Õppejõud**, *Experimentaalne osakestefüüsika*, Tartu ülikool, lisaks kursuse materjalide väljatöötamine.

2012 **Õppejõud**, *Elektriahelad*, Tartu ülikool.

2012 **Kaasjuhendaja**, *Joosep Pata bakalaureusetöö "Supersümmeetriline tumeaine"*, University of Tartu.

Auhinnad

2012 **Juhendaja preemia Eesti Teadusagentuuri teadustööde võistlusel**, *esimese preemia saanud Joosep Pata bakalaureusetöö "Supersümmeetriline tumeaine" eest.*

2008 **Playtechi stipendium**.

2002–2003 **Auhinnalised kohad Eesti füüsika- ja matemaatikaolümpiaadidel**, *rahvusvahelise füüsikaolümpiaadi Eesti koondise kandidaat.*

Töökogemus

2009–2010 **Tarkvaraarendaja**, *Tata Consultancy Services*, Mumbai.

2006–2007 **Tarkvara- ja teenuste arendaja**, *Mobi Solutions*, Tartu.

Muu kogemus

2003–2006 **Füüsika lahtiste võistluste läbiviija Tallinnas**.

2003 **Eesti Füüsika Seltsi liige**.

Curriculum Vitae

Andres Tiko ✉ *andres.tiko@cern.ch*

Education

2010–2016 **PhD programme in Physics**, *University of Tartu*.

thesis *Measuring single top quark properties with the CMS detector*

supervisors Andrea Giammanco, Mario Kadastik and Martti Raidal

2007–2009 **MS in Computer Science**, *University of Tartu*.

thesis *Ripple-down rule sets and MDL learning*

supervisors Jaak Vilo and Meelis Kull

2003–2007 **BSc in Physics**, *University of Tartu*.

thesis *Superconducting properties of a gapped metallic two-band model*

supervisor N. Kristoffel

Publications

2016 CMS collaboration. "**Measurement of top quark polarisation in t-channel single top quark production**". *JHEP*, 2016.4, pp. 1–42.

2015 A. Tiko on behalf of the CMS collaboration. "**Measurement of top quark properties in single top production**". *Proceedings, 2015 European Physical Society Conference on High Energy Physics (EPS-HEP 2015)*, EPS-HEP2015.

2014 CMS collaboration. "**Measurement of the t-channel single-top-quark production cross section and of the $|V_{tb}|$ CKM matrix element in pp collisions at $\sqrt{s} = 8$ TeV**". *Journal of High Energy Physics*, 2014.6, 90.

2012 CMS collaboration. "**Measurement of the single-top-quark t-channel cross section in pp collisions at $\sqrt{s} = 7$ TeV**". *Journal of High Energy Physics*, 12, p. 035.

Talks and posters

2016 "Poster **Measurement of top quark polarisation in t-channel single top quark production**". *TOP2016: 9th International Workshop on Top Quark Physics*.

2015 "**Measurement of top quark properties in single top production**". *EPS-HEP 2015: European Physical Society Conference on High Energy Physics*.

2014 "**Discovery of the Higgs boson**". *Estonian Physics Days*.

2014 "Poster **Measurement of top quark polarization in t-channel single-top production**". *FMTDK doctoral school conference*.

2014 "Poster **Measurement of top quark polarization in t-channel single-top production**". *LHC students poster session*. CERN.

2013 "**Measurement of top polarization in t-channel single-top roduction in pp collisions at $\sqrt{s} = 8$ TeV**". *Tartu-Tuorla cosmology conference*.

2012 "**Measuring top properties with the CMS detector**". *Seminar "From Cosmology to HEP and vice versa" of the "Dark Matter in (Astro)particle Physics and Cosmology" Centre of Excellence*.

Full list of publications `http://inspirehep.net/author/A.Tiko.2/`

Other training

2012 **European School of High Energy Physics**.

2012 **CMS Data Analysis School**.

2011 **50. Internationale Universitätswochen für Theoretische Physik - Prospects of Particle Physics**.

2011 **Mass 2011 LHC Training School**.

2011 **CERN Summer Student**.

DISSERTATIONES PHYSICAE UNIVERSITATIS TARTUENSIS

1. **Andrus Ausmees.** XUV-induced electron emission and electron-phonon interaction in alkali halides. Tartu, 1991.
2. **Heiki Sõnajalg.** Shaping and recalling of light pulses by optical elements based on spectral hole burning. Tartu, 1991.
3. **Sergei Savihhin.** Ultrafast dynamics of F-centers and bound excitons from picosecond spectroscopy data. Tartu, 1991.
4. **Ergo Nõmmiste.** Leelishalogeniidide röntgenelektronemissioon kiiritamisel footonitega energiaga 70–140 eV. Tartu, 1991.
5. **Margus Rätsep.** Spectral gratings and their relaxation in some low-temperature impurity-doped glasses and crystals. Tartu, 1991.
6. **Tõnu Pullerits.** Primary energy transfer in photosynthesis. Model calculations. Tartu, 1991.
7. **Olev Saks.** Attoampri diapasoonis voolude mõõtmise füüsikalised alused. Tartu, 1991.
8. **Andres Virro.** AlGaAsSb/GaSb heterostructure injection lasers. Tartu, 1991.
9. **Hans Korge.** Investigation of negative point discharge in pure nitrogen at atmospheric pressure. Tartu, 1992.
10. **Jüri Maksimov.** Nonlinear generation of laser VUV radiation for high-resolution spectroscopy. Tartu, 1992.
11. **Mark Aizengendler.** Photostimulated transformation of aggregate defects and spectral hole burning in a neutron-irradiated sapphire. Tartu, 1992.
12. **Hele Siimon.** Atomic layer molecular beam epitaxy of A^2B^6 compounds described on the basis of kinetic equations model. Tartu, 1992.
13. **Tõnu Reinot.** The kinetics of polariton luminescence, energy transfer and relaxation in anthracene. Tartu, 1992.
14. **Toomas Rõõm.** Paramagnetic H^{2-} and F^+ centers in CaO crystals: spectra, relaxation and recombination luminescence. Tallinn, 1993.
15. **Erko Jalviste.** Laser spectroscopy of some jet-cooled organic molecules. Tartu, 1993.
16. **Alvo Aabloo.** Studies of crystalline celluloses using potential energy calculations. Tartu, 1994.
17. **Peeter Paris.** Initiation of corona pulses. Tartu, 1994.
18. **Павел Рубин.** Локальные дефектные состояния в CuO_2 плоскостях высокотемпературных сверхпроводников. Тарту, 1994.
19. **Olavi Ollikainen.** Applications of persistent spectral hole burning in ultrafast optical neural networks, time-resolved spectroscopy and holographic interferometry. Tartu, 1996.
20. **Ülo Mets.** Methodological aspects of fluorescence correlation spectroscopy. Tartu, 1996.
21. **Mikhail Danilkin.** Interaction of intrinsic and impurity defects in CaS:Eu luminophors. Tartu, 1997.

22. **Ирина Кудрявцева.** Создание и стабилизация дефектов в кристаллах KBr, KCl, RbCl при облучении ВУФ-радиацией. Тарту, 1997.
23. **Andres Osvet.** Photochromic properties of radiation-induced defects in diamond. Tartu, 1998.
24. **Jüri Örd.** Classical and quantum aspects of geodesic multiplication. Tartu, 1998.
25. **Priit Sarv.** High resolution solid-state NMR studies of zeolites. Tartu, 1998.
26. **Сергей Долгов.** Электронные возбуждения и дефектообразование в некоторых оксидах металлов. Тарту, 1998.
27. **Kaupo Kukli.** Atomic layer deposition of artificially structured dielectric materials. Tartu, 1999.
28. **Ivo Heinmaa.** Nuclear resonance studies of local structure in $RBa_2Cu_3O_{6+x}$ compounds. Tartu, 1999.
29. **Aleksander Shelkan.** Hole states in CuO_2 planes of high temperature superconducting materials. Tartu, 1999.
30. **Dmitri Nevedrov.** Nonlinear effects in quantum lattices. Tartu, 1999.
31. **Rein Ruus.** Collapse of 3d (4f) orbitals in 2p (3d) excited configurations and its effect on the x-ray and electron spectra. Tartu, 1999.
32. **Valter Zazubovich.** Local relaxation in incommensurate and glassy solids studied by Spectral Hole Burning. Tartu, 1999.
33. **Indrek Reimand.** Picosecond dynamics of optical excitations in GaAs and other excitonic systems. Tartu, 2000.
34. **Vladimir Babin.** Spectroscopy of exciton states in some halide macro- and nanocrystals. Tartu, 2001.
35. **Toomas Plank.** Positive corona at combined DC and AC voltage. Tartu, 2001.
36. **Kristjan Leiger.** Pressure-induced effects in inhomogeneous spectra of doped solids. Tartu, 2002.
37. **Helle Kaasik.** Nonperturbative theory of multiphonon vibrational relaxation and nonradiative transitions. Tartu, 2002.
38. **Tõnu Laas.** Propagation of waves in curved spacetimes. Tartu, 2002.
39. **Rünno Lõhmus.** Application of novel hybrid methods in SPM studies of nanostructural materials. Tartu, 2002.
40. **Kaido Reivelt.** Optical implementation of propagation-invariant pulsed free-space wave fields. Tartu, 2003.
41. **Heiki Kasemägi.** The effect of nanoparticle additives on lithium-ion mobility in a polymer electrolyte. Tartu, 2003.
42. **Villu Repän.** Low current mode of negative corona. Tartu, 2004.
43. **Алексей Котлов.** Оксианионные диэлектрические кристаллы: зонная структура и электронные возбуждения. Tartu, 2004.
44. **Jaak Talts.** Continuous non-invasive blood pressure measurement: comparative and methodological studies of the differential servo-oscillometric method. Tartu, 2004.
45. **Margus Saal.** Studies of pre-big bang and braneworld cosmology. Tartu, 2004.

46. **Eduard Gerškevitš.** Dose to bone marrow and leukaemia risk in external beam radiotherapy of prostate cancer. Tartu, 2005.
47. **Sergey Shchemelyov.** Sum-frequency generation and multiphoton ionization in xenon under excitation by conical laser beams. Tartu, 2006.
48. **Valter Kiisk.** Optical investigation of metal-oxide thin films. Tartu, 2006.
49. **Jaan Aarik.** Atomic layer deposition of titanium, zirconium and hafnium dioxides: growth mechanisms and properties of thin films. Tartu, 2007.
50. **Astrid Rekker.** Colored-noise-controlled anomalous transport and phase transitions in complex systems. Tartu, 2007.
51. **Andres Punning.** Electromechanical characterization of ionic polymer-metal composite sensing actuators. Tartu, 2007.
52. **Indrek Jõgi.** Conduction mechanisms in thin atomic layer deposited films containing TiO_2. Tartu, 2007.
53. **Aleksei Krasnikov.** Luminescence and defects creation processes in lead tungstate crystals. Tartu, 2007.
54. **Küllike Rägo.** Superconducting properties of MgB_2 in a scenario with intra- and interband pairing channels. Tartu, 2008.
55. **Els Heinsalu.** Normal and anomalously slow diffusion under external fields. Tartu, 2008.
56. **Kuno Kooser.** Soft x-ray induced radiative and nonradiative core-hole decay processes in thin films and solids. Tartu, 2008.
57. **Vadim Boltrushko.** Theory of vibronic transitions with strong nonlinear vibronic interaction in solids. Tartu, 2008.
58. **Andi Hektor.** Neutrino Physics beyond the Standard Model. Tartu, 2008.
59. **Raavo Josepson.** Photoinduced field-assisted electron emission into gases. Tartu, 2008.
60. **Martti Pärs.** Study of spontaneous and photoinduced processes in molecular solids using high-resolution optical spectroscopy. Tartu, 2008.
61. **Kristjan Kannike.** Implications of neutrino masses. Tartu, 2008.
62. **Vigen Issahhanjan.** Hole and interstitial centres in radiation-resistant MgO single crystals. Tartu, 2008.
63. **Veera Krasnenko.** Computational modeling of fluorescent proteins. Tartu, 2008.
64. **Mait Müntel.** Detection of doubly charged higgs boson in the CMS detector. Tartu, 2008.
65. **Kalle Kepler.** Optimisation of patient doses and image quality in diagnostic radiology. Tartu, 2009.
66. **Jüri Raud.** Study of negative glow and positive column regions of capillary HF discharge. Tartu, 2009.
67. **Sven Lange.** Spectroscopic and phase-stabilisation properties of pure and rare-earth ions activated ZrO_2 and HfO_2. Tartu, 2010.
68. **Aarne Kasikov.** Optical characterization of inhomogeneous thin films. Tartu, 2010.
69. **Heli Valtna-Lukner.** Superluminally propagating localized optical pulses. Tartu, 2010.

70. **Artjom Vargunin.** Stochastic and deterministic features of ordering in the systems with a phase transition. Tartu, 2010.
71. **Hannes Liivat.** Probing new physics in e+e− annihilations into heavy particles via spin orientation effects. Tartu, 2010.
72. **Tanel Mullari.** On the second order relativistic deviation equation and its applications. Tartu, 2010.
73. **Aleksandr Lissovski.** Pulsed high-pressure discharge in argon: spectroscopic diagnostics, modeling and development. Tartu, 2010.
74. **Aile Tamm.** Atomic layer deposition of high-permittivity insulators from cyclopentadienyl-based precursors. Tartu, 2010.
75. **Janek Uin.** Electrical separation for generating standard aerosols in a wide particle size range. Tartu, 2011.
76. **Svetlana Ganina.** Hajusandmetega ülesanded kui üks võimalus füüsikaõppe efektiivsuse tõstmiseks. Tartu, 2011
77. **Joel Kuusk.** Measurement of top-of-canopy spectral reflectance of forests for developing vegetation radiative transfer models. Tartu, 2011.
78. **Raul Rammula**. Atomic layer deposition of HfO_2 – nucleation, growth and structure development of thin films. Tartu, 2011.
79. **Сергей Наконечный.** Исследование электронно-дырочных и интерстициал-вакансионных процессов в монокристаллах MgO и LiF методами термоактивационной спектроскопии. Тарту, 2011.
80. **Niina Voropajeva.** Elementary excitations near the boundary of a strongly correlated crystal. Tartu, 2011.
81. **Martin Timusk.** Development and characterization of hybrid electro-optical materials. Tartu, 2012, 106 p.
82. **Merle Lust.** Assessment of dose components to Estonian population. Tartu, 2012, 84 p.
83. **Karl Kruusamäe.** Deformation-dependent electrode impedance of ionic electromechanically active polymers. Tartu, 2012, 128 p.
84. **Liis Rebane.** Measurement of the $W \to \tau\nu$ cross section and a search for a doubly charged Higgs boson decaying to τ-leptons with the CMS detector. Tartu, 2012, 156 p.
85. **Jevgeni Šablonin.** Processes of structural defect creation in pure and doped MgO and NaCl single crystals under condition of low or super high density of electronic excitations. Tartu, 2013, 145 p.
86. **Riho Vendt**. Combined method for establishment and dissemination of the international temperature scale. Tartu, 2013, 108 p.
87. **Peeter Piksarv.** Spatiotemporal characterization of diffractive and non-diffractive light pulses. Tartu, 2013, 156 p.
88. **Anna Šugai.** Creation of structural defects under superhigh-dense irradiation of wide-gap metal oxides. Tartu, 2013, 108 p.
89. **Ivar Kuusik.** Soft X-ray spectroscopy of insulators. Tartu, 2013, 113 p.
90. **Viktor Vabson**. Measurement uncertainty in Estonian Standard Laboratory for Mass. Tartu, 2013, 134 p.

91. **Kaupo Voormansik.** X-band synthetic aperture radar applications for environmental monitoring. Tartu, 2014, 117 p.
92. **Deivid Pugal.** hp-FEM model of IPMC deformation. Tartu, 2014, 143 p.
93. **Siim Pikker.** Modification in the emission and spectral shape of photostable fluorophores by nanometallic structures. Tartu, 2014, 98 p.
94. **Mihkel Pajusalu**. Localized Photosynthetic Excitons. Tartu, 2014, 183 p.
95. **Taavi Vaikjärv.** Consideration of non-adiabaticity of the Pseudo-Jahn-Teller effect: contribution of phonons. Tartu, 2014, 129 p.
96. **Martin Vilbaste.** Uncertainty sources and analysis methods in realizing SI units of air humidity in Estonia. Tartu, 2014, 111 p.
97. **Mihkel Rähn.** Experimental nanophotonics: single-photon sources- and nanofiber-related studies. Tartu, 2015, 107 p.
98. **Raul Laasner.** Excited state dynamics under high excitation densities in tungstates. Tartu, 2015, 125 p.
99. **Andris Slavinskis.** EST Cube-1 attitude determination. Tartu, 2015, 104 p.
100. **Karlis Zalite**. Radar Remote Sensing for Monitoring Forest Floods and Agricultural Grasslands. Tartu, 2016, 124 p.
101. **Kaarel Piip.** Development of LIBS for *in-situ* study of ITER relevant materials. Tartu, 2016, 93 p.
102. **Kadri Isakar.** ^{210}Pb in Estonian air: long term study of activity concentrations and origin of radioactive lead. Tartu, 2016, 107 p.
103. **Artur Tamm.** High entropy alloys: study of structural properties and irradiation response. Tartu, 2016, 115 p.
104. **Rasmus Talviste.** Atmospheric-pressure He plasma jet: effect of dielectric tube diameter. Tartu, 2016, 107 p.